University of Alberta
Department of Civil Engineering

Structural Engineering Report No. 147

INCIPIENT FLOW IN SILOS

A Numerical Approach

By

R. A. LINK
and
A. E. ELWI

May 1987

RECENT STRUCTURAL ENGINEERING REPORTS

Department of Civil Engineering

University of Alberta

116. *Reinforced Concrete Column Design Program* by C-K. Leung and S.H. Simmonds, April 1984.

117. *Deflections of Two-way Slabs under Construction Loading* by C. Graham and A. Scanlon, August 1984.

118. *Effective Lengths of Laterally Unsupported Steel Beams* by C.D. Schmitke and D.J.L. Kennedy, October 1984.

119. *Flexural and Shear Behaviour of Large Diameter Steel Tubes* by R.W. Bailey and G.L. Kulak, November 1984.

120. *Concrete Masonry Prism Response due to Loads Parallel and Perpendicular to Bed Joints* by R. Lee, J. Longworth and J. Warwaruk.

121. *Standardized Flexible End Plate Connections for Steel Beams* by G.J. Kriviak and D.J.L. Kennedy, December 1984.

122. *The Effects of Restrained Shrinkage on Concrete Slabs* by K.S.S. Tam and A. Scanlon, December 1984.

123. *Prestressed Concrete Beams with Large Rectangular Web Openings* by T. do M.J. Alves and A. Scanlon, December 1984.

124. *Tests on Eccentrically Loaded Fillet Welds* by G.L. Kulak and P.A. Timler, December 1984.

125. *Analysis of Field Measured Deflections Scotia Place Office Tower* by A. Scanlon and E. Ho, December 1984.

126. *Ultimate Behaviour of Continuous Deep Reinforced Concrete Beams* by D.R. Ricketts and J.G. MacGregor, January 1985.

127. *The Interaction of Masonry Veneer and Steel Studs in Curtain Wall Construction* by W.M. McGinley, J. Warwaruk, J. Longworth and M. Hatzinikolas, May 1985.

128. *Evaluation of Existing Bridge Structure by Nondestructive Test Methods* by L. Mikhailovsky and A. Scanlon, May 1985.

129. *Finite Element Modelling of Buried Structures* by D.K. Playdon and S.H. Simmonds, October 1985.

130. *Behaviour and Ultimate Strength of Transversely Loaded Continuous Steel Plates* by K.P. Ratzlaff and D.J.L. Kennedy, November 1985.

131. *Inelastic Lateral Buckling of Steel Beam-Columns* by P.E. Cuk, M.A. Bradford and N.S. Trahair, December 1985.

132. *Design Strengths of Steel Beam-Columns* by N.S. Trahair, December 1985.

133. *Behaviour of Fillet Welds as a Function of the Angle of Loading* by G.S. Miazga and D.J.L. Kennedy, March 1986.

134. *Inelastic Seismic Response of Precast Concrete Large Panel Coupled Shear Wall Systems* by M.R. Kianoush and A. Scanlon, March 1986.

135. *Finite Element Prediction of Bin Loads* by A.H. Askari and A.E. Elwi, June 1986.

136. *Shear Behavior of Large Diameter Fabricated Steel Cylinders* by J. Mok and A.E. Elwi, June 1986.

137. *Local Buckling Rules for Structural Steel Members* by S. Bild and G.L. Kulak, May 1986.

138. *Finite Element Prediction of Reinforced Concrete Behavior* by S. Balakrishnan and D.W. Murray, July 1986.

139. *Behavior and Strength of Masonry Wall/Slab Joints* by T.M. Olatunji and J. Warwaruk, July 1986.

140. *Bayesian Analysis of In-Situ Test Data for Estimating the Compressive Strength of Concrete in Existing Structures* by G.J. Kriviak and A. Scanlon, July 1986.

141. *Shear-Moment Transfer in Slab-Column Connections* by S.D.B. Alexander and S.H. Simmonds, July 1986.

142. *Minimum Thickness Requirements for Deflection Control of Two-Way Slab Systems* by D.P. Thompson and A. Scanlon, November 1986.

143. *Shrinkage and Flexural Tests of Two Full-Scale Composite Trusses* by A. Brattland and D.J.L. Kennedy, December 1986.

144. *Combined Flexure and Torsion of I-Shaped Steel Beams* by R.G. Driver and D.J.L. Kennedy, March 1987.

145. *Cyclic and Static Behaviour of Thin Panel Steel Plate Shear Walls* by E.W. Tromposch and G.L. Kulak, April 1987.

146. *Postbuckling Behavior of Thin Steel Cylinders Under Transverse Shear* by V.G. Roman and A.E. Elwi, May 1987.

147. *Incipient Flow in Silos - A Numerical Approach* by R.A. Link and A.E. Elwi, May 1987.

INCIPIENT FLOW IN SILOS

A NUMERICAL APPROACH

by

R.A. LINK

A.E. ELWI

Structural Engineering Report No. 147

Department of Civil Engineering

University of Alberta

Edmonton, Alberta, Canada

May 1987

Abstract

A finite element model to analyse incipient flow for cohesionless materials in silos is presented. The model is formulated on the principle of virtual work, and is based on small displacement theory. Wall friction is included in the formulation by the use of a thin layer interface element. The effects of load history are simulated by layering the bulk material in stages during filling and incrementally releasing the outlet force during incipient flow. Since time dependent constitutive parameters are not generally available, an elastic perfectly plastic material is used as a material model.

Model problems are analysed and the results for both initial filling and incipient flow cases are compared with classical theories. These model problems consist of a silo geometry with differing sets of wall interface and bulk material properties. In addition, recommendations for wall design loads are made.

ACKNOWLEDGEMENTS

This study was funded under the Natural Sciences and Engineering Research Council of Canada Operating Grant No. A5877. Thanks are due to Mrs. D. Nickel who drew the figures and to Dr. S.H. Simmonds for permission to use Fig. 2.10.

Table of Contents

List of Tables

List of Figures

List of Symbols

A	-	dimensionless constant.
B	-	hopper diameter.
$[B]$	-	strain-displacement matrix.
C	-	dimensionless constant.
C_{ijkl}	-	constitutive tensor.
$[C]$	-	constitutive matrix.
D	-	dimensionless stress distribution factor.
E	-	modulus of elasticity.
F_N, F_T	-	wall normal and tangential forces respectively.
$\{\bar{F}\},\{\bar{T}\}$	-	body forces and surface traction vectors respectively.
$f(\sigma_{ij})$	-	yield surface function.
f_{cu}	-	uniaxial compressive strength.
G	-	shearing modulus.
$g(\sigma_{ij})$	-	plastic potential function.
H	-	height of solid in silo cylinder.
I_1, J_2	-	first stress invarient and second deviatoric stress invarient respectively.
k_r	-	Jenike radial pressure coefficient.
K	-	lateral pressure coefficient.
$[K]$	-	stiffness matrix.
K_m	-	modulus number parameter.
m	-	geometry parameter.
N,T	-	wall normal and tangential force components at transition.
$[N]$	-	shape function matrix.

n - compressibility parameter.

p_a - atmospheric pressure.

Q_f - vertical force during flow at transition.

ΔQ_f - unbalanced vertical force at transition.

q - dimensionless force parameter.

$\bar{q}^0$ - prescribed kinematic constraints.

q_n, q_t - displacement components normal and parallel to the interface surface respectively.

$\{\underline{q}\}$ - nodal displacement vector.

$\{Q\}$ - equilibrating load vector.

$\{\Delta Q\}$ - unbalanced load vector.

r - coordinate ray.

R - hydraulic radius.

R_x - relaxation factor.

R_N, R_T - surface normal and tangential forces respectively.

$S_i(\theta)$ - dimensionless stress parameter during filling.

$S_f(\theta)$ - dimensionless stress parameter during flow.

$S_{\sigma k}$, S_{qk} - surfaces on which prescribed tractions and displacements, respectively, are applied.

S_{ij} - deviatoric stress tensor.

$\bar{T}^0, \bar{F}^0$ - prescribed surface tractions and body forces respectively.

t - exponent parameter.

V_k - element volume.

V_{fk} - interface element volume.

z_i - vertical switch height above apex.

z_{in} - vertical height above apex of peak pressure for initial filling stress distribution.

z_0 - vertical height above apex of hopper.

α, k - Drucker-Prager yield surface parameters.

β - angle of principal stresses at hopper wall.

γ - unit weight.

Δ - incremental change in.

δ - effective internal angle of friction.

δ_{ij} - Kronecker delta.

ϵ, $\{\epsilon\}$ - strain and strain vector respectively.

θ - coordinate angle.

θ' - hopper angle.

$\lambda_{q,P}$ - Euclidean norm displacement and load tolerances respectively.

μ' - coefficient of friction.

σ, $\{\sigma\}$ - stress and stress vector respectively.

σ_m - mean stress.

$\sigma_{r,\theta,a}$ - radial, circumferential, and out of plane stresses, respectively.

σ_a - initial filling wall pressure at apex.

σ_s - vertical surcharge pressure.

$\sigma_{t1,t2}$ - wall initial filling and flow pressures, respectively, at transition.

σ_{tr} - radial flow pressure at transition.

σ_J - Janssen vertical pressure.

$(\sigma'/\gamma B)$ - dimensionless stress parameter.

σ_{vw} - vertical stress at vicinity of wall.

$\bar{\sigma}_v$ - average vertical stress.

$\sigma_{1,2,3}$ - principal stresses.

σ_w - normal stress at wall vicinity.

τ_v - shear stress at wall vicinity.

τ_{limit} - Coulomb limiting shear stress.

τ_m - mean shear stress.

ϕ, c - Mohr-Coulomb yield surface parameters.

ϕ' - wall friction angle.

1. INTRODUCTION

1.1 Background

The subject of mass flow pressures in silos has come under increasing investigation by researchers in recent years. Mass flow refers to the continuous movement of all bulk solid in the silo during emptying. The problem lies mainly with the development of overpressures, both in the cylinder and in the hopper.

Steady state bulk solids flow has been extensively researched. Many experimental investigators (Jenike et. al. 1973, Walker and Blanchard 1967, Moriyama and Jotaki 1980, to name a few) confirm that a wall pressure reduction under static loads occurs in the lower region of a hopper. In addition, wall pressures were found to increase substantially over static pressures in a localized region near the transition from hopper to cylinder. It has been suggested by Jenike et. al. (1959-1973), Walker (1966), and Walters (1973), that these results are an equilibrium consequence of a switch in pressure fields at the transition from active to passive. Finite element results from Eibl and Häussler (1984) are in agreement with the concept of an arched passive field.

The subject of incipient flow has not drawn extensive research. Walker and Blanchard (1967), and Smith and Simmonds (1983), show limited experimental evidence of overpressures that do not occur at the transition. Most

other experimental investigators do not report on pressures other than those for steady state flow. Jenike (1968) and Walters (1973) contend that overpressures of this nature are due to a moving switch point, but so far no design practice has adopted this concept. The finite element analysis of Eibl and Häussler (1984) also shows a pressure increase in the hopper during the beginning stages of flow.

Askari and Elwi (1986) analysed a number of silo configurations using the finite element method. The results indicated that a localized overpressure existed at the silo outlet during flow. Unfortunately, it is possible that a static arch may have formed over the outlet which prevented flow. In addition, load and displacement convergence could not be obtained for weaker materials.

This study is a finite element investigation of incipient flow in silos, and is an attempt to model incipient flow conditions using a static elastic plastic incremental analysis.

1.2 Scope and Objectives of Thesis

The objectives of this thesis are as follows:

1. To provide an extensive review of the work of Jenike et. al. (1959-1973), and Walker (1966), since their approaches are the most commonly used in practice, and to clarify any misconceptions.
2. To develop a finite element representation that models the effects of nonlinear material behavior, wall

friction, and load history.

3. To run sample problems with different material properties, and to compare stress history, magnitude, and orientation to those predicted by classical theories for both initial filling and incipient flow conditions.
4. To make recommendations for design and further study based on observation of the finite element results.

1.3 Organization of Thesis

Chapter two is divided into three parts. The first part is an extensive literature review of the work of Jenike and Walker. The second part is a review of some of the research done in the area of finite element analysis. The last part of the chapter reviews some of the field measurements that were done on full scale silos.

Chapter three is a discussion of the formulation of the finite element problem. In Chapter four, the finite element model of the wall - bulk solid interface is presented. Chapter five is a discussion of granular material modelling.

Chapter six is divided into two parts. In the first part, the modelling of load history and outlet release procedures are described. Secondly, sample problems are run using the models described in earlier chapters, and results are compared to classical theories. The third part is a discussion of design situations involving incipient flow and "lock in" stresses. Finally, the reasons for lack of convergence of the silo problem are discussed.

Chapter seven contains the summary, recommendations for further study, and conclusions.

2. LITERATURE REVIEW

2.1 Introduction

There is extensive literature regarding the design, testing, and analysis of silo structures (Walli and Schwaighofer 1979). In this chapter, some of the major work done regarding silos and hoppers is examined. In the first part of the chapter, the classical theories by Jenike et. al. (1959-1973), Walker (1966), and Walters (1973) are reviewed. The finite element work that has been done regarding bulk solids flow is examined. Finally, the results of two selected silo testing programs (Walker 1966 and Smith and Simmonds 1983) are reviewed.

2.2 Radial Stress Fields - Jenike's Theories

In a series of papers, Jenike et. al. (1959-1973) formulated a number of theories on bin loads and design of axisymmetric and plane strain hoppers. Two distinct design criteria were examined; wall loads and flowability. Both initial filling and flow cases were considered in determining wall loads. Flowability criteria were given regarding outlet size to prevent the occurence of stable arching or the formation of a small channel in the material, known as piping. Only the design criteria regarding hopper loads are discussed here.

2.2.1 Bin Loading

Equilibrium expressions for bin loads were derived considering the stresses existing on a solid element in a channel as shown in Fig. 2.1. In deriving these expressions, Jenike (1961) makes the following assumptions:

1) The bulk material is assumed compressible during initial filling, and incompressible during flow.
2) For both initial and flow stress fields, a mean stress σ_m is assumed which increases linearly from the apex of the channel with coordinate ray, r, and is defined as

$$\sigma_m = \gamma r S_i(\theta), \qquad [2.1]$$

for initial filling and

$$\sigma_m = \gamma r S_f(\theta), \qquad [2.2]$$

for flow conditions, where $S_i(\theta)$ and $S_f(\theta)$ are dimensionless stress parameters for initial filling and flow conditions respectively. Equations 2.1 and 2.2 hold in the hopper as long as equilibrium is maintained in the physical system. This is discussed in more detail subsequently.
3) For initial stress fields, the ratio of the circumferential stress, σ_θ, to the radial stress, σ_r, is assumed to be constant

$$\frac{\sigma_\theta}{\sigma_r} = k_r. \qquad [2.3]$$

The coefficient k_r is analogous to Janssen's K factor,

and is dependent upon the compressibility and Poisson's ratio of the bulk solid (Jenike and Johanson 1968).

4) For flow stress fields, the material is assumed plastic, and the ratio of the major principal stress, σ_1, to the minor principal stress, σ_2, is assumed to be of the form

$$\frac{\sigma_1}{\sigma_2} = \frac{1 + \sin \delta}{1 - \sin \delta}, \qquad [2.4]$$

where δ is the effective angle of internal friction. A Mohr's circle representation of the stress state at a wall is shown in Fig. 2.2. The mean stress σ_m is the consolidating stress which exists during flow. The Mohr's circle is tangent to the actual yield locus (YL) and the effective yield locus (EYL). The advantage of using the effective yield locus is that material behavior at yield can be modelled with one yield locus. If the actual yield locus were used, a family of these curves would result, since it expands and contracts with changes in σ_m (Jenike and Shield 1959).

5) The material at the wall is assumed to slip, thereby developing the full kinematic angle of wall friction ϕ'.

The solution to the initial filling and flow stress fields proceeds in a similar manner. From the assumed stress relations and geometry, expressions are written for σ_r, σ_θ, and the out of plane stress σ_a. These expressions are inserted into the equilibrium equations for spherical coordinates. The resulting expressions are solved

numerically for the stress parameters $S_i(\theta)$ and $S_f(\theta)$ for specified problem parameters (ϕ', k_r, and hopper angle θ' for initial filling; ϕ', δ, and θ' for flow).

2.2.2 Initial Filling

As mentioned previously, Eqs. 2.1 and 2.2 are valid in the hopper as long as equilibrium is maintained. In the case of a hopper with no surcharge (Fig. 2.3a), the radial field can only be maintained below a certain level, z_{in}. Above that level, overall equilibrium warrants a reduction in wall pressure, terminating in $\sigma_\theta = 0$ at $z = z_0$. From z_{in} to z_0, a linear distribution is assumed.

In an actual bin, a surcharge is present which is equivalent to Janssen's vertical pressure in the cylinder at the transition. If a surcharge is added, the hopper walls above z_i must carry the additional load (Fig. 2.3b).

Major principal stresses during filling line up close to the vertical direction. This stress field is referred to as active.

Since the determination of $S_i(\theta')$ is complex, Jenike et. al. (1973) proposed a simplification. If a hydrostatic pressure distribution is assumed, the pressure at the apex can be derived as

$$\sigma_a = \frac{\gamma B}{2(\tan \theta' + \tan \phi')}. \qquad [2.5]$$

For a hopper with a vertical surcharge pressure, σ_s, the pressure at the transition, σ_{t1}, can be expressed as

$$\sigma_{t1} = \sigma_s \left[\frac{2 + m}{1 + m}\right] \frac{\tan \theta'}{\tan \theta' + \tan \phi'} , \qquad [2.6]$$

where m is a geometry parameter which equals 0 for plane strain, and 1 for axisymmetry. Between the top and the apex, one can interpolate linearly for a pressure value (Fig. 2.4).

2.2.3 Flow Pressures

As flow is initiated, the major principal stresses switch from a vertical to a horizontal direction, forming an arched (passive) field, as shown in Fig. 2.5a for no surcharge, and Fig. 2.5b with surcharge. In the case of no surcharge, the flow wall pressures are obtained in the same manner as initial filling pressures by considering overall equilibrium of the system. The flow radial stress field is substituted for the initial filling stress field.

As flow progresses, a plastic passive field is developed below the switch point, and moves upwards as the switch point moves upward. Below the switch point, pressures reduce from initial filling values in accordance with the flow radial stress field bound. This causes a net loss in equilibrium. If the bin is not to move, the unbalanced load (equivalent to the shaded regions in Figs. 2.5a and 2.5b) must be balanced in a region above the switch point. The imbalance is treated as a concentrated compressive load acting over an arbitrary distribution depth at the switch point.

It is generally assumed that the switch moves up the hopper. Hence the switch forces are considered short lived. Only the stable overpressure, which occurs as the switch point arrests at the transition, is considered in design. The solution for the transition overpressure, σ_{t2}, is arrived at (Jenike 1964) by consideration of vertical equilibrium at the transition. The magnitude of the unbalanced vertical force at the transition, ΔQ_t, is obtained as the difference between the force at filling (assuming Janssen's stresses) and the force during flow, Q_f. The force Q_f may be obtained as

$$Q_f = q\gamma B^{2+m}. \qquad [2.7]$$

where B is the hopper diameter at the transition, and q is a dimensionless parameter obtained by integrating the vertical components of the radial stress field over the transition cross-sectional area. Charts for q as a function of θ' , δ, and ϕ' have been developed by Jenike (1961). The flow force Q_f is expressed in units of force for axisymmetric hoppers, and force/metre for plane strain hoppers.

The unbalanced vertical force, ΔQ_t, is equilibrated by vertical components of wall normal and tangential transition forces N and T respectively, where

$$T = N \tan \phi'. \qquad [2.8]$$

These forces are assumed to act as a triangular pressure distribution over a slant height of 0.3B (Jenike 1973). The

value of the peak transition pressure, σ_{t2}, is obtained as

$$\sigma_{t2} = \sigma_{tr} + \frac{3.3(\sigma_J - (4/\pi)^m q\gamma B)}{(2 - 0.4 \sin \theta')^m(\sin \theta' + \cos \theta' \tan \phi')}, \quad [2.9]$$

where σ_J is the vertical Janssen pressure at the transition, and can be expressed as

$$\sigma_J = \frac{\gamma R}{\mu' K}(1 - e^{-\mu' KH/R}), \quad [2.9a]$$

where R is the hydraulic radius of the silo cylinder, μ' is the coefficient of friction of the wall-material interface (equivalent to tan ϕ'), H is the height of solid in the cylinder, and K is the Janssen lateral pressure coefficient.

The radial transition pressure, σ_{tr}, is determined by the solution of the radial stress field at the transition. Values for σ_{tr} are expressed as

$$\sigma_{tr} = (\sigma'/\gamma B)\gamma B, \quad [2.10]$$

where $\sigma'/\gamma B$ is a dimensionless stress parameter analogous to $S_f(\theta)$. Charts for this parameter have also been developed by Jenike (1961).

The final design envelope for the hopper region is as shown in Fig. 2.5c. Jenike et. al. (1973) compared pressure measurements of a model silo to this design envelope and found agreement.

2.3 The Differential Slice Approaches by Walker and Walters

Walker (1966) obtained a solution to the steady state flow in converging channels by considering equilibrium of a differential slice of material, shown in Fig. 2.6. The following assumptions were made:

1) Material yielding is governed by the Jenike effective yield locus (EYL), shown in Fig. 2.2. The stress field in the hopper is assumed passive during flow, and hence the ratio of principal stresses is given by Eq. 2.4.

2) The shear stress at the vicinity of the wall, τ_v, is related to the vertical stress at the wall, σ_{vw}, as

$$\tau_v = A\sigma_{vw}, \qquad [2.11]$$

where A is a constant.

3) The vertical stress, σ_{vw}, is related to the average vertical stress $\bar{\sigma}_v$ by

$$\sigma_{vw} = D\bar{\sigma}_v, \qquad [2.12]$$

where D is a stress distribution factor which takes into account the variation in vertical stress across the cross section. The parameter D is normally taken as 1.0 (Janssen's assumption)

Considering equilibrium of the slice dz under its own weight, the vertical stress field $\bar{\sigma}_v$, and the shear stresses τ_v, one can write a differential equation of equilibrium only in terms of $\bar{\sigma}_v$

$$\frac{d\bar{\sigma}_v}{dz} - C\,\frac{\bar{\sigma}_v}{z} = -\gamma. \qquad [2.13]$$

The solution is obtained as

$$\bar{\sigma}_v = \frac{\gamma z}{C - 1}\left[1 - \left[\frac{z}{z_0}\right]^{C-1}\right] + \sigma_J\left[\frac{z}{z_0}\right]^{C}, \qquad [2.14]$$

where

$$C = \frac{(m + 1)D}{\tan \theta'}\left[\frac{\sin \delta \sin 2(\theta' + \beta)}{1 - \sin \delta \cos 2(\theta' + \beta)}\right], \qquad [2.15]$$

and

$$\beta = \frac{1}{2}\left[\phi' + \text{Arcsin}\left[\frac{\sin \phi'}{\sin \delta}\right]\right]. \qquad [2.16]$$

The expression for the wall pressures σ_w is found by transforming σ_{vw} to local coordinates by using Eq. 2.16a

$$\sigma_w = \frac{1 + \sin \delta \cos 2\beta}{1 - \sin \delta \cos 2(\theta' + \beta)}\,\sigma_{vw}. \qquad [2.16a]$$

Walker and Blanchard (1967) performed some experimental pressure measurements in full scale silos and hoppers and concluded that pressures calculated with D = 1 gave a good fit of data points. This method is relatively simple compared to Jenike's (1964), which involves a rigorous solution of the radial stress field.

Walters (1973) proposed a more rigorous solution of the differential slice. Shear stresses acting on the slant height of the wall were considered, as shown in Fig. 2.7. In addition, an exact value of D was derived. The solution was extended to accommodate both initial filling (active) and flow (passive) stress states.

The solution to the resulting differential equation was similar in form to that of Walker's (1966), and was applicable to calculation of the switch stress at any switch point z_i. The author suggested that structural design should proceed on the basis of an envelope of these switch stresses.

An envelope of wall switch pressures were calculated for a silo with $\delta = 50°$, $\phi' = 25°$, and $\theta' = 4°$. Switch stresses were many times over the static pressures (the ratio of switch to static pressure at the transition was approximately 40), and were distributed over a relatively small depth. These pressures are high compared to those of Jenike and Walker, and design on the basis of the switch pressure envelope is overly conservative.

In calculating initial pressures, the assumption was made that the stress field in the hopper was plastic active. This assumption is unjustified, since the bulk solid is compressed triaxially, and is likely elastic because of high mean stresses and low shearing stresses.

2.4 Finite Element Studies

Although there have been numerous papers (Jofriet et. al. 1977, Chandrangsu and Bishara 1978) dealing with static bin loads, there have been few papers which attempt a flow solution.

Eibl and Häussler (1984) developed a nonlinear incremental viscoplastic formulation in which material

stress increments were divided into rate dependent and rate independent components. The formulation included both inertial and viscous effects and was developed along streamlines so that incompressibility was maintained during flow. The rate independent component of stress was assumed to be bounded by the yield surface proposed by Lade (1978), which considered plastic contractive and expansive strain components. The rate dependent stress component was assumed to be of a form analogous to Newtonian flow, relating stress increments to strain rates. Coulomb friction was assumed along the walls except at the outlet, where a condition of zero stress was enforced. The problem was formulated in an Eulerian frame of reference, relating velocities to a fixed spatial mesh.

Initial pressures were obtained for two silos of differing hopper inclination, and results compared favorably with experimental pressures obtained by Motzkus (1974). Flow pressures were then obtained for a 6.5 ft. (1.98 m.) by 39 ft. (11.88 m) plane strain silo with an outlet diameter of 3.3 ft. (1.01 m.). The principal stress directions and wall pressure distributions compared favorably with those predicted by Jenike et. al. (1973), Walker (1966), and Walters (1973), although the authors made no numerical comparisons.

The silo that was analysed had a fairly large outlet diameter in relation to the cylinder diameter. Such a silo would not exist in practice. It would have been more

convincing to analyse a silo with a more practical outlet diameter, following the guidelines suggested by Jenike (1961) or Walker (1966).

In addition, the outlet constraint of zero wall stress does not exist. Figure 2.8 shows the consequence of that assumption. Instead of following the wall when leaving the hopper, the material point is unrestrained, and falls vertically. There is nothing to stop the material from moving into the wall (having a nonzero velocity component normal to the silo wall).

Askari and Elwi (1986) proposed using a double iterative scheme to solve the silo problem. Initially, the silo material displacements are obtained with all wall tangential forces F_T equal to zero. Then, tangential forces are obtained as

$$\{F_T\} = R_x\{F_N\}\tan \phi', \qquad [2.17]$$

where $\{F_N\}$ are the wall normal forces, and R_x is a predetermined relaxation factor less than 1.0 used to maintain solution stability. Equation 2.17 is transformed to the global axes and added to the silo load vector. The nonlinear iteration for material stresses represents the first loop, and the iteration for frictional forces represents the second loop of the iteration cycle. The iterative cycle is continued until specified load, displacement, and friction force tolerances are met. The Drucker-Prager yield criterion was used for material

yielding.

In all, 12 silos with varying geometries and material parameters were analysed in an attempt to perform a parametric study. The silos were analysed using "single step switch on" gravity loading instead of using layers of material elements. The results indicated a good agreement with Janssen cylinder pressures, but a substantial increase over Jenike's maximum hopper pressures was observed. The author attributed the increase in pressures to the conservative strength characteristics and extreme dilatency ratios of the Drucker-Prager yield surface. Large overpressures existed at the outlet and transition regions.

Plots of plastified points seem to indicate an elastic stress field in the hopper for all cases considered. The increase in hopper pressures directly contradicts the pressure decrease assumed in most flow pressure theories and found in many experimental measurements. The overpressure at the outlet may be the result of elastic arching occuring there which would prevent flow. The results just described are consistent with the formation of a stable static pressure field, which means that flow is not taking place.

2.5 Experimental Studies

Walker and Blanchard (1967) performed a series of pressure measurements during initial filling and flow conditions on three steel hopper configurations shown in Fig. 2.9. Load diaphragms mounted flush to the silo wall

were used to record measurements. In addition, during some tests a water filled pressure bladder was inserted into the silo at various depths to record vertical pressures.

Although there was a substantial scatter in test results, the results during flow showed a general pressure decrease in the lower hopper region, and a pressure increase in the upper hopper region over pressures at initial filling. The flow pressure magnitudes and distribution were found to be relatively independent of flow rate. Results were close to the distributions predicted by Walker (1966). In addition, flow pressures were observed to "lock in" if flow was stopped.

Smith and Simmonds (1983) performed pressure measurements on a full scale coal silo in Elkford, B.C. (See Fig. 2.10). The silo was axially symmetric in the cylinder region, converging into 2 pyramidal hoppers. Strain gauges were mounted at the gauge locations shown in Fig. 2.10. Cylindrical pressure vessel theory was used to relate normal wall stresses to hoop strains.

Overpressures were detected at gauge locations 3, 4, and 5 that were satisfactorily bounded by Jenike's minimum strain energy field. At gauge 6, there were no observed overpressures. In addition, there was evidence of "locked in" overpressures once flow was terminated. The authors recommended the use of overpressure factors (ratio of flow switch pressures to static pressures) in design. In addition, the authors further suggested that the larger

stresses of Jenike's minimum strain energy distribution and ACI 313-77 should be used to design the cylinder region.

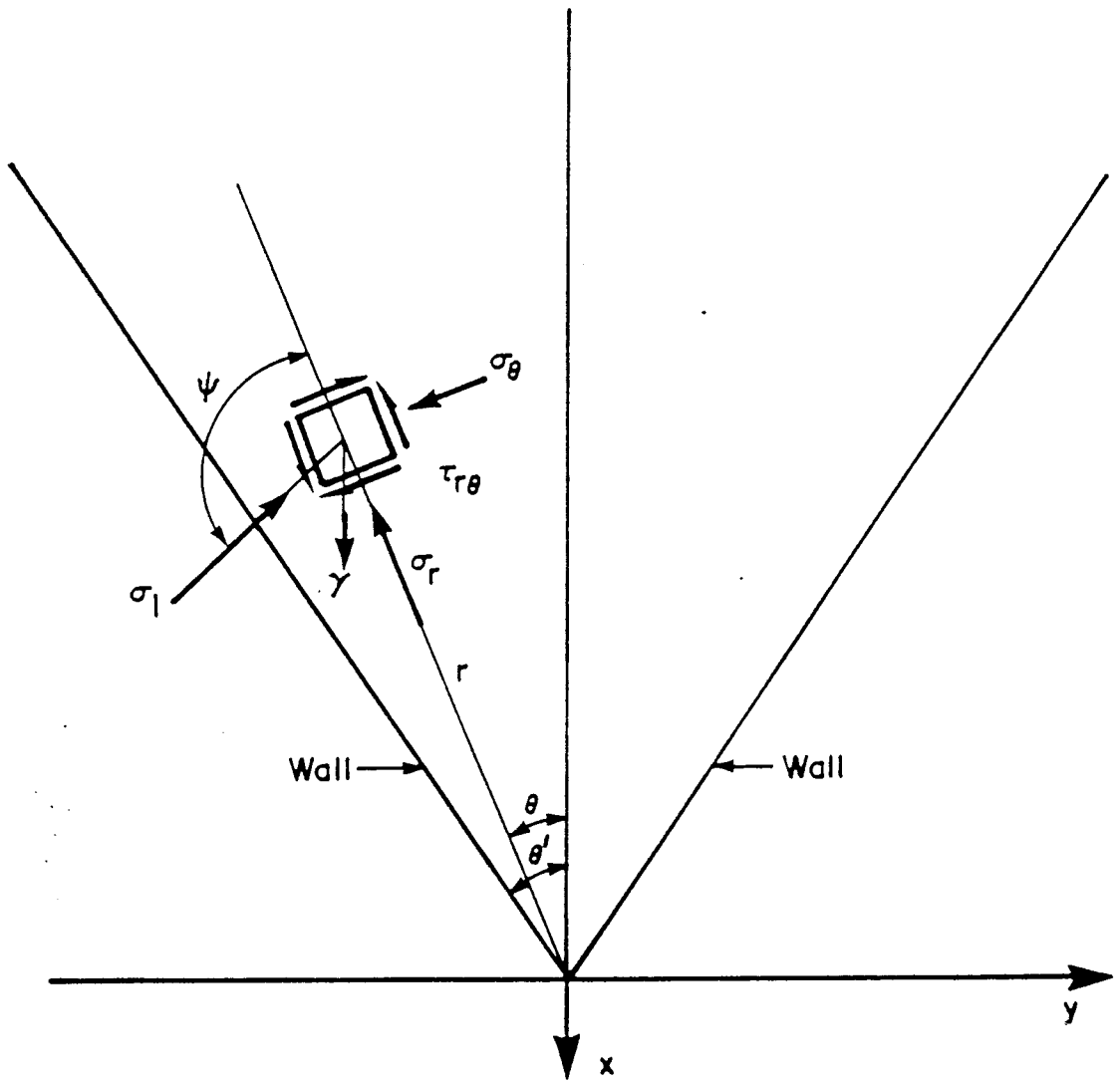

Figure 2.1 Stress on an element of solid

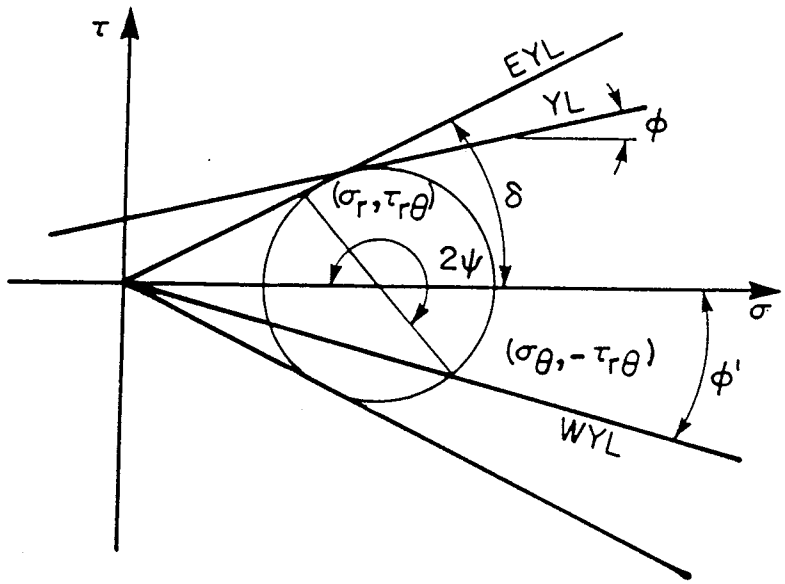

Figure 2.2 Mohr's circle representation

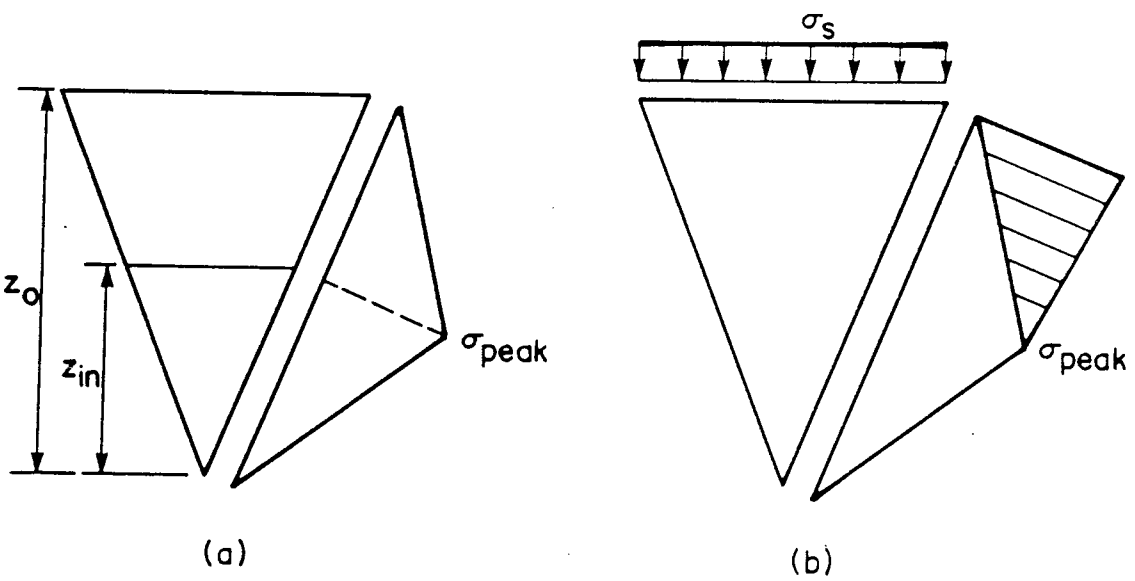

Figure 2.3 Initial filling pressures

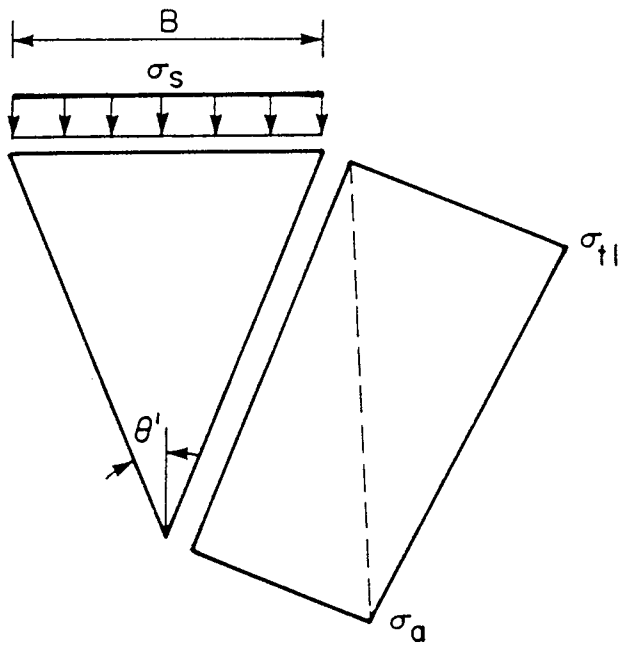

Figure 2.4 Design initial filling pressures

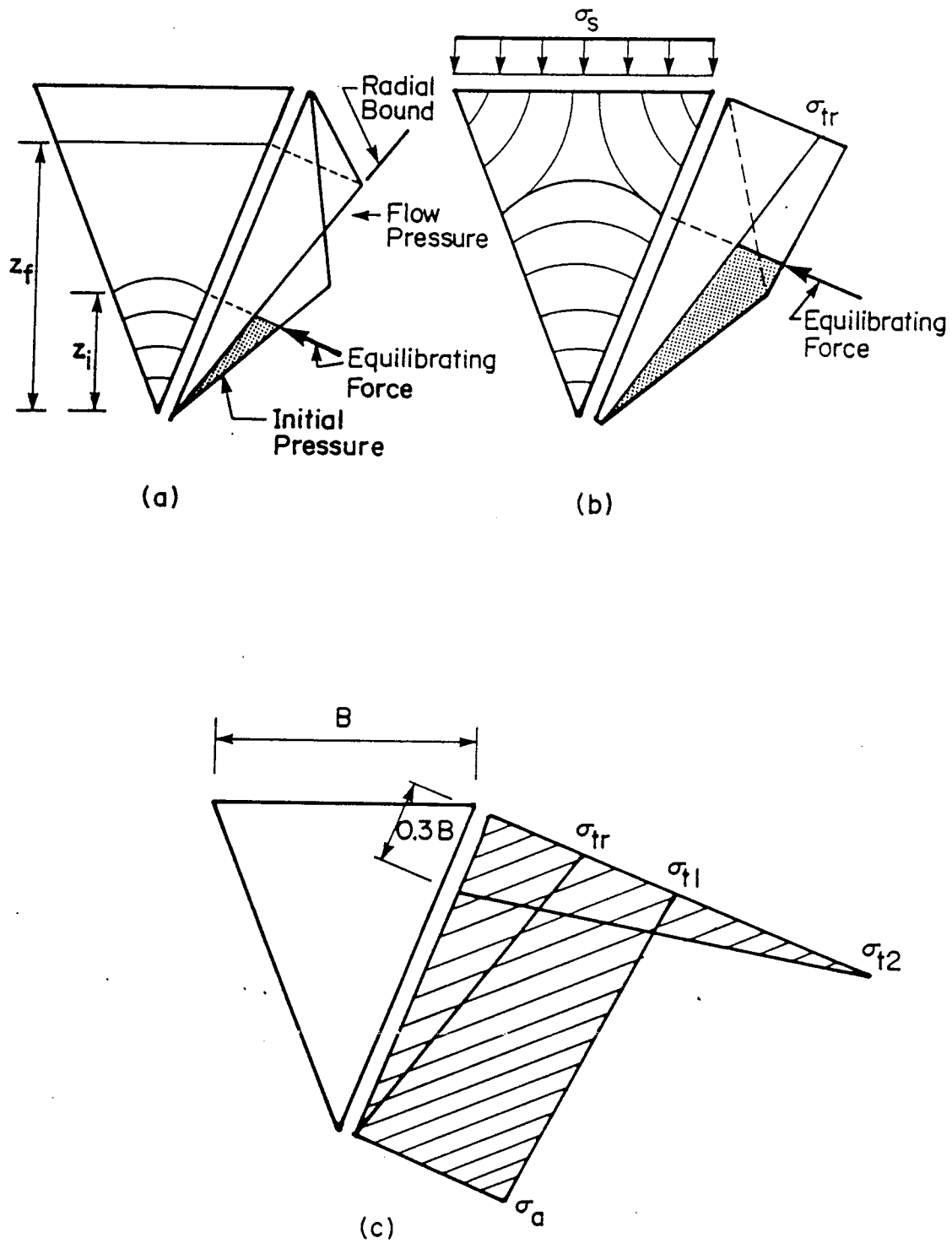

Figure 2.5 Flow pressures and design curves

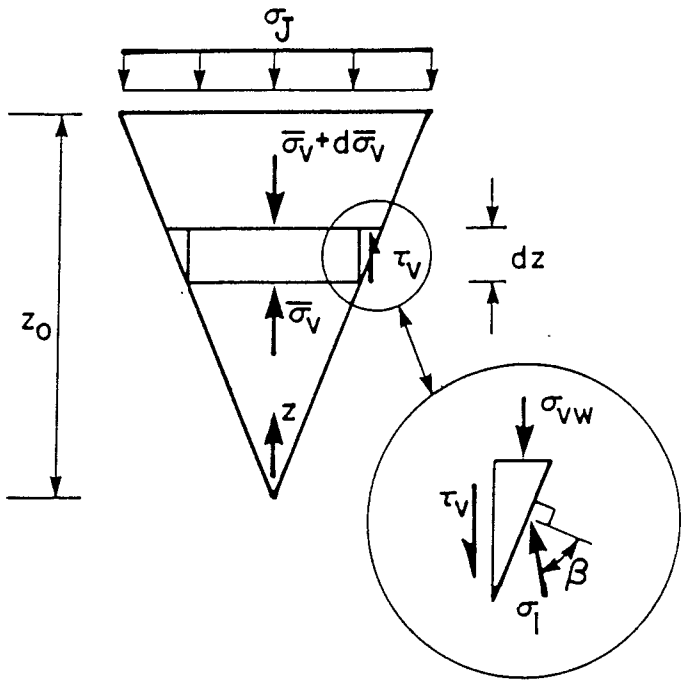

Figure 2.6 Walker's differential slice

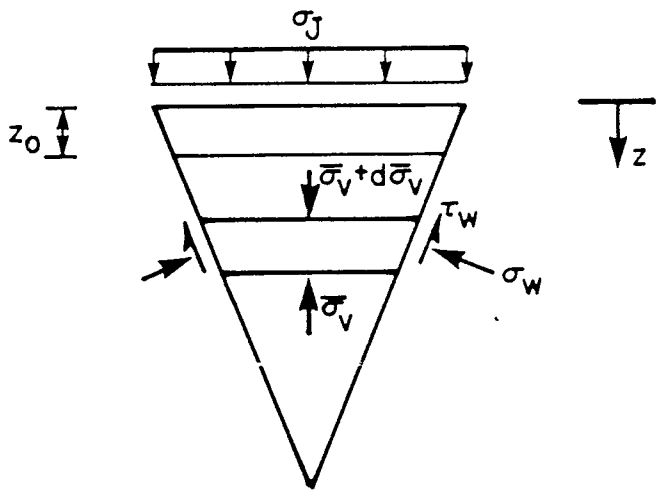

Figure 2.7 Walters' differential slice

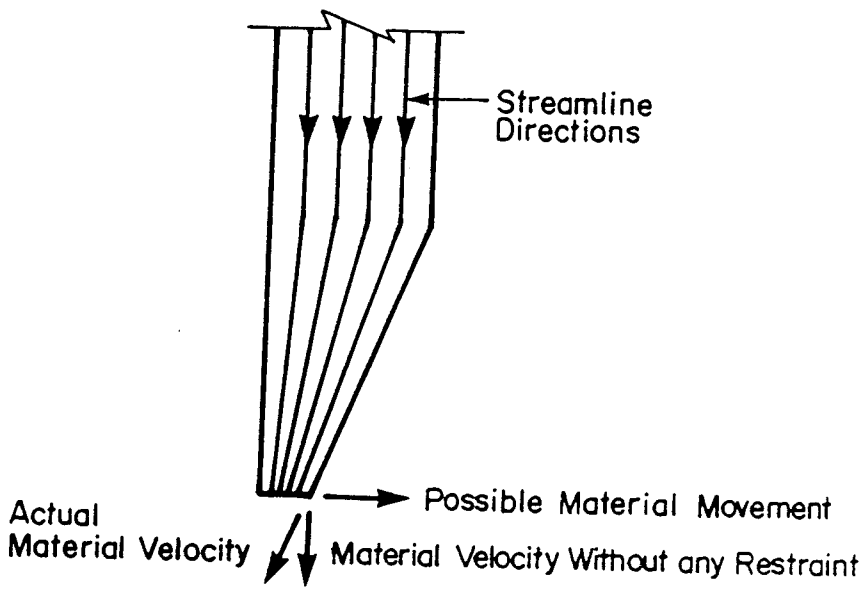

Figure 2.8 Assumption of zero outlet pressure

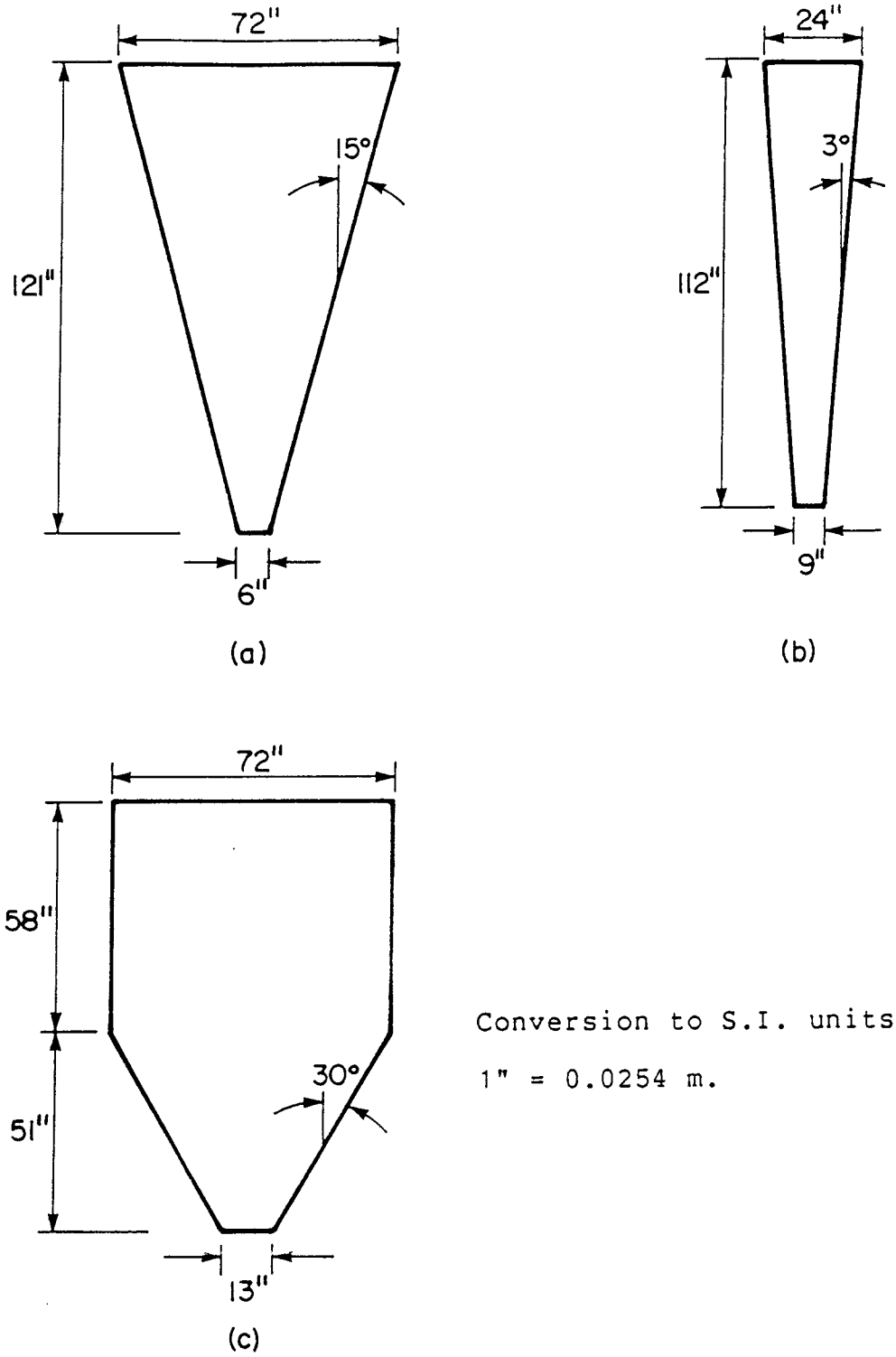

Conversion to S.I. units:

1" = 0.0254 m.

Figure 2.9 Walker's experimental hoppers

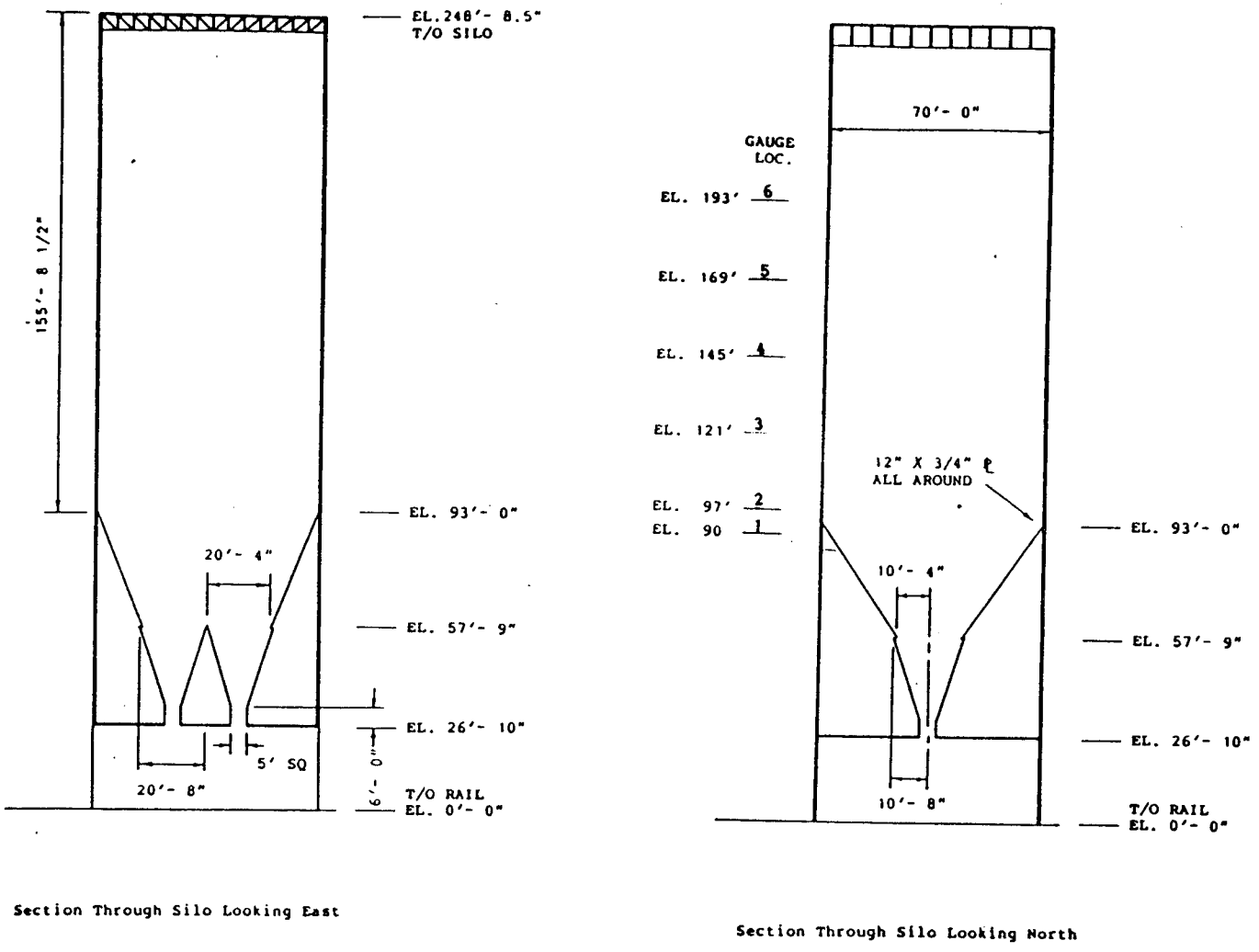

Figure 2.10 Elkford silo (Smith and Simmonds 1983)

3. PROBLEM FORMULATION

3.1 Introduction

Using the principle of virtual work, the structural response of the ensiled material and the frictional interface is formulated in an incremental sense, and is based on small displacement fields. Material and frictional nonlinearities can be readily included in the formulation.

3.2 Variational Formulation

Consider a mechanical system at a certain load step in equilibrium under a set of prescribed tractions $\bar{T}^0$, body forces $\bar{F}^0$, and kinematic constraints $\bar{q}^0$. Let the body in Fig. 3.1 be divided into "k" number of elements. Let V_k denote the element volume and $S_{\sigma k}$, S_{qk} be those portions of element surfaces on which prescribed tractions and displacements, respectively, are applied. Also, assume that the frictional surface is approximated by a thin layer and denote the volume of that layer on the element surfaces as V_{fk}. The prescribed body forces and surface tractions are in equilibrium with the internal stresses σ_{ij}^0 and the frictional stresses σ_{ij}^{f0}. The displacement field q^0 is compatible with the strains ϵ_{ij}^0 and ϵ_{ij}^{f0}.

If the structure is loaded with increments of traction $\Delta\bar{T}$, body forces $\Delta\bar{F}$, and kinematic constraints $\Delta\bar{q}$, the stress and strain increments $\Delta\sigma_{ij}$, $\Delta\epsilon_{ij}$ and $\Delta\sigma_{ij}^f$ are generated. This load increment, or load step, is the case for which a

solution is desired.

The principle of virtual work states that the sum of all virtual work δW done by the external and internal forces in going through a set of infinitesimal arbitrary displacements $\delta\Delta q_i$ satisfying prescribed kinematic constraints is zero ie. $\delta W = 0$. Thus,

$$\delta W = \sum_k \Big[\int_{V_k} \Delta\sigma_{ij}\delta\Delta\epsilon_{ij}dV + \int_{V_{fk}} \Delta\sigma^f_{ij}\delta\Delta\epsilon_{ij}dV$$

$$+ \int_{V_k} \sigma^0_{ij}\delta\Delta\epsilon_{ij}dV + \int_{V_{fk}} \sigma^{f0}_{ij}\delta\Delta\epsilon_{ij}dV$$

$$- \int_{V_k} (F^0_i + \Delta F_i)\delta\Delta q_i dV - \int_{S_{\sigma k}} (T^0_i + \Delta T_i)\delta\Delta q_i dV \Big] = 0. \qquad [3.1]$$

In this study, evaluation of the frictional work terms is based on the assumption that the work done on a frictional surface can be approximated by the work done on a thin boundary layer if the normal stiffness of the thin layer is large, i.e.

$$\int_{S_{fk}} \sigma_T \delta\Delta q_T dS \approx \int_{V_{fk}} (\sigma^{f0}_{ij} + \Delta\sigma^f_{ij})\delta\Delta\epsilon_{ij}dV. \qquad [3.2]$$

Finite element matrices can now be generated from Eq. 3.1. The strain increment tensor is related to the displacement field tensor by

$$\Delta\epsilon_{ij} = \frac{1}{2}(\Delta q_{i,j} + \Delta q_{j,i}). \qquad [3.3]$$

The displacement field can be written in terms of nodal quantities as

$$\{\Delta q\} = [N]\{\Delta \underline{q}\}. \qquad [3.4]$$

where [N] is a matrix of shape functions. If Eq. 3.2 is rewritten in matrix form, the incremental strain - displacement relationship is obtained as

$$\{\Delta \epsilon\} = [B]\{\Delta \underline{q}\}, \qquad [3.5]$$

where [B] is a displacement derivative operator matrix.

Within the bulk material, the stress increment tensor is related to the strain increment tensor as

$$\Delta \sigma_{ij} = C_{ijkl}\Delta \epsilon_{kl}, \qquad [3.6]$$

or, in matrix form

$$\{\Delta \sigma\} = [C]\{\Delta \epsilon\}. \qquad [3.7]$$

It is assumed that the concept of Eq. 3.6 holds true for the friction layer as well, i.e.

$$\{\Delta \sigma\}^f = [C]^f\{\Delta \epsilon\}. \qquad [3.8]$$

If Eqs. 3.3 to 3.8 are substituted into Eq. 3.1, and the necessary variations are carried out, Eq. 3.1 is written as

$$\sum_k \langle \delta\Delta\underline{q} \rangle \Big[\Big(\int_{V_k} [B]^T [C][B] dV + \int_{V_{fk}} [B]^T [C]^f [B] dV \Big) \{\Delta\underline{q}\}$$

$$+ \int_{V_k} [B]^T \{\sigma^0\} dV + \int_{V_{fk}} [B]^T \{\sigma^{f0}\} dV - \int_{V_k} [N]^T \{\bar{F}^0\} dV$$

$$- \int_{V_k} [N]^T \{\Delta F\} dV - \int_{S_{\sigma k}} [N]^T \{\bar{T}^0\} dS - \int_{S_{\sigma k}} [N]^T \{\Delta T\} dS \Big] = 0. \qquad [3.9]$$

Equation 3.9 can be reduced to the form

$$\langle \delta\Delta\underline{q} \rangle [K] \{\Delta\underline{q}\} = \langle \delta\Delta\underline{q} \rangle \{\Delta Q\}, \qquad [3.10]$$

where,

$$[K] = \sum_k \Big[\int_{V_k} [B]^T [C][B] dV + \int_{V_{fk}} [B]^T [C]^f [B] dV \Big], \qquad [3.11]$$

$$\{\Delta Q\} = \{\bar{F}\} + \{\bar{T}\} - \{Q\}. \qquad [3.12]$$

The terms of Eq. 3.12 are defined as

$$\{\bar{F}\} = \sum_k \Big[\int_{V_k} [N]^T \{\bar{F}^0\} + \int_{V_k} [N]^T \{\Delta F\} dV \Big], \qquad [3.13]$$

$$\{\bar{T}\} = \sum_k \Big[\int_{S_{\sigma k}} [N]^T \{\bar{T}^0\} + \int_{S_{\sigma k}} [N]^T \{\Delta T\} dV \Big], \qquad [3.14]$$

$$\{Q\} = \sum_k \Big[\int_{V_k} [B]^T \{\sigma^0\} dV + \int_{V_{fk}} [B]^T \{\sigma^{f0}\} dV \Big]. \qquad [3.15]$$

The terms $\{\bar{F}\}$ and $\{\bar{T}\}$ refer to the work equivalent body force and surface traction vectors, and $\{Q\}$ is the equilibrating load vector.

Since $<\delta\Delta\underline{q}>$ has arbitrary values, Eq. 3.10 becomes

$$[K]\{\Delta\underline{q}\} = \{\Delta Q\}. \qquad [3.16]$$

Equatiom 3.16 represents the usual stiffness equations resulting from a displacement formulation.

3.3 Non-Linear Solution Strategy

The finite element model described in the previous section is a displacement model. It satisfies kinematic compatiblility everywhere and approximately satisfies equilibrium only on a global level. The set of linear algebraic equations (Eq. 3.16) are considered a piecewise linearization of a non-linear structural response, and are solved for an increment of displacement, which yields an increment of strain. Stress increments are calculated by constitutive laws. Total stresses are updated either by direct addition of the stress increments, or by satisfaction of a governing stress condition (this method is necessary for the friction interface, where the increment of interface shear stress developed during slip is not constitutively dependent). When integrated over the volume of the structure, the total stresses yield the equilibrating loads $\{Q\}$.

The structural model is said to be in equilibrium if the unbalanced load $\{\Delta Q\}$ vanishes. If $\{\Delta Q\} \neq 0$, the stresses which satisfy the constitutive laws and governing stress conditions are not in equilibrium with the external loads.

One way to arrive at a state of stress that satisfies equilibrium is to eliminate the unbalanced load $\{\Delta Q\}$ through an iterative scheme.

The iterative scheme used in this study is known as the standard Newton Rhapson method, or tangential stiffness method. Fig. 3.2 qualitatively illustrates the tangential stiffness approach. The curved line represents the actual load - displacement response of the structure. The stiffness matrix K is first assembled as K_1, and a displacement increment Δq_1 is calculated corresponding to K_1. The equilibrating load Q_1 at displacement q_1 is less than the external load F + T. The stiffness matrix is reassembled as $K_2 \neq K_1$, and the structure is reloaded with an unbalanced load $\Delta Q_1 = F + T - Q$. This process is continued until convergence is achieved. Euclidean norms are used to form the criteria for convergence.

A pictorial description of Euclidean norm convergence is shown in Fig. 3.2. The symbols λ_q and λ_p represent relative absolute tolerances less than one, and are set arbitrarily by the program user. The values $\lambda_q\|q\|$ and $\lambda_p\|F + T\|$ represent the maximum allowed magnitudes of the errors in displacements and loads respectively. Point 3 in Fig. 3.2 has passed both error limits, and has, therefore, converged.

Acceptable values of λ_q and λ_p are problem dependent. In this study, a range of 0.01 to 0.03 was used for both tolerances.

The piecewise linearization of Eq. 3.16 requires that the load increment be reasonably small. If the structural response is path dependent, the resulting strain increment may still be large enough to cause the solution to drift. If the strain increment is divided into a number of smaller subincrements, better control of the solution is achieved. This is known as the subincrement method of updating stresses (Elwi and Murray 1980).

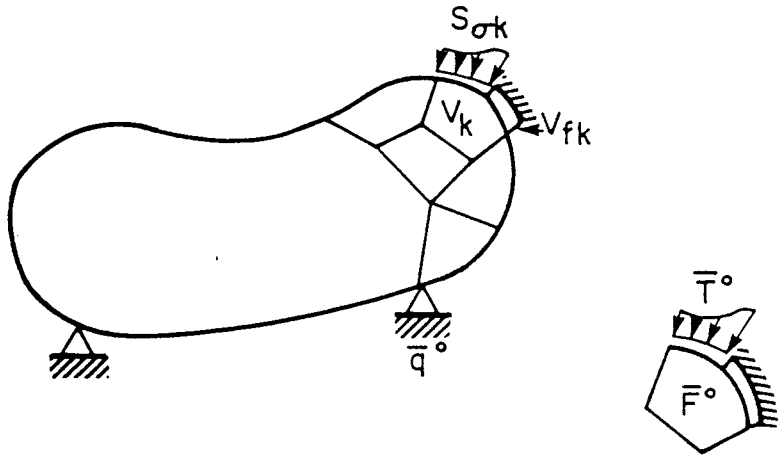

Figure 3.1 Structural configuration

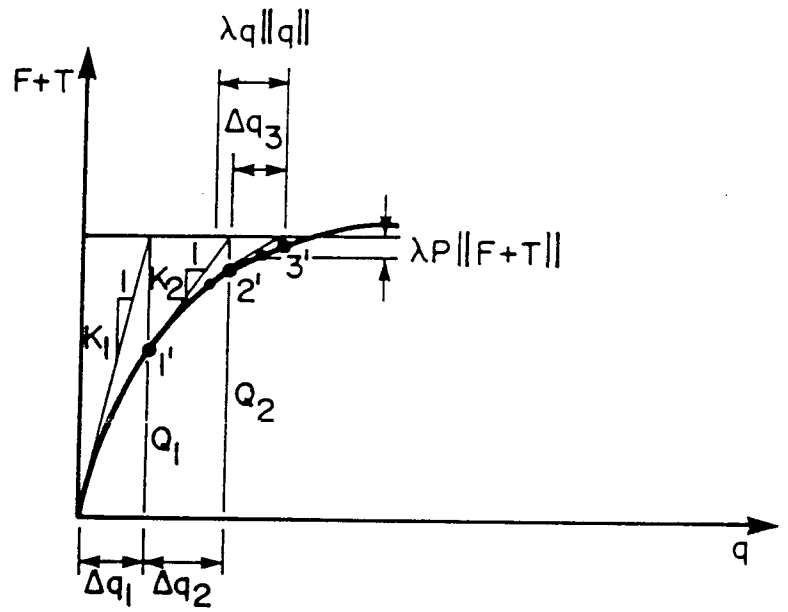

Figure 3.2 Modified Newton-Rhapson solution strategy

4. FRICTION MODEL

4.1 Introduction

Wall friction has a major influence on the magnitude of bin pressures. Therefore, it is important to include the frictional interface between material and wall in the formulation of the structural problem. The solution to the problem is both nonlinear and iterative in nature. In this chapter, an intuitive and practical solution to the friction problem is discussed. The element formulation is similar to an approach taken by Desai et. al. (1984). This involves using a thin interface element to describe interface behavior under loading.

In this study, Coulomb friction is assumed. Coulomb friction is a simple concept and requires only one parameter to describe sliding frictional behavior. Kinetic and adhesion effects are neglected, although the friction model can be modified to accommodate both.

The limiting equation for the Coulomb friction law can be expressed as

$$R_T = R_N \tan \phi', \qquad [4.1]$$

where R_N is compressive. Eq. 4.1 may be expressed in terms of stresses as

$$\tau_{limit} = \sigma \tan \phi', \qquad [4.2]$$

where ϕ' refers to the angle of friction of the interface.

It is assumed to remain constant under all loading conditions, and has different values for different wall - material combinations.

A simple model illustrates sliding frictional behavior. Consider a block of incompressible material resting in contact with a surface as shown in Fig. 4.1. The interface has an angle of friction ϕ'. The block is subjected to loads R_N and R_T acting in the normal and tangential directions respectively. Three states may now be identified to govern the relation between R_T and R_N

$$|R_T| < R_N \tan \phi', \qquad [4.3]$$

$$R_T = R_N \tan \phi', \qquad [4.4]$$

$$R_T = R_N = 0. \qquad [4.5]$$

The three states are referred to as stick, slip, and debond in that order. When an increment of shear ΔR_T and an increment of normal force ΔR_N are added to the system, the interface may pass between the three states in a manner discussed in detail subsequently. In this case, $(R_N + \Delta R_N)$ is the independent variable and R_T is determined accordingly. The remainder of ΔR_T and/or ΔR_N beyond that allowed by Eqs. 4.3, 4.4, and 4.5 must be redistributed.

Equations 4.3 to 4.5 may be referred to as force type constraints. Corresponding displacement constraints can be derived in the form

$$q_t = 0, \quad q_n = 0 \qquad \text{(stick)} \qquad [4.6]$$

$$q_t \neq 0, \quad q_n = 0 \qquad \text{(slip)} \qquad [4.7]$$

$$q_t \neq 0, \quad q_n > 0 \qquad \text{(debond)} \qquad [4.8]$$

where q_t and q_n refer to tangential and normal displacements respectively.

Coulomb friction may be introduced in a finite element program in many ways. The boundary integral approach (Jofriet et. al. 1977) is rejected on the premise that the resulting formulation is unsymmetric and requires special equation solving programs. In addition, the method is based on the assumption that the full frictional boundary is slipped, which may not be the case. The iterative process adopted by Askari and Elwi (1986) is also rejected. This method also assumes full frictional boundary slippage. In this study, a thin interface element with specific material properties designed to satisfy Eqs. 4.3 to 4.8 is adopted.

4.2 Model Description

4.2.1 Representation of Interface States

As described earlier, it is proposed to use a thin interface element to model friction effects. This element (shown in Figure 4.2) must have material properties that enforce the necessary constraints for stick, slip, and debond.

Adopting an incremental approach based on displacement formulation, an increment of stress is obtained in terms of an increment of strain as

$$\{\Delta\sigma\} = [C]\{\Delta\epsilon\}. \qquad [4.9]$$

where [C] is the constitutive matrix.

In an axisymmetric formulation only four components of the stress and strain tensors exist. Of these, the only stress increments of concern are the stress component $\Delta\sigma_1$ normal to the interface and the corresponding shear component $\Delta\tau_{12}$. All other stress increments are zero. This relation may be described as

$$\begin{Bmatrix} \Delta\sigma_1 \\ \Delta\sigma_2 \\ \Delta\sigma_3 \\ \Delta\tau_{12} \end{Bmatrix} = \begin{bmatrix} E_1 & 0 & 0 & 0 \\ 0 & 0 & 0 & 0 \\ 0 & 0 & 0 & 0 \\ 0 & 0 & 0 & G_{12} \end{bmatrix} \begin{Bmatrix} \Delta\epsilon_1 \\ \Delta\epsilon_2 \\ \Delta\epsilon_3 \\ \Delta\gamma_{12} \end{Bmatrix} \qquad [4.10]$$

Physically, [C] represents the normal and tangential stiffness of the interface. Strain (and displacement) conditions are dependent upon the values in [C]. Also, it can be said that the total stresses $\{\sigma\}$ represent the force conditions that exist at the interface. If this is true, then [C] and $\{\sigma\}$ can be used to describe the three frictional states of slip, stick, and debond.

In the stick state ($\tau_{12} < \sigma_1 \tan \phi'$), no relative movement occurs along or against the friction surface (Eq. 4.6). To enforce these two constraints, arbitrarily large

values of E_1 and G_{12} are used. This ensures small movements since the corresponding strains are small. There are no force constraints because the interface can carry the full stresses σ_1 and τ_{12}.

As the slip state is initiated ($\tau_{12} \geq \sigma_1 \tan \phi'$), no relative movement occurs in the normal direction (Eq. 4.7). However, movement does occur in the tangential direction because the limit condition is exceeded. If a stress - strain plot of the interface is examined (Fig. 4.3), it can be seen that once slip starts, the shear stiffness G_{12} of the interface reduces to zero. This means that G_{12} must be set to zero. In addition, the force constraints specified in Eq. 4.4 must be enforced as

$$\tau_{12} = \frac{\tau_{12}}{|\tau_{12}|} |\sigma_1| \tan \phi'. \qquad [4.11]$$

For debonding ($\sigma_1 \geq 0$), the surfaces no longer remain in contact. There is relative movement in both directions, and the effective stiffness of the interface is zero. In this case,

$$E_1 = G_{12} = \sigma_1 = \tau_{12} = 0. \qquad [4.12]$$

Table 4.1 shows the force constraints and the corresponding constitutive matrices for the three cases discussed above.

4.2.2 Change in Interface State

As an interface is loaded, it is possible that the interface state may change, e.g. from a stick to a slip condition. Normally, this is modelled by changing the force - displacement constraints to those of the new state within the load step. However, some state changes need to be given special consideration due to model limitations.

It is convenient to show state changes in the form of a decision matrix as shown in Table 4.2. The left column of the matrix denotes the old state, and the top row denotes the new state. The members of the matrix represent what conditions must occur for the change and what corresponding constraint changes need to be made. Most changes in the table are fairly obvious. However, some changes in state bear explanation.

If one surface has debonded from another, it means that there is some gap or separation of the two surfaces. Therefore, it is convenient to use the element normal strain ϵ_1 as an indicator of separation. If $\epsilon_1 < 0$ and the surface was previously debonded, the gap no longer exists, and the interface is under compression. At this point, the interface stresses are set to zero.

The case of debond to slip is not allowed. This is because the conditions for this change are not clearly defined, so it is assumed that a stepped path is taken to achieve this change ie. debond to stick to slip. This method is also used by Katona (1982).

Also, the case of slip to stick is not allowed. Once the interface has slipped in a given load step, it stays slipped. The assumption is made that once slipped, the final equilibrium position of the interface is at a limiting condition shear stress ($\tau_{12} = \sigma_1 \tan \phi'$). This assumption is used by many researchers for friction formulation (Katona 1982, Eibl 1984, Askari 1985, and Bishara 1979).

4.2.3 Computational Algorithm

Given the background theory of the model, the implementation of the model into a finite element program is now explained. In each load step an initial frictional state (usually stick) is assumed at selected sampling (Gauss) points on the interface. The structure is then loaded. Interface stresses and strains are calculated, and the interface condition at the Gauss points is checked (Table 4.2). If the interface state changes, corresponding changes are made to [C] and $\{\sigma\}$ from Table 4.2. The unbalanced load $\{\Delta Q\}$ is calculated and the structure is reloaded with $\{\Delta Q\}$ using the new interface state conditions. The process is repeated until convergence of loads and displacements is achieved.

Interface stresses are calculated using a simple material model. The model's function is to assign stiffnesses (displacement constraints) and stresses (force constraints) that correspond to the state of the interface. The flowchart for such a model is shown in Fig. 4.4.

To understand the logic flow, it is necessary to examine Fig. 4.4, step by step, noting that all calculations are for one Gauss point. In Step 1, global stress increments $\{\Delta\sigma\}_g$ are calculated. Next, the global stress components are transformed to the point local axes. The local axes are axes which define directions normal and parallel to the interface. The total local stresses $\{\sigma\}_l$ and global strains $\{\epsilon\}_g$ are updated in Step 3. As well, a global load step strain increment $\{\epsilon\}_{gls}$ is updated. The strain increment $\{\epsilon\}_{gls}$ represents the sum of the strain increments accumulated during the load step. The term $\{\epsilon\}_{gpls}$ refers to the total strain from the previous load step. When $\{\epsilon\}_{gls}$ is transformed to the local strain increment $\{\epsilon\}_{lls}$, the load step shear strain increment $(\gamma_{12})_{lls}$ determines the sign of the interface shear stress $(\tau_{12})_l$ during slip. This is useful in cases where the loading is reversed in subsequent load steps.

In Step 5, the interface state is checked, and appropriate stress (force) constraints are assigned. Also, a condition flag is assigned to the Gauss point. This flag is used to determine appropriate stiffness (displacement) constraints for the Gauss point (Step 6). Finally, $[C]_l$ and $\{\sigma\}_l$ are transformed to the global frame of reference (Step 7). These steps are repeated for all the Gauss points on the interface.

To simulate the permanent deformation that occurs during slip (see Fig. 4.3), the constitutive matrix $[C]_l$ for

each Gauss point is reset to $[C]_{stick}$ after each load step. This has the effect of inducing a permanent "set" if the interface is unloaded in a subsequent load step.

4.2.4 Limitations

The friction element described in this chapter has a number of advantages. It is formulated just like any other solid element, which makes it easy to implement in a finite element program. Adhesion and non-linear friction laws can be modelled fairly simply. The element converges rapidly for problems without severe stress gradients. However, there are some limitations as to its use.

In reality, the thickness of an interface is either zero or very small. Therefore, it is necessary for the interface element to be "thin", i.e. the element has a large aspect ratio. It is well known that large aspect ratios invite numerical trouble (Zienkiewicz 1977). In the silo problem, this shows up in the form of stress oscillations near the transition if the values of E_1 and G_{12} become too large for a given aspect ratio. To determine suitable parameters of E_1 and G_{12}, it is necessary to perform parametric studies with varying aspect ratios. This may only amount to varying E_1 and G_{12} until the oscillations are small or have disappeared, which is the approach followed here. Alternatively, an error balancing method involving penalty functions (Zienkiewicz 1977) may be used.

In the model, the process of rebonding a debonded element is not done entirely correctly. This can be illustrated by examining Fig. 4.5. Assume that the element started out in configuration C_1 with Gauss point #1 debonded. The interface would have zero stiffness and would be free to increase or narrow the gap. If, in the subsequent iterate, the element moved to configuration C_2, Gauss point #1 is rebonded. The interface would then have full stiffness. Also, ϵ_1 would be less than zero, with a possible case of nodal penetration when $\epsilon_1 < -1$. The correction for this would be to set $\epsilon_1 = 0$ if $\epsilon_1 < 0$ for a debonded element, i.e. restore the displacement constraint $q_n = 0$. However, this correction requires another iterative cycle, and is not done here.

For the silo problem, it is generally found that debonding takes place at the top corners of material layers during loading. Considerable tensile stresses are generated there. Since final compressive stresses at the top corners are relatively small, the error in rebonding is considered inconsequential to the final results.

Table 4.1 Model description of interface states

State	Constitutive Matrix
Stick ($\tau_{12} < \sigma_1 \tan\phi'$)	$[C]_{stick} = \begin{bmatrix} E_1 & 0 & 0 & 0 \\ 0 & 0 & 0 & 0 \\ 0 & 0 & 0 & 0 \\ 0 & 0 & 0 & G_{12} \end{bmatrix}$
Slip ($\tau_{12} \geq \sigma_1 \tan\phi'$)	$[C]_{slip} = \begin{bmatrix} E & 0 & 0 & 0 \\ 0 & 0 & 0 & 0 \\ 0 & 0 & 0 & 0 \\ 0 & 0 & 0 & 0 \end{bmatrix}$
Debond ($\sigma_1 \geq 0$ or $\epsilon_1 \geq 0$)	$[C]_{debond} = \begin{bmatrix} 0 & 0 & 0 & 0 \\ 0 & 0 & 0 & 0 \\ 0 & 0 & 0 & 0 \\ 0 & 0 & 0 & 0 \end{bmatrix}$

Table 4.2 Interface decision matrix

From \ To	Stick	Slip	Debond
Stick	$q_n = q_t = 0$ $[C] = [C]_{stick}$ No Force Constraints	$q_n = 0$ $[C] = [C]_{slip}$ $\tau_{12} = \sigma_1 \tan \phi'$	No Displacement Constraints $[C] = [C]_{debond}$ $\sigma_1 = \tau_{12} = 0$
Slip	Not Allowed Within a Load Step	$q_n = 0$ $[C] = [C]_{slip}$ $\tau_{12} = \sigma_1 \tan \phi'$	No Displacement Constraints $[C] = [C]_{debond}$ $\sigma_1 = \tau_{12} = 0$
Debond	$q_n = q_t = 0$ $[C] = [C]_{stick}$ $\sigma_1 = \tau_{12} = 0$	Not Allowed	No Displacement Constraints $[C] = [C]_{debond}$ $\sigma_1 = \tau_{12} = 0$

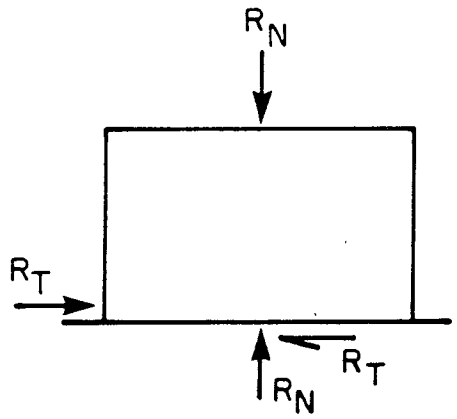

(a) Stick : $R_T < R_N \tan\phi'$

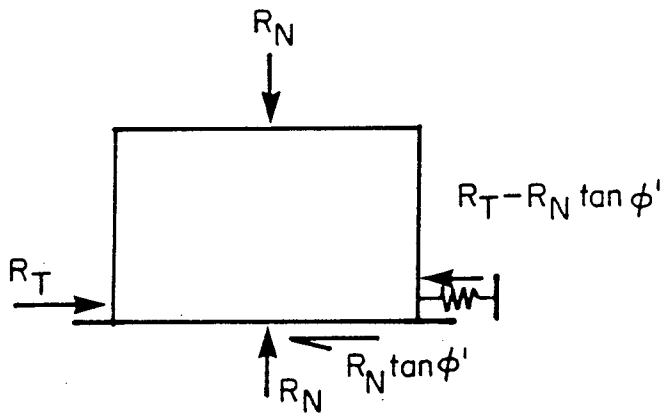

(b) Slip : $R_T \geq R_N \tan\phi'$

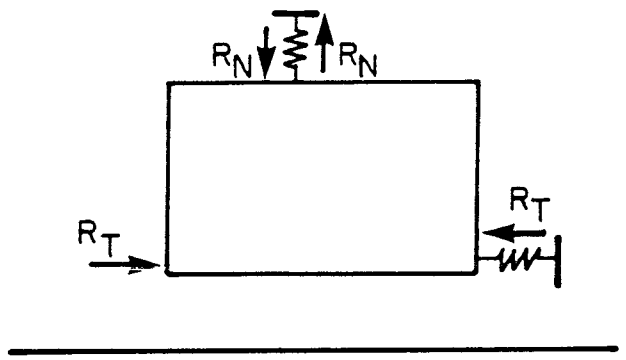

(c) Debond : $R_N \geq 0$

Figure 4.1 Interface states

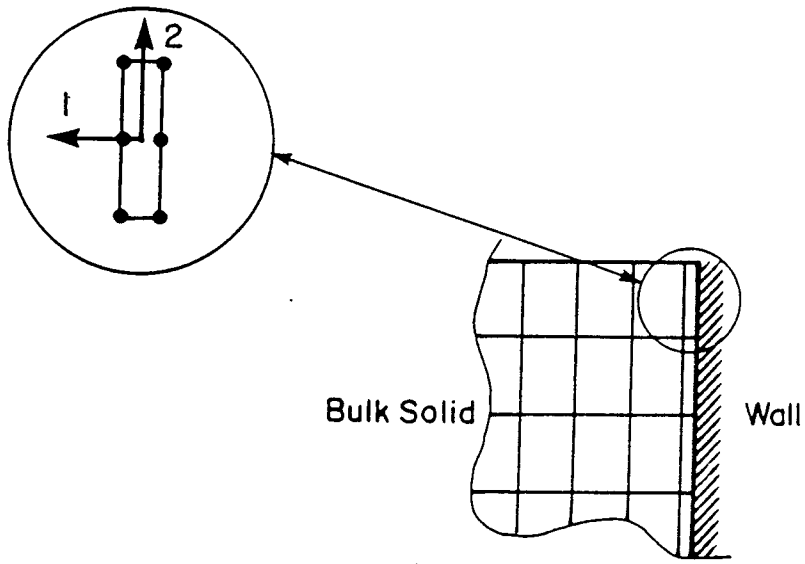

Figure 4.2 Interface element

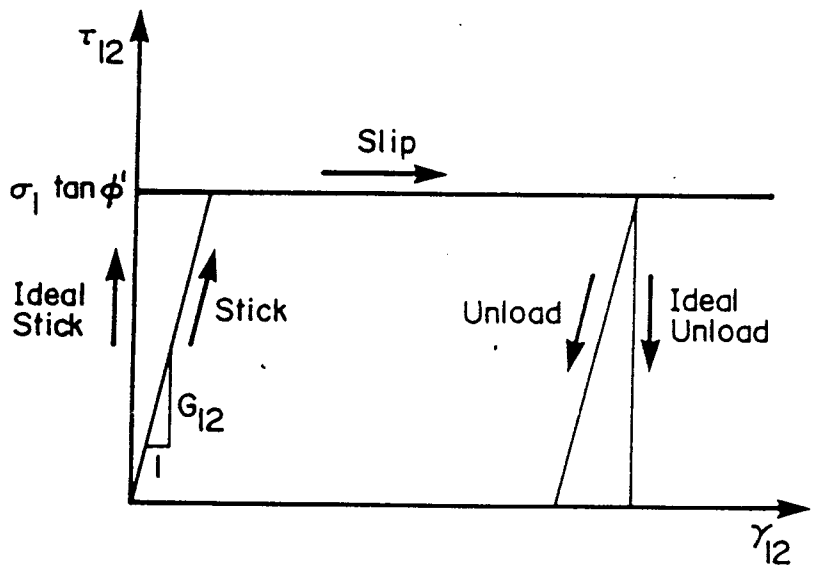

Figure 4.3 Interface shear stress characteristics

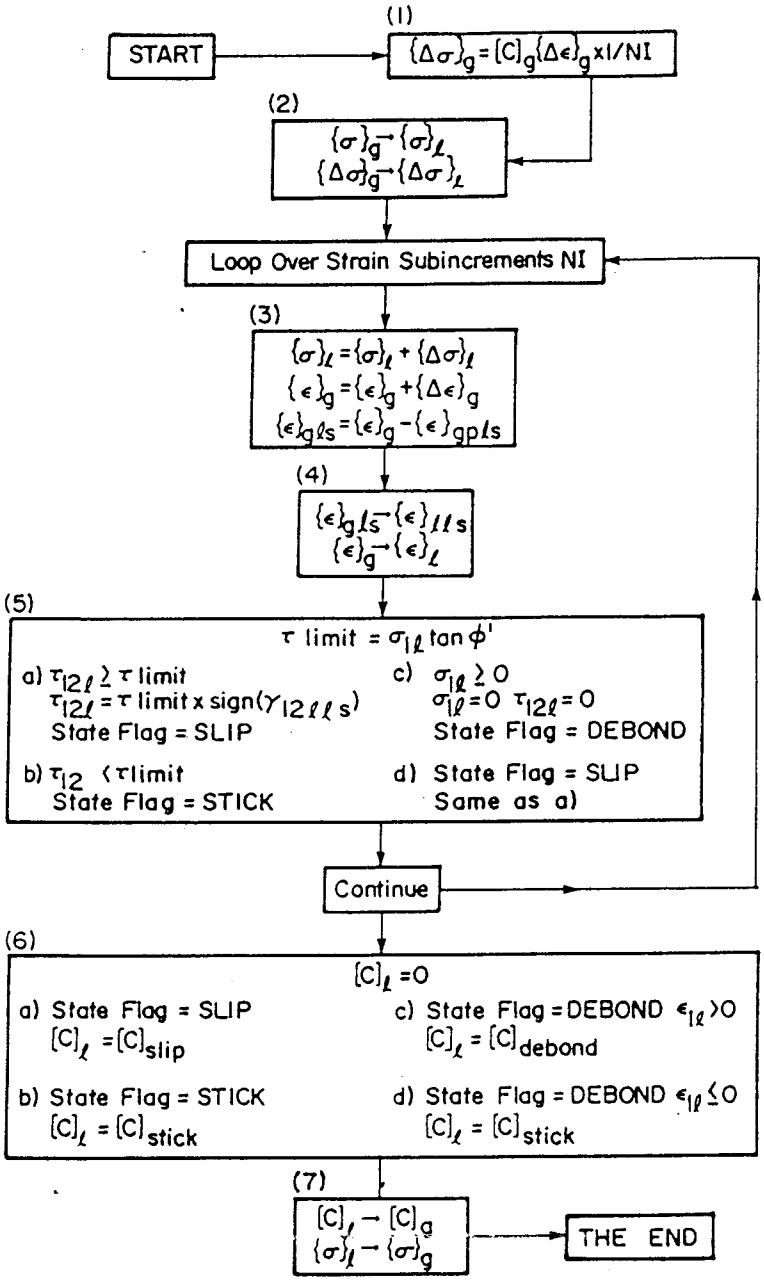

Figure 4.4 Calculation of interface stresses and state - flowchart

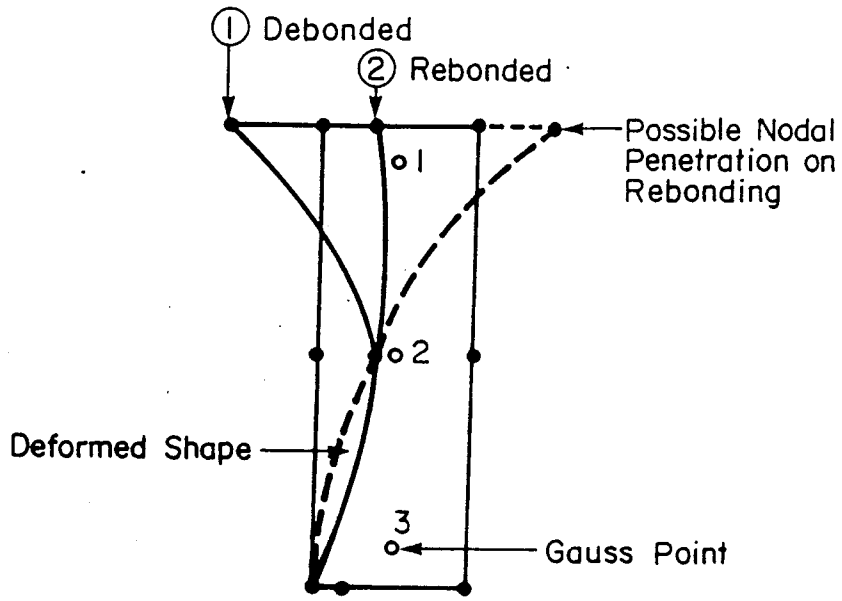

Figure 4.5 Rebonding and nodal penetration

5. MATERIAL MODEL

5.1 Introduction

Ensiled materials are mostly granular in nature, with or without a certain amount of cohesion. Only cohesionless materials are examined in this study. Granular materials have certain behavioral characteristics under loading. These characteristics are summarized as:

1) An increase in density with increased mean stress σ_m.
2) A plastic volume decrease with increasing σ_m.
3) In the elastic range, an increase in elastic modulus E with increasing σ_m.
4) Elastic - plastic work hardening behavior.
5) Time dependent load - deformation behavior.
6) An increase in shear strength with increasing σ_m.
7) A plastic volume expansion when the shear strength of the material is reached and plastic flow commences.

The first three characteristics are consequences of compressibility. Compressibility of granular materials under load is due to deformation of the grains (usually negligible), compression of air in the voids which exist between the grains, and squeezing out of air and water from the voids. For most granular materials, compressibility is not a time dependent phenomenon because granular materials are usually highly permeable, which helps for water and air

to squeeze out of the bulk mass relatively quickly.

Jenike (1964) has found that the material unit weight γ can be expressed in terms of the mean stress σ_m by the expression

$$\gamma = \gamma_0(1 + \sigma_m)^n. \qquad [5.1]$$

where γ_0 is the unit weight intercept and n is a compressibility parameter.

For most materials, $n < 0.1$, and the effect of compressibility on unit weight is negligible. General practice, in most design situations, assumes a maximum expected unit weight value for γ. Although this assumption is conservative, it is the approach followed herein. However, significant error may be introduced in the analysis for highly compressible materials or a small head of material (Smith and Simmonds 1983).

As a bulk mass compresses, progressive stiffening of the material system occurs (Lade 1977). Lade relates the average elastic modulus, E, to the confining stress in a triaxial test, σ_3, as

$$E = K_m p_a \left[\frac{\sigma_3}{p_a}\right]^t. \qquad [5.2]$$

where K_m is a modulus number parameter, p_a is the atmospheric pressure, and t is an exponent parameter.

The values of K_m and t are determined from triaxial compression tests under various levels of the confining stress σ_3. However, these parameters are not available in

the literature for ensiled materials. Therefore, a constant value of E is used herein for the purpose of analysis.

Figure 5.1 shows the variation of volumetric strain ϵ_v with axial strain in a triaxial compression test ϵ_1. The strain increment tensors are composed of three distinct parts; elastic, plastic contractive, and plastic expansive components. In most cases, the effects of compressibility are negligible, and consequently the magnitude of the plastic contractive strain is small. Therefore, in this study only elastic and plastic expansive components of stress and strain are considered.

Granular materials exhibit triaxial stress - strain characteristics similar to those shown in Fig. 5.2. There is a linear initial portion followed by a curved work hardening region. Unloading is generally elastic with a small hysteretic loop. Since, in most cases, the parameters needed to describe the hardening process are not available, it is proposed to use an elastic - perfectly plastic approximation, neglecting both work hardening and hysteresis.

Time dependent load deformation behavior (viscoplasticity) is not considered here. There is very little information regarding the flow properties of bulk solids which can be used in a finite element analysis. Viscoplastic formulations await future research, although some attempts have been made (Eibl and Häussler 1984) to solve the problem.

To summarize the above discussion; if the effects of compressibility are small, then density changes, plastic volume contraction, and changes in bulk modulus are all negligble. The stress - strain relation is approximated by an elastic - perfectly plastic approach, while time dependent behavior awaits further research. Finally, plastic volume expansion and shear strength dependence on the mean stress level have a major influence on material behavior, and are discussed in the next section.

5.2 Model Description

It is desired to model the ensiled material as an elastic perfectly plastic material which exhibits an increase in shear strength with increasing mean stress σ_m. In addition, once the material shear strength is reached, a plastic volume expansion, known as dilatency, occurs. An approach used extensively by geotechnical engineers to model these characteristics is to adopt a Drucker-Prager failure criterion (Drucker and Prager 1952). A more accurate approach may use the failure surface proposed by Lade (1977) or an adaptation of that proposed by Willam and Warnke (1977). However, parameters for these surfaces are not readily obtainable. The Drucker-Prager surface is simple, requiring only two commonly obtained parameters to describe it, and is discussed in subsequent sections.

The theory of perfect plasticity is based on three assumptions (Chen 1982):

1. Existence of a yield surface - The material is elastic until a certain function of the stress components reaches a certain value. This function is known as the yield function, and for perfect plasticity the value of the function is zero i.e.

$$f(\sigma_{ij}) = 0. \qquad [5.3]$$

If $f(\sigma_{ij}) < 0$, the material is elastic. The condition $f(\sigma_{ij}) > 0$ is not allowed for a perfectly plastic material.

Once the yield surface has been reached, plastic deformation takes place without limit. This means that the state of stress must remain on the yield surface i.e.

$$df = \frac{\partial f}{\partial \sigma_{ij}} d\sigma_{ij} = 0. \qquad [5.4]$$

2. The strain increment tensor $d\epsilon_{ij}$ can be decomposed into a recoverable, or elastic, component and a non recoverable, or plastic, component such that

$$d\epsilon_{ij} = d\epsilon^{e}_{ij} + d\epsilon^{p}_{ij}. \qquad [5.5]$$

The stress increment tensor is related to the elastic strain increment tensor by Hooke's Law

$$d\sigma_{ij} = C_{ijkl} d\epsilon^{e}_{kl}. \qquad [5.6]$$

3. Existence of plastic potential - It is assumed that there exists a plastic potential function, $g(\sigma_{ij})$, such that

$$d\epsilon^{p}_{ij} = \frac{\partial g}{\partial \sigma_{ij}} d\lambda, \qquad [5.7]$$

where $d\lambda$ is a positive scalar quantity.

If the function $g(\sigma_{ij})$ defines a plastic potential surface, the surface gradient $\partial g/\partial \sigma_{ij}$ defines the direction that the plastic strain increment must follow.

If Eqs. 5.5 to 5.7 are used in conjunction with the assumptions of perfect plasticity (Eq. 5.4), a constitutive law relating the stress increment tensor to the strain increment tensor is obtained (Chen 1982)

$$d\sigma_{ij} = \left[C_{ijkl} - \frac{C_{ijmn}\, \partial f/\partial \sigma_{mn}\, \partial g/\partial \sigma_{pq}\, C_{pqkl}}{\partial f/\partial \sigma_{rs}\, C_{rstu}\, \partial g/\partial \sigma_{tu}} \right] d\epsilon_{kl}, \qquad [5.8]$$

or, in matrix form

$$\{\Delta\sigma\} = \left[[C] - \frac{[C]\ \{\partial f/\partial \sigma\}\ \langle \partial g/\partial \sigma \rangle\ [C]}{\langle \partial f/\partial \sigma \rangle\ [C]\ \{\partial g/\partial \sigma\}} \right] \{\Delta\epsilon\}. \qquad [5.9]$$

With two different functions $f(\sigma_{ij})$ and $g(\sigma_{ij})$, the elastic plastic constitutive matrix of Eq. 5.9 is unsymmetric, and the flow rule of Eq. 5.6 is called a non associated flow rule. If $g(\sigma_{ij})$ is assumed to have the form of $f(\sigma_{ij})$, an associated flow rule is established, and the constitutive matrix is symmetric.

There is evidence related to dilatency to suggest that cohesionless material behavior should be described with a

non associated flow rule (Lade 1977). However, the associated flow rule has found widespread use because of its simplicity, and is adopted here for the same reason.

5.2.1 Drucker-Prager Surface

The Drucker-Prager surface is a right circular cone with its axes equally inclined to the coordinate axes in principal stress space, as shown in Fig. 5.3. The yield function is expressed as

$$f(I_1,\sqrt{J_2}) = \alpha I_1 + \sqrt{J_2} - k = 0, \qquad [5.10]$$

where α and k are real material constants. The terms I_1 and J_2 are the first stress invarient and second deviatoric stress invarient respectively. These invarients can be expressed in terms of the mean shear stress τ_m and the mean normal stress σ_m as

$$I_1 = 3\sigma_m, \qquad [5.11]$$

$$J_2 = 5/2\tau_m^2, \qquad [5.12]$$

where σ_m is the average of the three principal stresses and τ_m is given as

$$\tau_m = \sqrt{S_{ij}S_{ij}/5}. \qquad [5.13]$$

The deviatoric stress tensor S_{ij} is expressed as

$$S_{ij} = \sigma_{ij} - \sigma_{kk}\delta_{ij}/3. \qquad [5.14]$$

If Eqs. 5.11 and 5.12 are substituted into Eq. 5.10 and the expression is normalized with respect to uniaxial compressive strength, f_{cu}, an expression is obtained relating the yield function to mean stress components (Askari and Elwi 1986)

$$\frac{f(\sigma_{ij})}{f_{cu}} = \frac{\tau_m}{f_{cu}} + \sqrt{\frac{18}{5}}\,\alpha\,\frac{\sigma_m}{f_{cu}} - \sqrt{\frac{2}{5}}\,k = 0. \qquad [5.15]$$

That form is suited for concrete materials for which the application program FEPARCS was written. In the current context, it is applied with the value $f_{cu} = -1$. The representation of the yield surface in mean stress coordinates is shown in Fig. 5.3c.

It is desirable to relate the Drucker - Prager strength parameters α and k to the Mohr - Coulomb strength parameters ϕ and c. The terms ϕ and c refer to the angle of internal friction of the material and the cohesion intercept respectively. For axisymmetry and plane strain, the relationships are given as (Chen 1982)

$$\alpha = \frac{\tan\phi}{\sqrt{9 + 12\tan^2\phi}}, \qquad [5.16]$$

$$k = \frac{3c}{\sqrt{9 + 12\tan^2\phi}}. \qquad [5.17]$$

The mathematical description of the Drucker - Prager surface is now complete. The yield surface description in Eq. 5.15, with parameters from Eqs. 5.16 and 5.17, can be used in conjunction with Eq. 5.9 to model elastic perfectly

plastic behavior of a granular material.

5.2.2 Computational Algorithm

The numerical implementation of the material model is described in detail in Appendix A. To summarize, an elastic stress increment is calculated, and a trial total stress state is obtained. The total stress state is then checked against yield criterion. If yielded, the stress and strain increments are decomposed into two components; an elastic stress (strain) increment, and a stress (strain) increment after onset of yielding. To obtain this decomposition, the intersection point of the stress increment with the yield surface is computed. Elastic stress increments are calculated using the matrix form of Eq. 5.6

$$\{\Delta\sigma\} = [C]\{\Delta\epsilon\} \qquad [5.18]$$

Stress increments after onset of yielding $\{\Delta\sigma\}_{oy}$ are obtained using Eq. 5.9 and $\{\Delta\epsilon\} = \{\Delta\epsilon\}_{oy}$. Finally, the error in the incremental approach is scaled to an acceptable tolerance, and the total stress state lies near the yield surface. If the stress increment is small, the assumption of a linear stress increment is a good approximation. Using a linear stress increment with the point of intersection at $\sigma_m = 0$ presents difficulties because the surface gradient $<\partial f/\partial\sigma>$ is not uniquely defined. It is proposed here to use a stepwise stress path to move away from $\sigma_m = 0$ to a point on the yield surface where the surface gradient is uniquely

defined. In this process, the test stress increment $\{\Delta\sigma\}_{test}$ is divided into a mean, $\{\Delta\sigma\}_m$, and a deviatoric component $\{\Delta\sigma\}_d$

$$\{\Delta\sigma\}_{test} = \{\Delta\sigma\}_m + \{\Delta\sigma\}_d. \qquad [5.19]$$

The stepwise stress path is used for all increments of mean stress $\Delta\sigma_m < 0$. The stress increment $\{\Delta\sigma\}_{test}$ is applied in two steps. First, $\{\Delta\sigma\}_m$ is applied which does not lead to yield if $\{\Delta\sigma\}_m < 0$

$$\{\sigma\} = \{\sigma\}_0 + \{\Delta\sigma\}_m. \qquad [5.20]$$

Then, the deviatoric component is added

$$\{\sigma\}_{test} = \{\sigma\} + \{\Delta\sigma\}_d. \qquad [5.21]$$

The rationale for using the stepwise stress path for all mean stress increments less than zero can be seen by examination of Fig. 5.4. If a linear stress path is followed, the point of intersection with the yield surface is at point a. If a stepwise stress path is used, the intersection is at point b. The actual stress state is close to point c. It can be seen that point b is closer to the actual stress state than point a. This means that yield surface drift is reduced because point b has a better estimate of the surface gradient than point a.

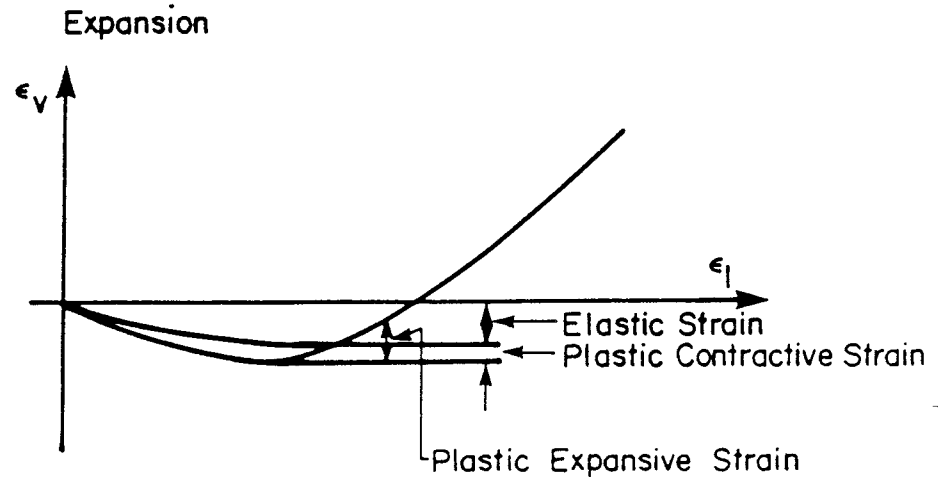

Figure 5.1 Volumetric strain characteristics

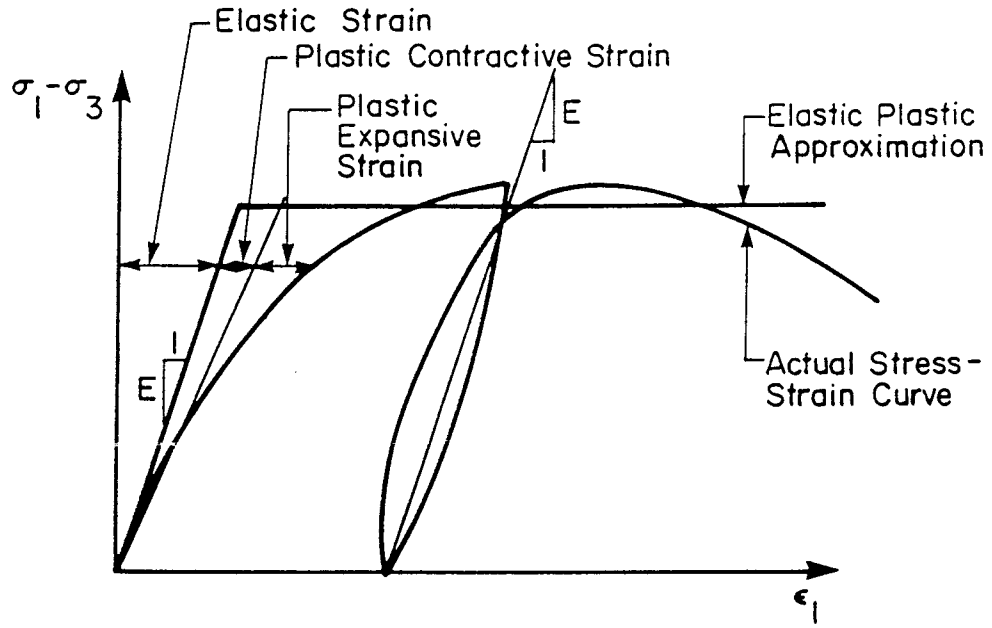

Figure 5.2 Bulk solid stress-strain characteristics

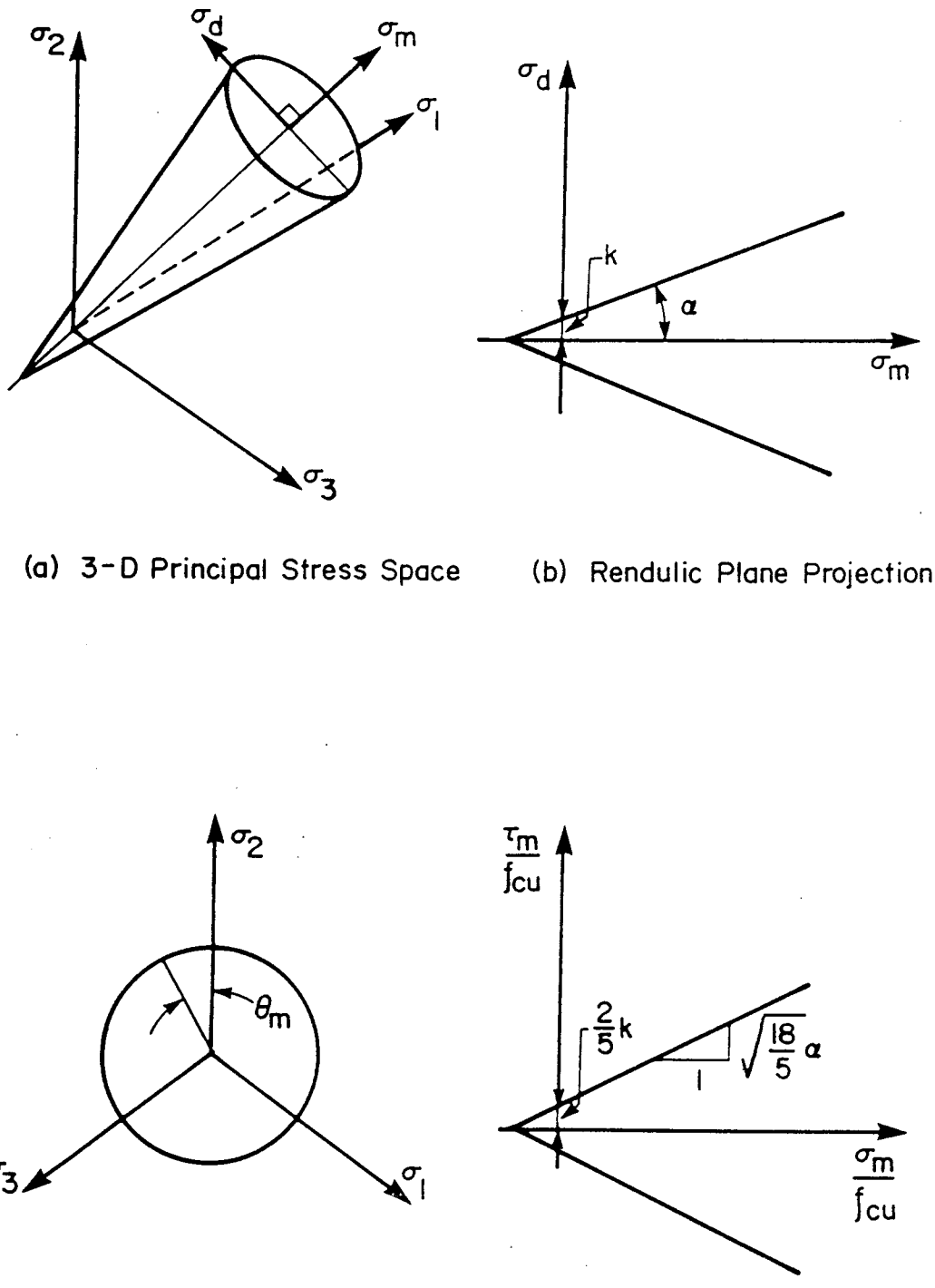

(a) 3-D Principal Stress Space (b) Rendulic Plane Projection

(c) Octahedral Plane Cross Section (d) Mean Stress Coordinates

Figure 5.3 Drucker-Prager yield surface

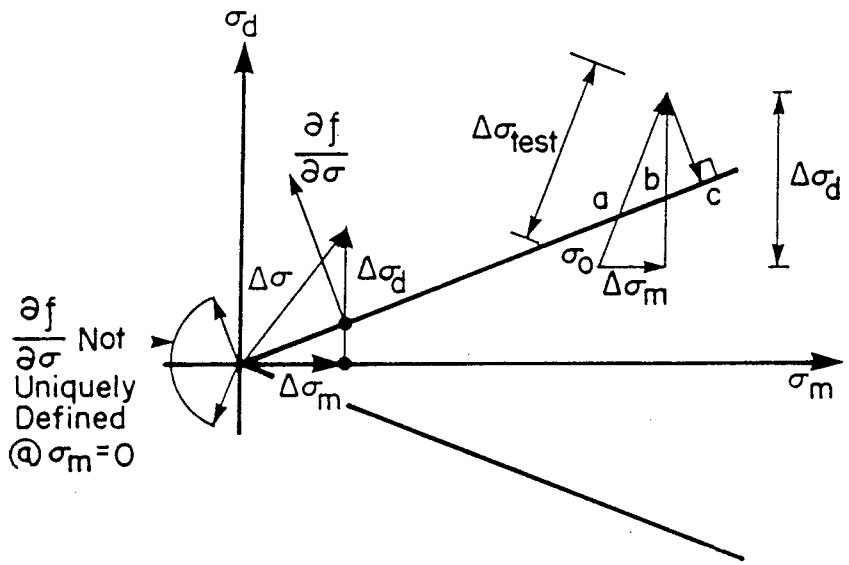

Figure 5.4 Stepwise stress path on a rendulic view

6. IMPLEMENTATION LEADING TO INCIPIENT FLOW

6.1 Introduction

In chapters three, four, and five, finite element models were presented for wall interface and material behavior. These models are now used along with special provisions for loading history to determine wall pressures. In this chapter, one axisymmetric silo geometry with three sets of material properties is analysed using a modified version of the program FEPARCS (Elwi and Murray 1980).

In the first phase of the analysis, a typical silo is filled in stages, and comparisons with the Jenike and Janssen pressure distributions are made. In the second phase, the silo outlet closure is removed in an incremental manner, and the resulting stress field is examined. Finally, failure to obtain a free flowing solution is examined, and recommendations for design are made.

6.2 Procedure for Filling and Release

To obtain correct wall pressures, it is necessary to know the load history of the silo. This is because the constitutive behavior of both the ensiled material and wall interface are path dependent. The load history of a silo consists of two parts; filling and release.

Filling usually takes place continuously, but it is sufficiently accurate to model the filling process as a sequence of material layers. The material layers are placed

in a series of load steps until the silo is filled. Analysis in steps normally yields better results than "single step switch on" gravity methods (Clough and Duncan 1969).

A simple method of stepwise filling is implemented in program FEPARCS. Each material and interface element is given a layer activation number. The number corresponds to the layer the element belongs to. When a layer activation number is specified in a load step, all elements that have an activation number less than or equal to the specified value are activated. In other words, stiffnesses and gravity loads are calculated for these elements. Elements that are not activated are assigned small elastic moduli, and their gravity loads are not calculated.

In practice, when the ensiled material is required, the outlet bottom is released, and the material flows freely or flow is controlled by a feeder. For the purpose of analysis, it is desirable to control the release procedure in order to closely monitor material yielding. Full release is difficult in a static analysis, since the material near the bottom of the silo fails, causing numerical instability. Therefore, the analysis is limited to incipient flow.

The boundary conditions of a closed outlet bottom can be modelled by a series of stiff springs, as shown in Fig. 6.1a. To control the release process, it is possible to replace the springs with a series of equivalent nodal forces (Fig. 6.1b). These forces can be incrementally removed from the outlet until the material starts flowing. Flow is

detected by a sudden increase in displacements at the outlet, followed by convergence failure of the numerical procedure.

6.3 Description of Silo Model

As described earlier, one axisymmetric silo geometry under three different sets of interface and material properties is analysed. These analyses are referred to, hereinafter as Silo #1, Silo #2, and Silo #3. The finite element discretization of the silo geometry is shown in Fig. 6.2. Because of symmetry, only one half of the total cross-section is considered. To eliminate the effects of wall flexibility on wall pressures, the nodes at the silo wall are prevented from moving. The bulk material region is characterized by eight node isoparametric elements. The midside nodes along the top and bottom of the interface elements have been eliminated because inclusion of these nodes may cause zero stiffness terms to appear on the main diagonal of the stiffness matrix during slip. Thus, isoparametric elements with six nodes are used to describe the interface.

The outlet closure during filling is represented by a series of stiff springs as shown in Fig 6.1a. The springs are removed and replaced by a series of equivalent nodal forces for release conditions as described in the previous section.

Silo #1 has an internal angle of friction ϕ of 35°, and a wall friction angle ϕ' of 20°. Silo #2 has ϕ and ϕ' angles of 25° and 15° respectively, and Silo #3 has values of ϕ and ϕ' of 15° and 10° respectively. The unit weight of the material is identical for all three silos, and is similar to that of finely graded coal at 9.5 kN/m^3. An average modulus of elasticity E of 1.5×10^5 kPa is used. It was observed in preliminary analyses with a hopper configuration, that a substantial variation in E caused only a minor variation in stresses.

As described in Chapter 4, values of E_1 and G_{12} for the interface elements are determined by varying these parameters until the stress oscillations near the transition area are small or have disappeared. Generally, values for E_1 and G_{12} of 1.0×10^4 kPa and 1.0×10^6 kPa respectively were found suitable, although some oscillations of pressure results were still present.

6.4 Discussion of Results

6.4.1 Initial Filling

Figures 6.3, 6.4, and 6.5 show the wall pressure results for initial filling of Silos #1, #2, and #3 respectively. These are plotted as wall pressure vs. height above the silo outlet. For the purpose of comparison, two other curves are plotted. These curves are the prediction of wall pressures using Janssen's theory for the cylinder and

Jenike's initial pressure theory for the hopper region (Jenike et. al. 1973). The first curve is obtained using a lateral pressure coefficient, K, of 0.4. This is the value recommended by Jenike et. al. (1973) based on experience and test results. The second curve is derived using an "at rest" value of K recommended by Jaky (1948). The "at rest" coefficient, K_0 has been determined experimentally as

$$K_0 = 1 - \sin \delta, \qquad [6.1]$$

An examination of Figs. 6.3 to 6.5 shows that the variation in wall pressures follow a similar pattern. In the cylinder region, the wall pressures closely approximate a Janssen distribution. The plot using $K = K_0$ gives a closer estimate of finite element wall pressures than does the plot using $K = 0.4$ in each case. In the hopper region, the finite element results are close to the Jenike pressures in most areas, and are slightly less than the Jenike pressures near the outlet of Silos #1 and #2. As for the cylinder region, the plot using $K = K_0$ provides a closer fit of the finite element data than the plot using $K = 0.4$.

Oscillations and a large overpressure are evident near the transition region for all three silo cases. Some of the overpressure may be due to the existence of a stress concentration at the sharp corner of the transition. More likely, the oscillations and overpressure may be due to the numerical instability discussed earlier in Chapter 4. However, the oscillations and overpressure only occur near

the transition, and their effects tend to be localized.

Figures 6.6 to 6.8 show the direction and magnitude of principal stresses for Silos #1 to #3 respectively. In an active state of stress, the major principal stresses are aligned in more or less the vertical direction. Examination of the principal stress directions confirms that the stress field closely approximates an active field, which is consistent with both the Janssen and Jenike theories.

Figures 6.9 to 6.11 show the nodal displacements of the bulk material in the silos. Since the silo wall is very stiff, the displacements of the ensiled mass are mostly in the vertical direction. The ensiled material in the cylinder deforms rigidly, with most of the deformation occuring in the weak material at the silo wall. Examination of Figs. 6.12, 6.13, and 6.14, which show the location of plastic Gauss points in all three silos, indicates that the bulk material in the cylinder is not rigid plastic as assumed by Janssen (A plastic Gauss point is a material sampling point which has yielded according to the yield criteria discussed in Chapter 5.) Thus, the assumption of a rigid moving system seems valid, and the use of K_0, an experimental parameter, sidesteps the assumption of a fully plastic active field.

In Jenike's derivation of inital filling pressures in hoppers, it was assumed that the hopper stress field was elastic active. Examination of Figs. 6.12 to 6.14 tends to confirm this assumption.

From the above discussion, it is evident that the finite element analysis closely represents the stress fields proposed by Jenike and Janssen during filling. The finite element analysis, therefore, gives a good estimate of an initial stress field with which to study conditions of incipient flow.

6.4.2 Incipient Flow

Plots of wall pressure vs. height above outlet are shown in Figs. 6.15 to 6.17 for Silos #1 to #3 respectively. The quantity U represents the cumulative proportion of equivalent nodal force removed from the outlet; eg. if U = -0.5, half of the static outlet load is removed. The largest value of U is the point at which the problem fails to converge. As described earlier, convergence failure was characterized by a sudden large increase in displacements at the outlet, indicating localized material failure.

As the release process was initiated, all three silos experienced a sudden, localized overpressure near the outlet. This overpressure continued to increase until failure for the stronger material in Silo #1. However, as release progressed for the weaker materials in Silos #2 and #3, there was a sharp decrease in pressure at the outlet, and a concommitant pressure increase in the material above the outlet. In the case of Silo #3, the pressure increase moved upward as release progressed.

Plots of principal stress directions for selected U values are shown in Figs. 6.18 to 6.22. In all cases, it is evident that arching occurs in the hopper region.

Figures 6.23 to 6.27 show the yield status of the material Gauss points in the silos during selected stages of outlet release. All silos show localized plastification regions near the silo outlet.

The yielding history of Silo #3 is examined in the following, since this silo gives the best indication of material flow.

Yielding at the outlet began at U = -0.70. The plastic arch extended to a height of 1 metre, with elastic arching occuring from 1 to 2 metres (See Fig. 6.20). The upper boundary of yielding coincided with the increase in wall pressure (See Fig. 6.17). At U = -0.8, yielding progressed to the 2.5 metre level, with elastic arching extending to 4 metres, and the upper yield boundary roughly coincided with the increase in wall pressure. At U = -0.9, the level of yielding had progressed to 4 metres, and the elastic arch moved to 5.5 metres. The upward motion of the upper yield boundary was consistent with the behavior of the previous two load steps.

Figures 6.29 and 6.30 show the variation of horizontal and vertical stresses with load history at two selected Gauss integration points (shown in Fig. 6.28). Load steps #1 to #12 represent the 12 layers of elements used in filling the silo. Load steps #13 to #16 are outlet unloading stages

with U values -0.5, -0.7, -0.8, and -0.9 respectively. As the silo is filled, it is evident from both figures that the vertical stress, σ_v, is larger than the horizontal stress, σ_h, indicating an active stress field. Both stresses increase with increasing consolidating pressure (layers). As outlet unloading progresses, σ_v decreases and σ_h continues to increase, indicating a switch from an active to a passive stress state. Finally, after both points have plastified, at load step #15, both stresses decrease until failure.

Variation in K^* vs. load history is plotted in Fig. 6.31 for the selected Gauss points. The parameter K^* refers to the ratio of minor principal stress to major principal stress. Bounds for the active (K_0) and passive (K_p^*) are also plotted for reference, where, K_0 is as described by Eq. 6.1 and

$$K_p^* = 1/K_p = \frac{1 - \sin \delta}{1 + \sin \delta}. \qquad [6.2]$$

Initially there is a sharp variation in K^*. As the load steps continue, K^* for both points assumes a fairly constant value close to K_0. During load steps #13 and #14, when the release process starts, the stresses switch direction, causing an increase in K^*. At load steps #15 and #16, the points yield and closely approach K_p^*.

Based on the above discussion, a model of incipient flow can now be described. As outlet unloading progresses, the material at the outlet forms a stable arch until the material shear strength is reached. A loss of equilibrium at

the outlet is balanced by an overpressure which exists in the elastic arch. Once the material shear strength is reached, subsequent unloading of the outlet (release of outlet pressures) causes a reduction in the mean stresses and hence a decrease in the material shear strength. Consequently, a reduction in wall pressures ensues. This process moves upwards behind the front of elastic arching.

The effects of outlet pressure release are shown in Fig. 6.32, which shows a projection of the stress state history at a point on the σ_1-σ_2 plane. For simplicity, the state of stress is assumed to be on the axis of symmetry. Point "1" represents the state of stress during filling. If the outlet is slowly opened, increments $\Delta\sigma_1$ are tensile. As increments $\Delta\sigma_1$ are removed, the material is drawn downward, causing compression in the horizontal direction because of the converging geometry of the hopper. The reduction in σ_1 and increase in σ_2 imply a switch in pressure fields. Once the yield surface is reached, further increase in σ_2 is not possible, since the state of stress must follow the yield surface and σ_1 must continue to reduce. Therefore, the material strength decreases, and wall pressures reduce.

The upward propagation of the arching action is caused by the decrease in vertical stresses of the underlying material. The material above the outlet progressively arches and yields, causing subsequent overpressures and pressure reductions respectively. This arching may or may not arrest at the transition. The behavior described above matches

closely the process hypothesized by Jenike (1964). Further insight can be achieved by the use of a simple illustration. Consider the hopper configuration shown in Fig. 6.33. Initially, the system is in equilibrium. If the outlet is unloaded to the point just before material yield (Fig. 6.33b), there is a net loss in equilibrium which must be balanced by the hopper walls. The overpressure force, N, is carried mostly in the elastic arch. Let the outlet be further unloaded so that the material yields (Fig. 6.33c) The yielded material loses strength, and stresses are reduced in the solid as described earlier. In order to maintain vertical equilibrium, the walls above the yielded material must carry the difference in initial outlet stress, $\Delta\sigma_0$, and the difference in wall initial and flow forces. According to Jenike et. al. (1973), a concentrated load acting over a distribution depth of 0.3B provides the equilibrium imbalance (shown in Fig. 6.33c). According to Walker (1966), a sharp pressure increase at the switch and pressure decrease below the switch are equilibrium consequences of the switch in pressure fields. Walker's approach can be thought of as a "smoothed" approximation, while Jenike's approach implies a sharp stress discontinuity.

Table 6.1 shows a comparison of finite element maximum pressures with pressures calculated using the Jenike and Walker approaches at the outlet region. The wall pressures were calculated using expressions for the switch pressure,

assuming the switch point can occur anywhere in the hopper. The derivation of these expressions is given in Appendix B.

The finite element pressures agree more closely with Walker's results than Jenike's at the outlet region. However, Walker's results were calculated assuming uniformity of vertical stress across the hopper cross-section (D = 1 in Eq. 2.12). Walters (1973) has shown that D is always greater than 1 for flow pressures, and Walker (1966) estimates D as between 1 and 2. Therefore, Walker's switch pressures should be higher than the values given in Table 6.1. If Walter's method of calculating D is used, values of 1.3 to 1.6 are obtained for Silos #1 to #3.

It is evident that maximum outlet pressures obtained in the finite element analysis are lower than both Jenike's and Walker's predicitons. The discrepancy in results may be due to the assumption of a switch point in the analytical studies compared to the softer distribution of the elastic arching in the finite element results. As discussed earlier, elastic arching takes place over a finite height of hopper, thereby reducing the stress intensities at the switch location because the unbalanced load is distributed over the arch height.

Generally, the orientation and propagation of the plastic arched stress field for Silo #3 seems to be in agreement with theories proposed by Jenike and Walker. It was not possible to develop an extensive plastic flow field in Silos #2 and #3. Reasons for this are examined in Section

6.6.

6.5 Design Situations Involving Incipient Flow and "Lock In" Stresses

It has been postulated that the switch pressure, although it exists everywhere in the hopper, is short lived. Therefore, design practices for hoppers tend to ignore all switch loading except that at the transition area. This may be unwise, since switch loads can exist in the form of "lock in" stresses. These stresses occur when flow is interrupted, and the switch overpressure is trapped between the hopper outlet and the transition, and exists as a static load.

Figures 6.34 and 6.35 are plots of wall pressure vs. hopper height obtained by Walker and Blanchard (1967) for 15° pyramidal and conical hoppers respectively. Hopper geometries are shown in Fig. 2.9. The first curve, labelled "normal loading", represents filling by dropping coal from a loading belt. The second curve, labelled "part low pressure", is an attempt to reduce stress buildup at the outlet. The hopper was filled to the one-third level, then 100-200 lbs. (45.5-91.0 kg.) of coal was drawn off the base of the hopper. Filling was then completed. The third curve, labelled "extreme low pressure", was achieved by filling for 30 seconds at a specified filling rate, followed by 30 seconds discharge at a rate lower than filling until the hopper was finally filled. The straight line is a hydrostatic pressure distribution for reference.

It is apparent that there is a pressure decrease at the outlet for "part low pressure" filling. There is a corresponding pressure increase at higher levels in the hopper. The switch appears to be "locked in" at the point of greatest pressure for both hoppers. In the "extreme low pressure" filling, the static loading curve is similar to the flow pressure curve. The conditions described above are similar to the results obtained from Silos #1 to #3 during incipient flow.

Conditions of "lock in" stresses can occur if flow is terminated. Any additional filling of the silo causes the switch pressure to increase. This may cause problems not only with loading, but with arching. If a cohesive material is present in the silo, high overpressures at the switch point may cause a strength increase such that a stable arch is formed. The collapse of this arch may induce additional dynamic loads. This has been observed experimentally by Smith and Simmonds (1983) in the cylinder region of a silo.

It has been suggested by both Jenike et. al. (1973) and Walters (1973) that silos should be designed on the basis of a pressure envelope which bounds all maximum pressures. This seems overly conservative, considering that the switch at any one time is at one location. It seems more rational to investigate the effect of a concentrated load or stress distribution on silo walls in order to determine design parameters.

Based on the limited results obtained by the finite element analysis of Silos #1 to #3, it may be possible to reduce the loads obtained by the theories of Jenike and Walker. However, parametric studies are needed with a more sophisticated model to determine a full envelope of design pressures for hoppers.

6.6 Convergence Failure

As described earlier, convergence was measured as the ability of the solution to achieve specified load and displacement tolerances. Failure occurred if the solution could not meet these tolerances within a specified number of iterates. Convergence failure occurred in Silos #1, #2, and #3 during outlet release U values of -0.98, -0.88, and -0.90 respectively. For each failure, there was evidence of a localized solution instability. At failure, outlet displacements increased substantially over those of previous load steps, whereas other material displacements were relatively unaffected.

In bin loading theories proposed by Jenike (1961), Walker (1966), and Walters (1973), the assumption is made that a plastic passive stress field exists in the hopper. Pressure measurements in hoppers confirm that a pressure reduction takes place during flow (Jenike et. al. 1973, Walker and Blanchard 1967, Moriyama and Jotaki 1980). From the preceeding discussion, this seems to indicate the physical existence of a plastic passive stress field. In

this study, it was not possible to develop an extensive plastic field in the hoppers of Silos #1 and #2.

In an actual hopper, if the outlet is opened, bulk material flows in a state of dynamic equilibrium. Material stresses in excess of yield are balanced by inertial and viscous forces. These forces were not included in the analysis, and hence a net force imbalance at the outlet results which may cause convergence failure before a full plastic field can develop. It may be ultimately necessary to use an Eulerian formulation for which velocities and accelerations are measured relative to a fixed spatial mesh (Eibl and Häussler 1984). Alternatively, a hardening parameter may be introduced into the plasticity approach. The hardening parameter would serve as an artificial means of ensuring solution stability.

It may be possible to extend the solution in a Lagrangian frame of reference by using a displacement constraint strategy in which the outlet nodes are constrained to move vertically once the hopper is vacated. This is analogous to forming a vertical tube around the outlet.

Problems also exist with the choice of yield surface. The yield surface for actual materials is compared with the Drucker-Prager yield surface in Fig. 6.36. The state of stress in the hopper material during yield follows the line $\sigma_1 > \sigma_2 = \sigma_3$ (Jenike 1961). The Drucker-Prager surface gives a conservative estimate of yielding in this region. In

addition, the rate of dilatency for the Drucker-Prager surface in this region is high. Since plastic volume increases are restrained in the hopper, the restraint forces increase the material strength and retard yielding. It may be advisable to adopt a yield surface similar to Lade (1978), where the yield strength of a material is dependent on the mix of stresses (See Fig. 6.36).

Table 6.1 Comparison of maximum outlet pressures with Jenike's and Walker's pressures

SILO		OUTLET PRESSURE (kPa)
1. $\phi' = 20°$	Jenike	248.2
$\delta = 35°$	Walker	119.6
	F.E.	86.6
2. $\phi' = 15°$	Jenike	278.6
$\delta = 25°$	Walker	119.2
	F.E.	88.4
3. $\phi' = 10°$	Jenike	332.4
$\delta = 15°$	Walker	113.8
	F.E.	111.3

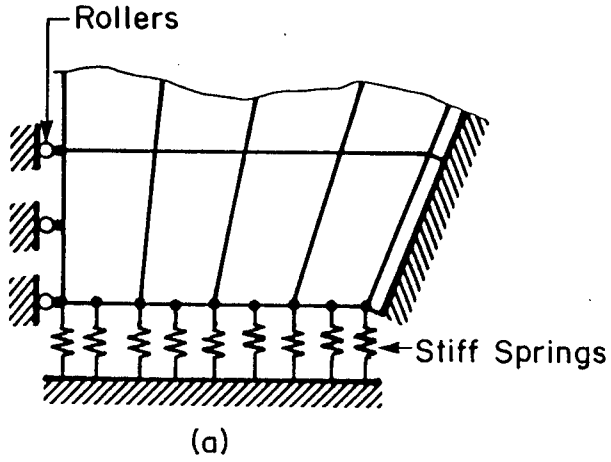

Figure 6.1 Outlet modelling

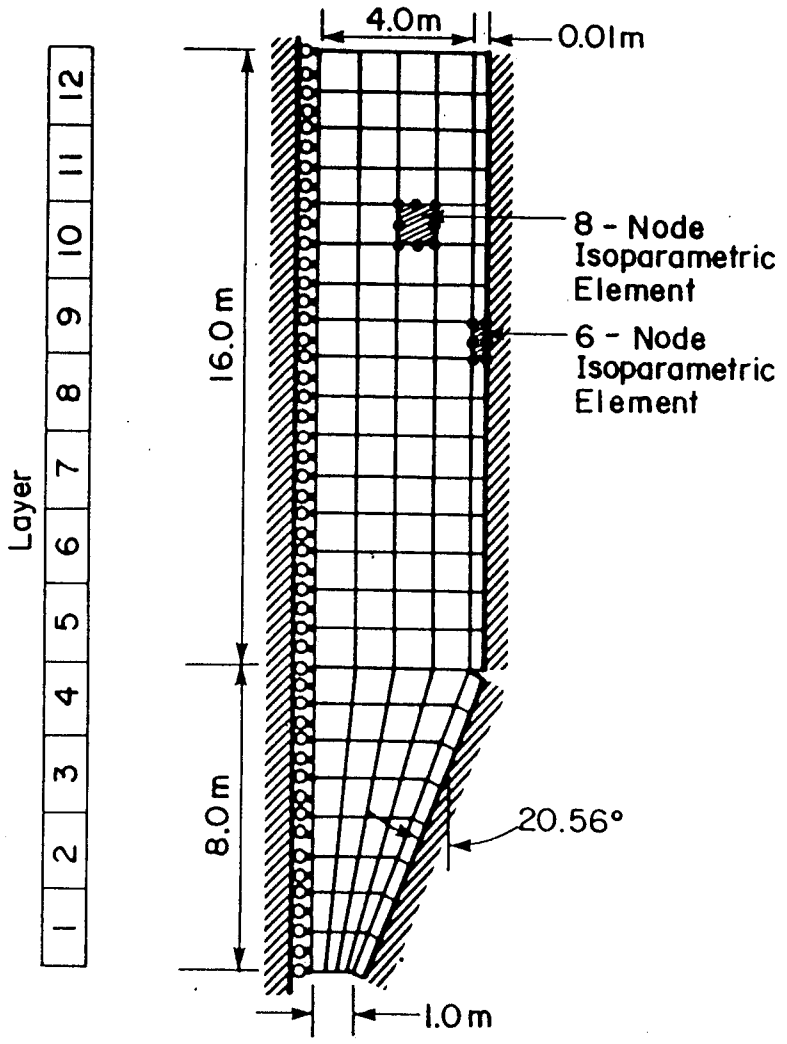

Figure 6.2 Finite element mesh

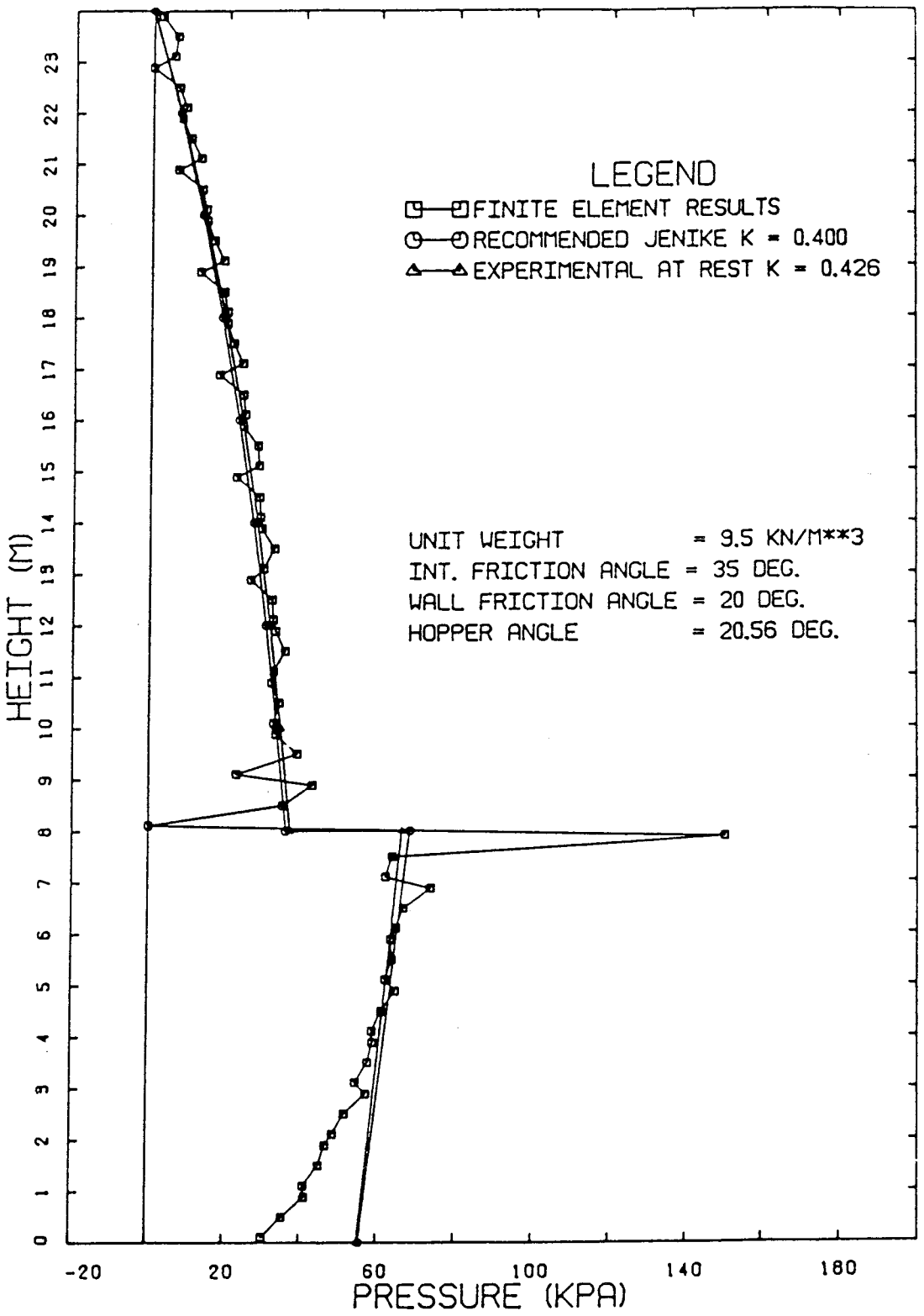

Figure 6.3 Initial filling wall pressures - Silo #1

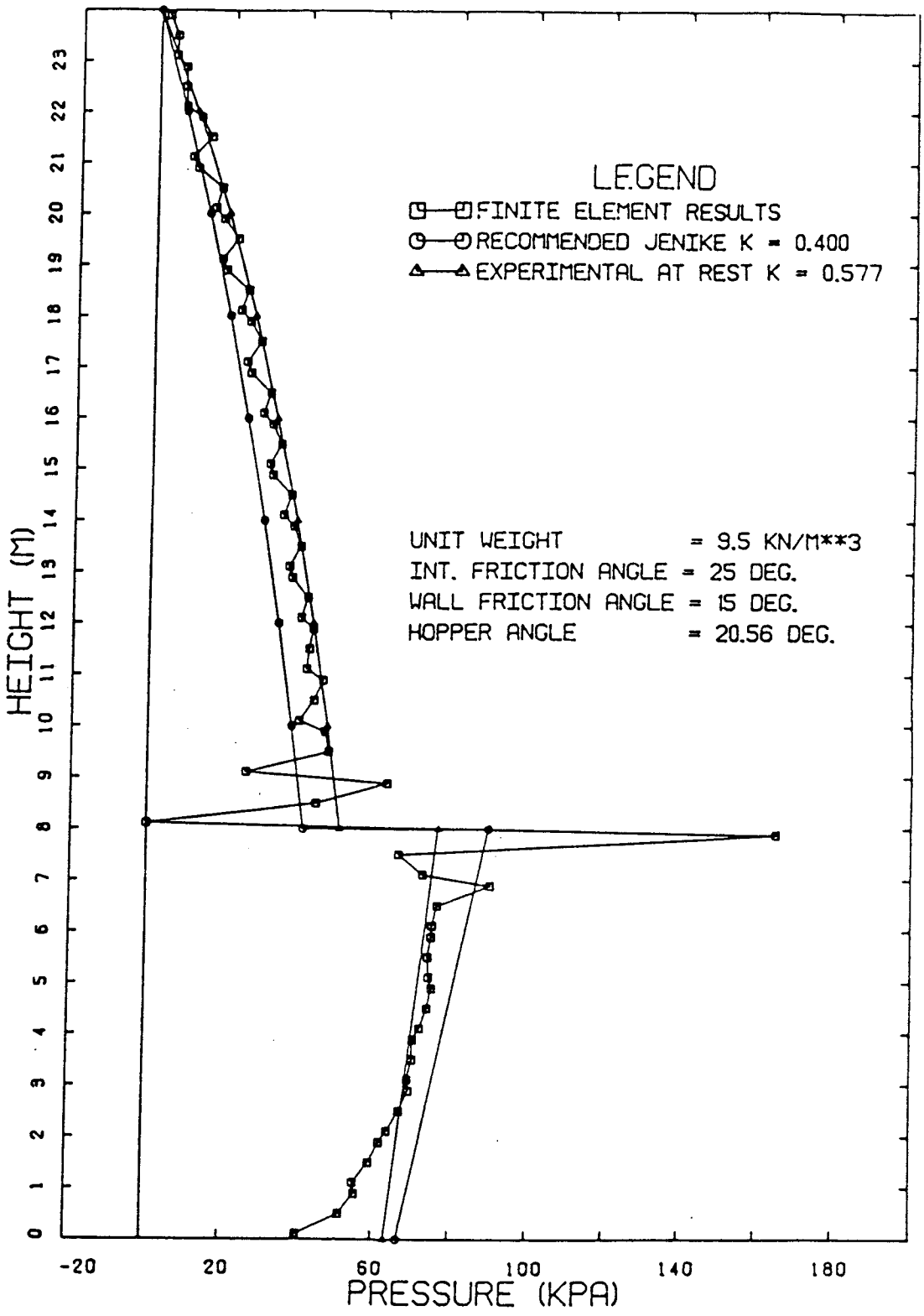

Figure 6.4 Initial filling wall pressures - Silo #2

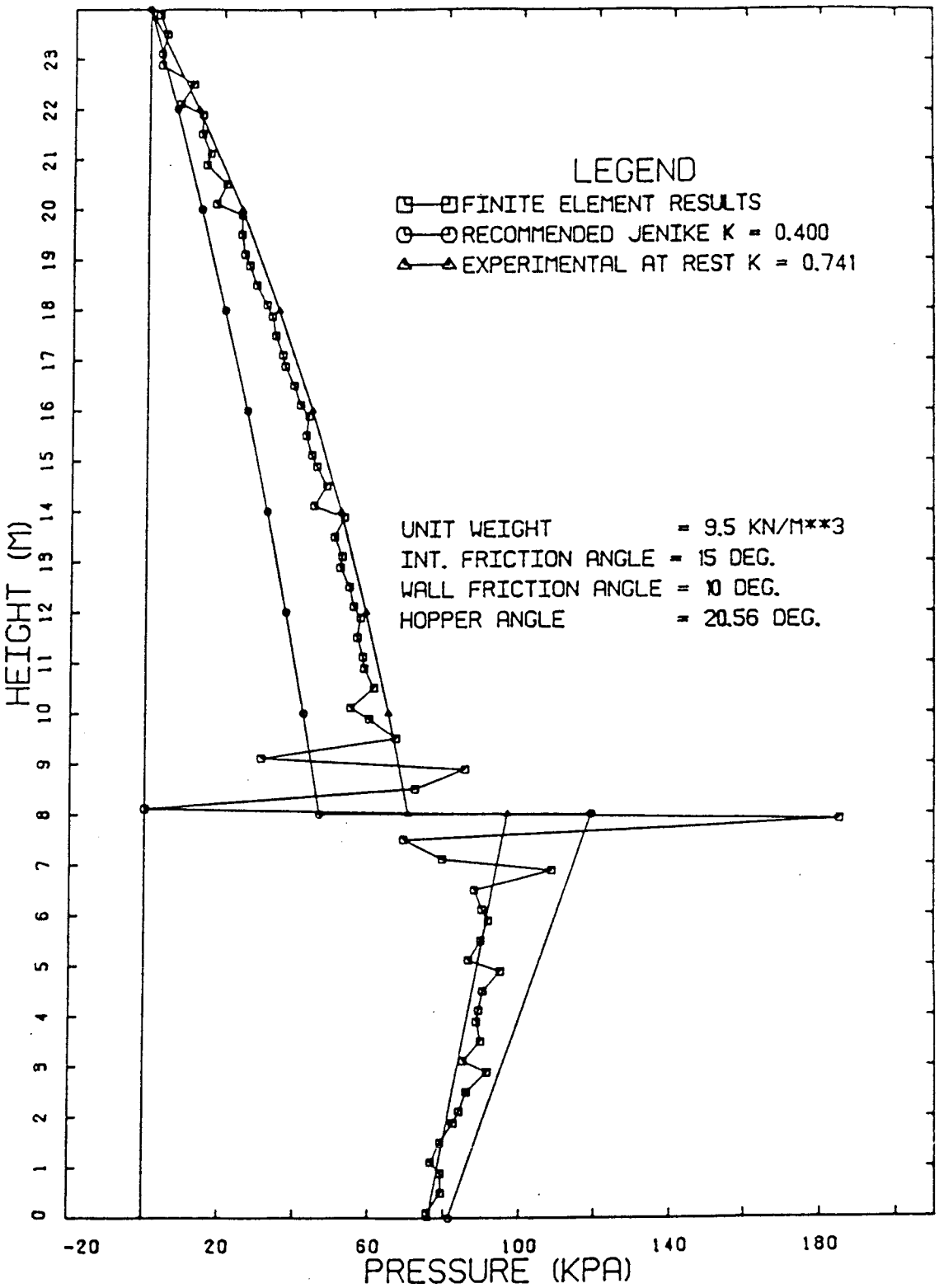

Figure 6.5 Initial filling wall pressures - Silo #3

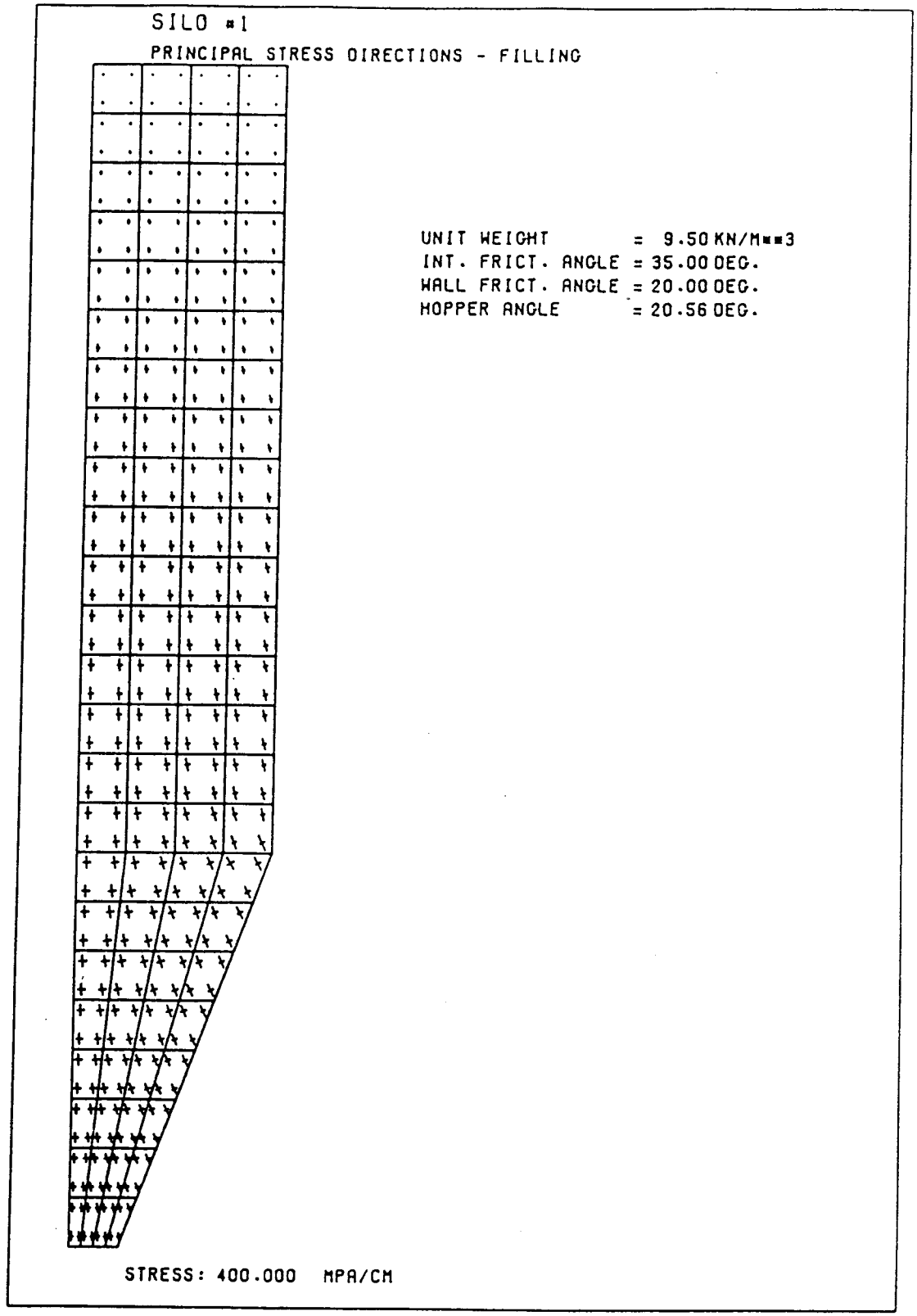

Figure 6.6 Principal stress directions - Silo #1

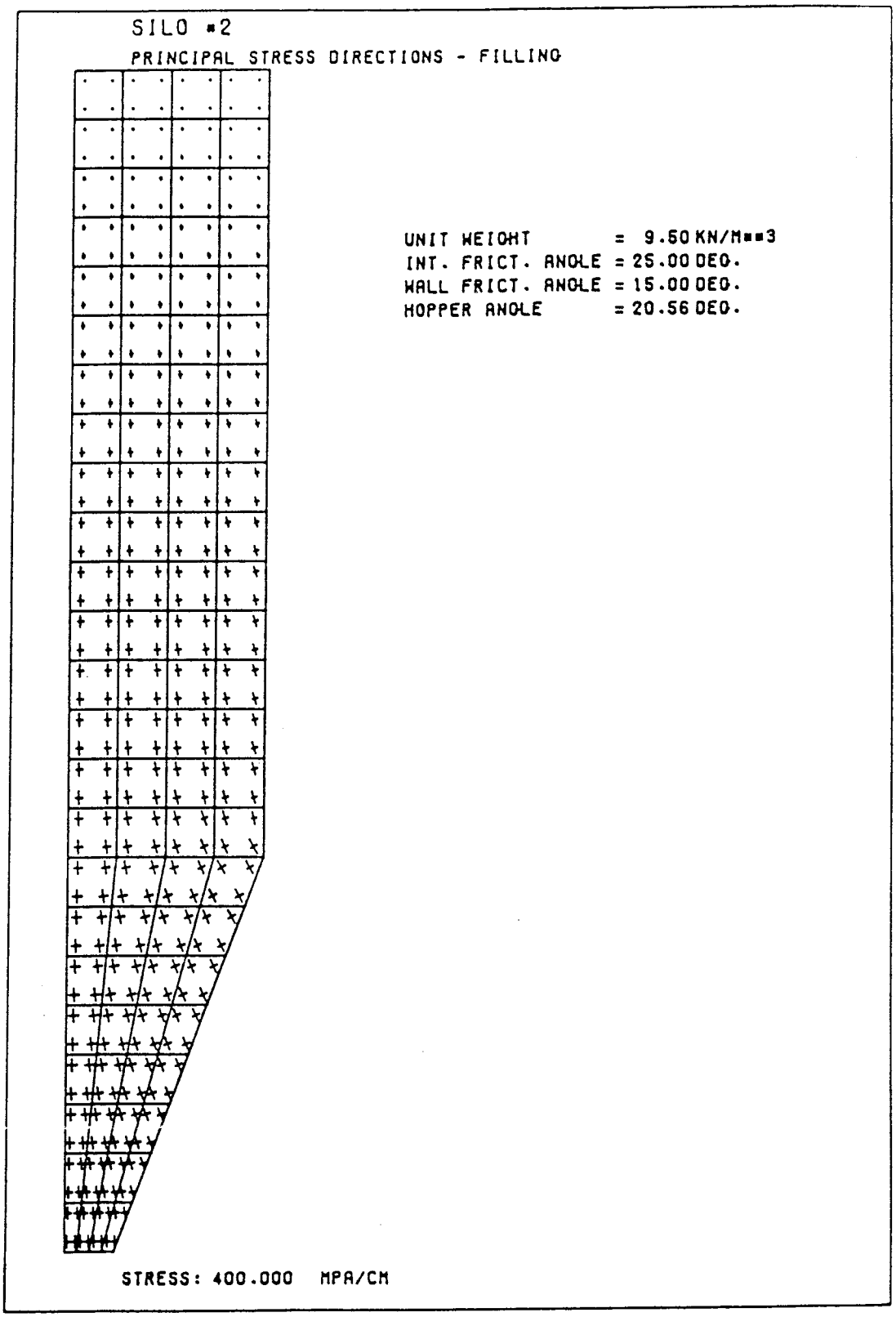

Figure 6.7 Principal stress directions - Silo #2

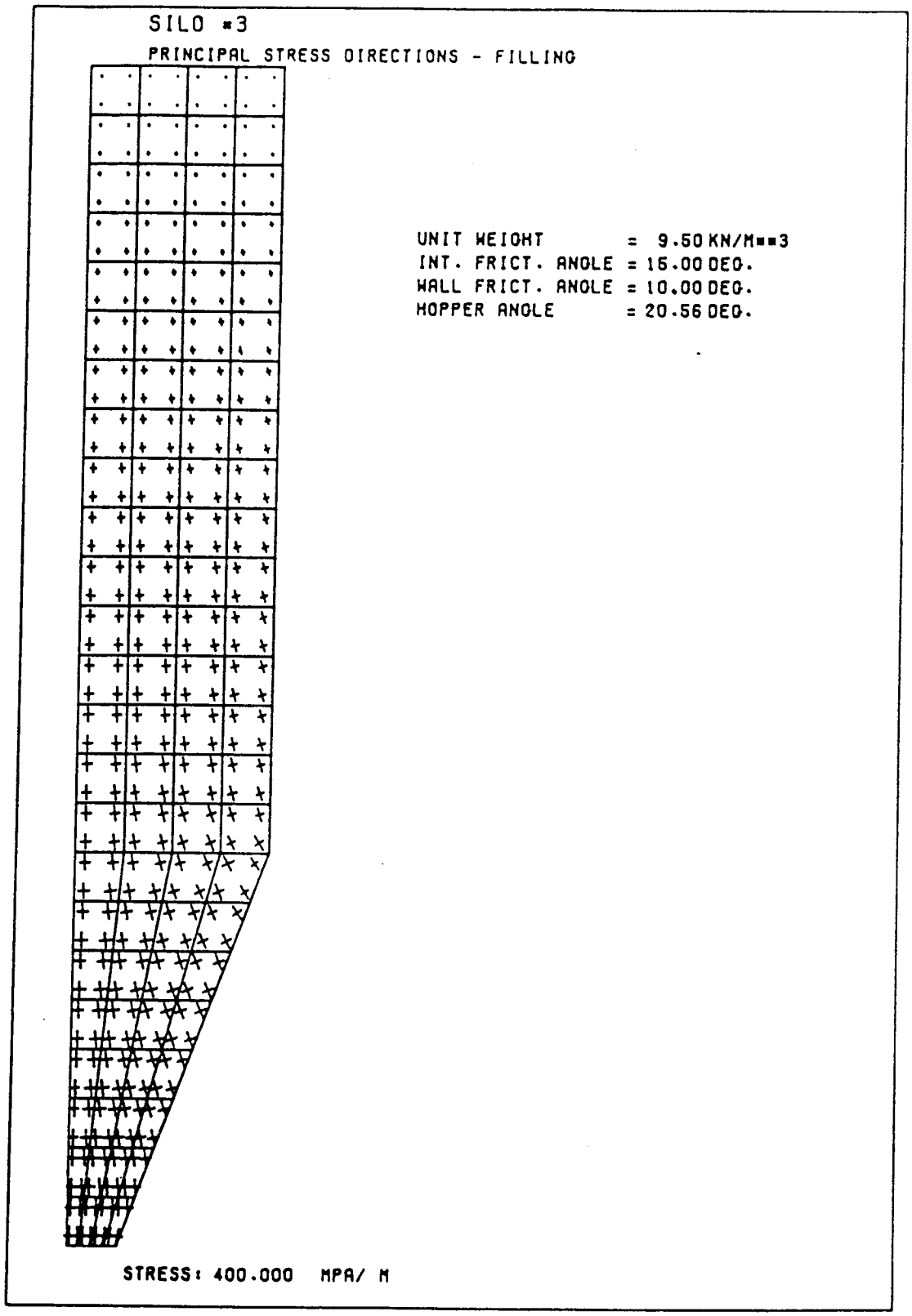

Figure 6.8 Principal stress directions - Silo #3

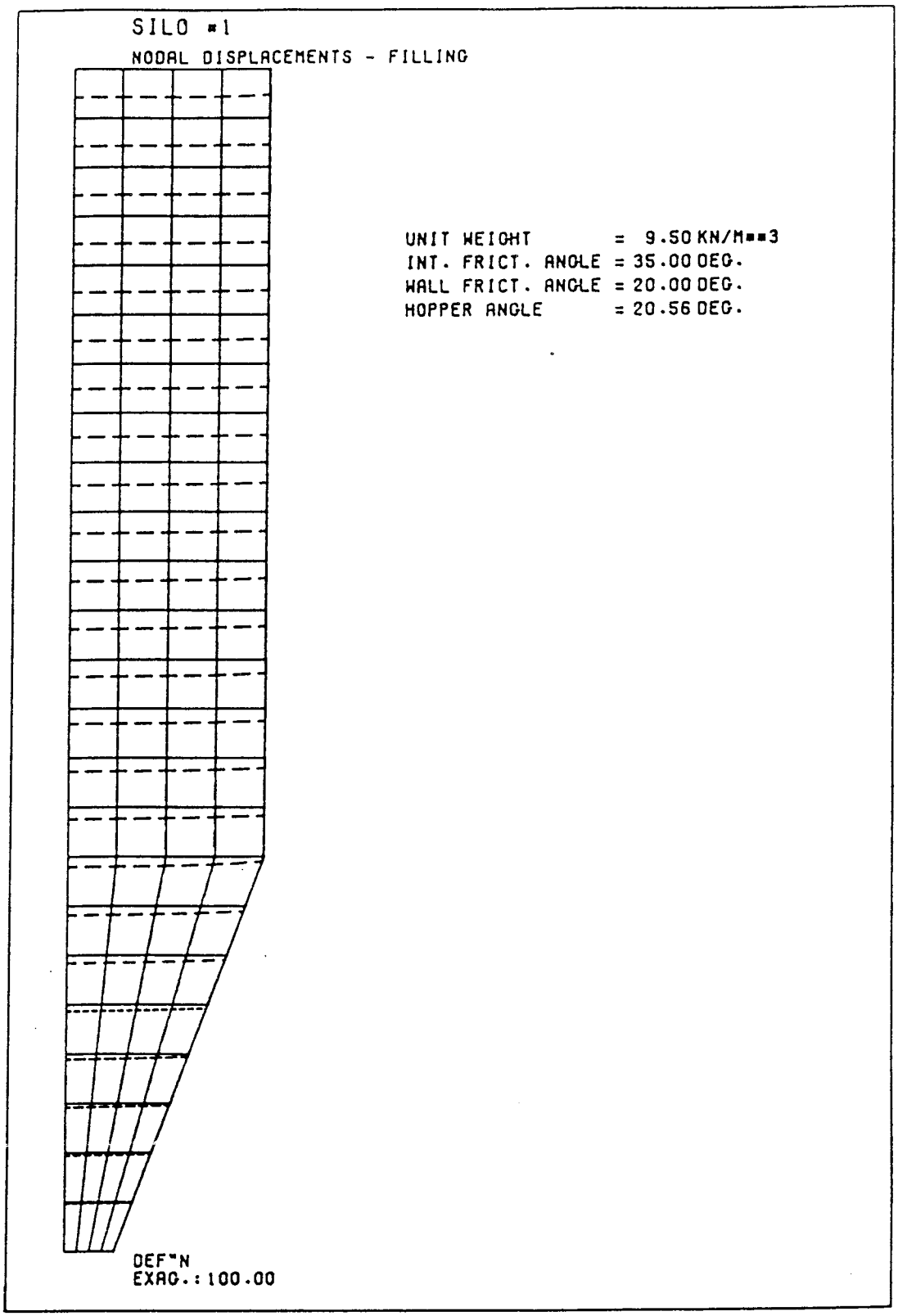

Figure 6.9 Nodal displacements - Silo #1

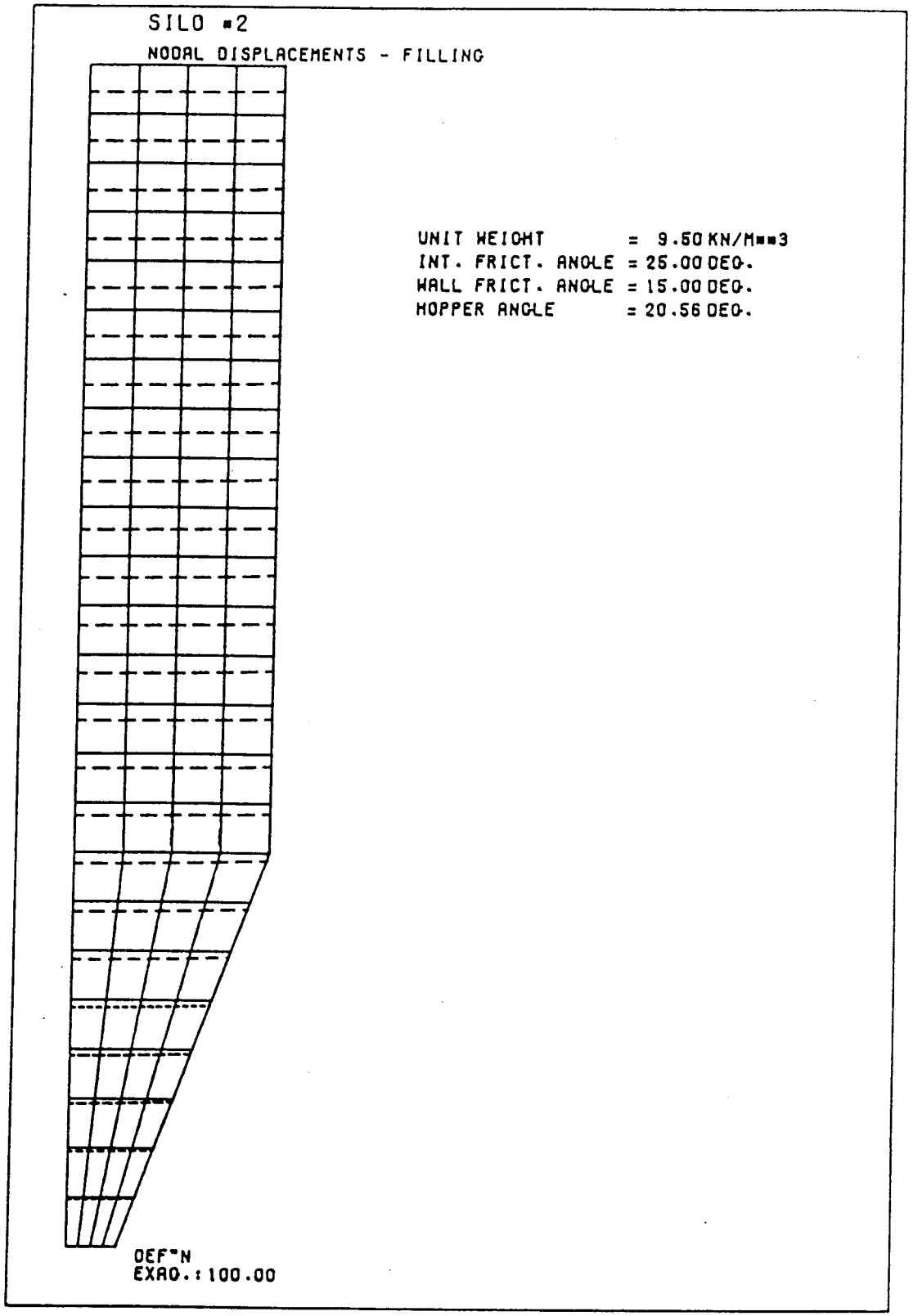

Figure 6.10 Nodal displacements - Silo #2

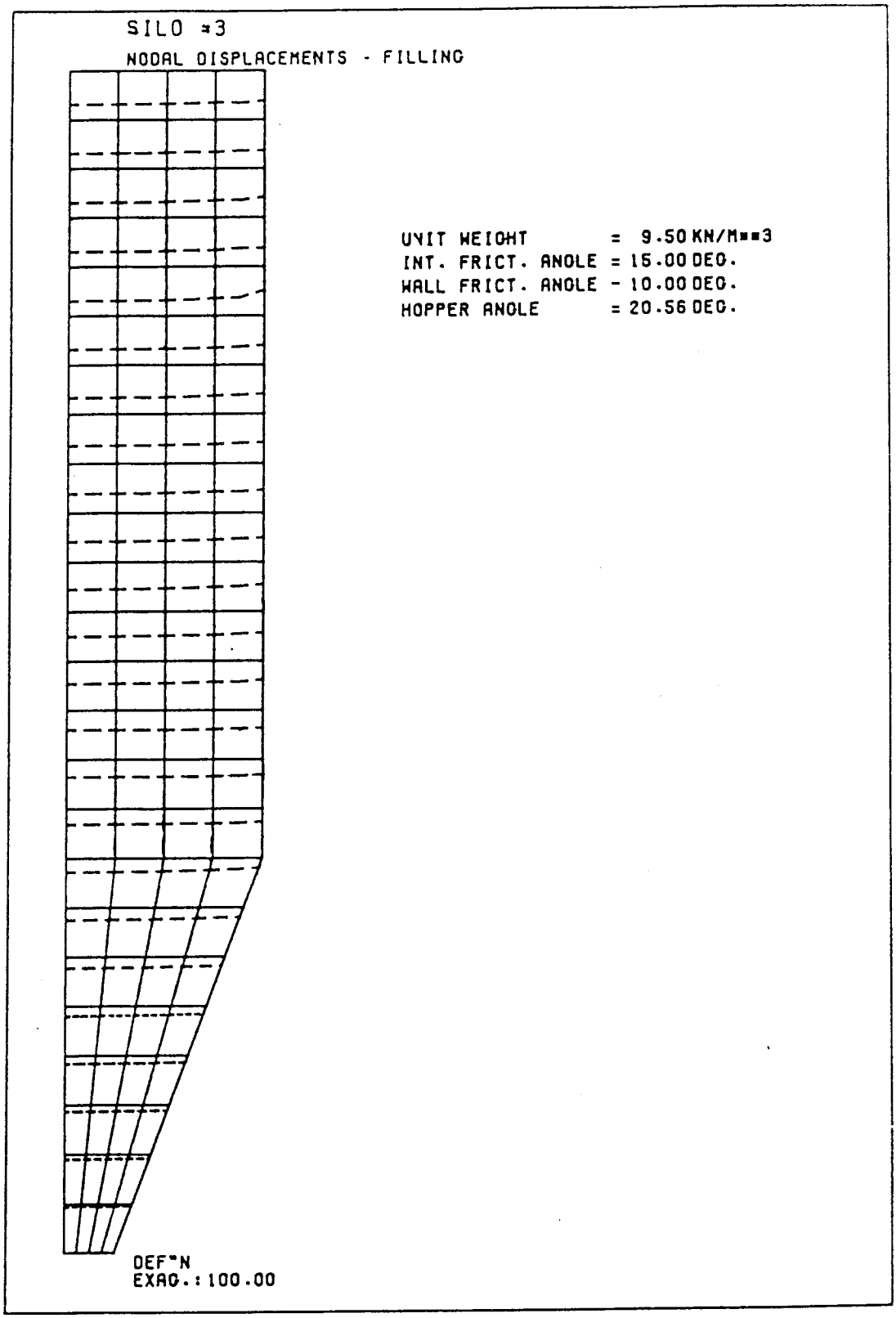

Figure 6.11 Nodal displacements - Silo #3

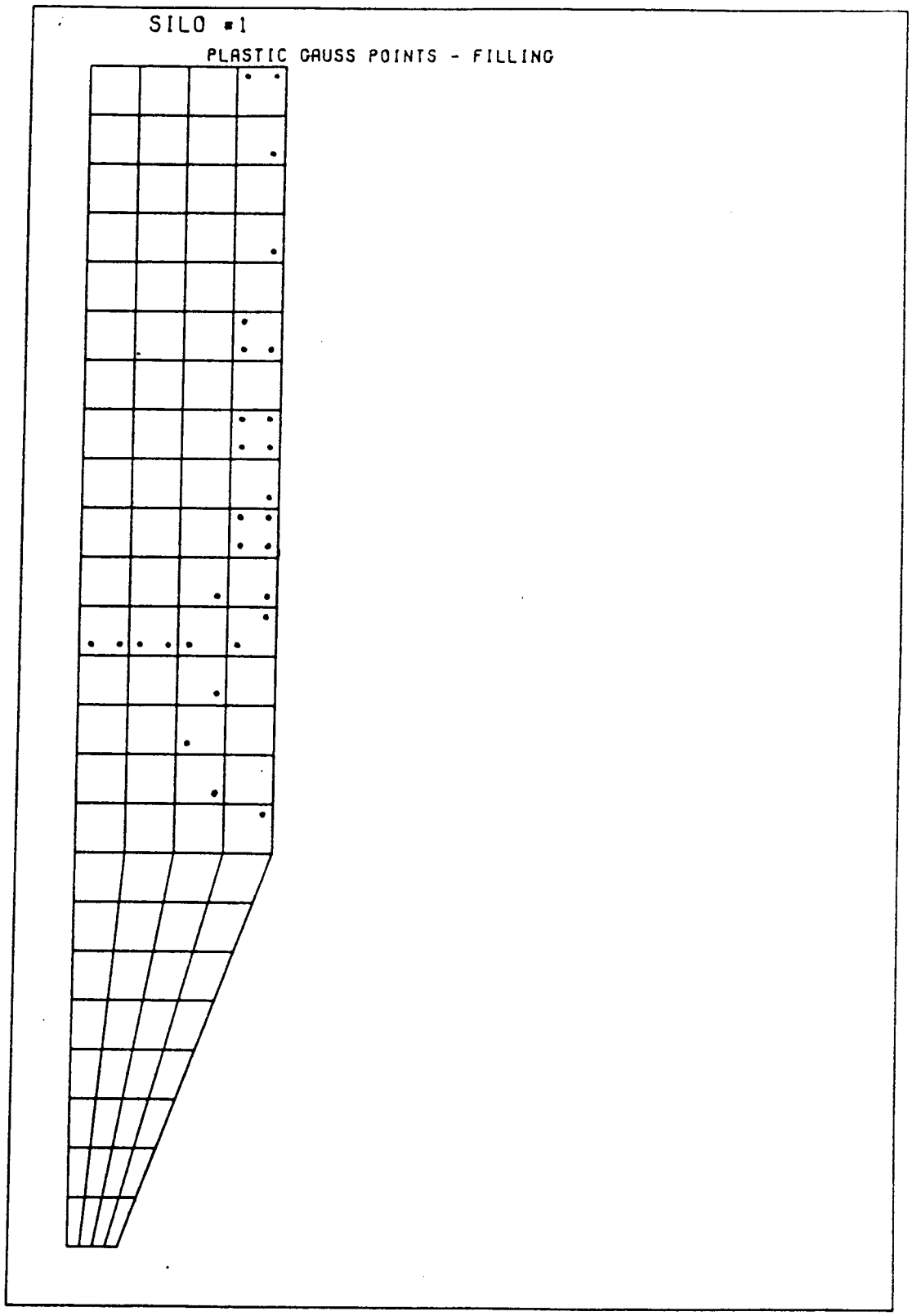

Figure 6.12 Plastic Gauss points - Silo #1

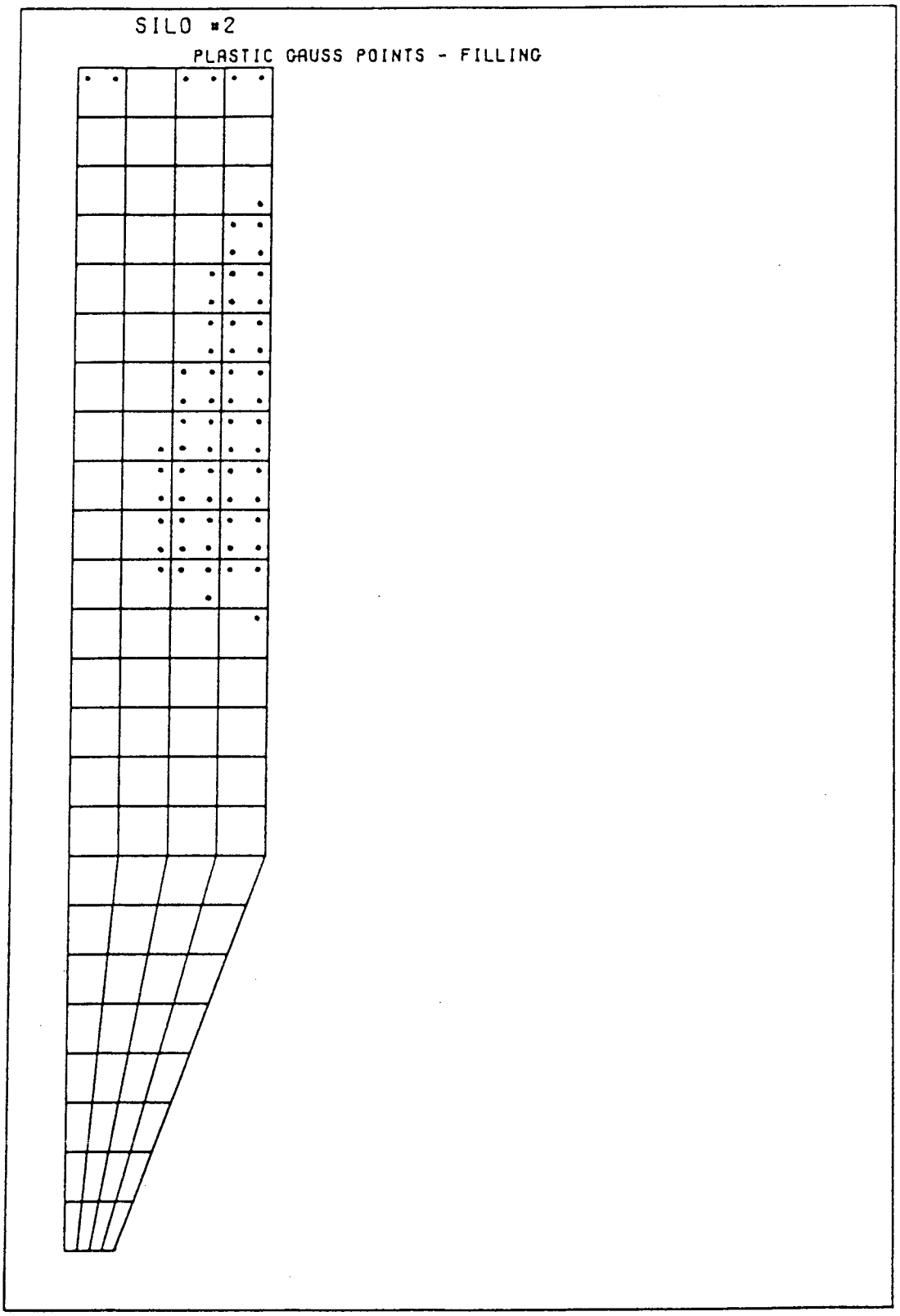

Figure 6.13 Plastic Gauss points - Silo #2

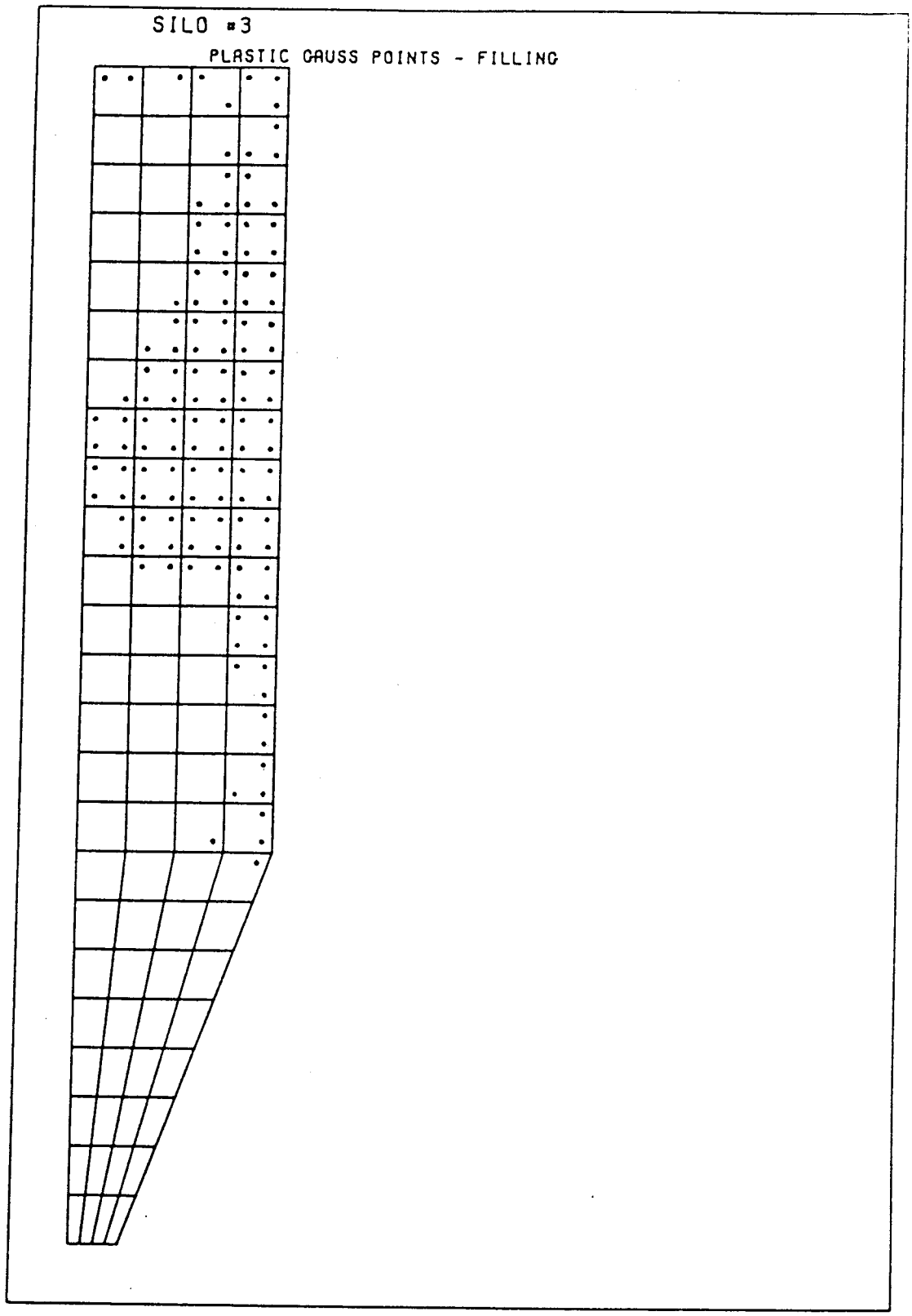

Figure 6.14 Plastic Gauss points - Silo #3

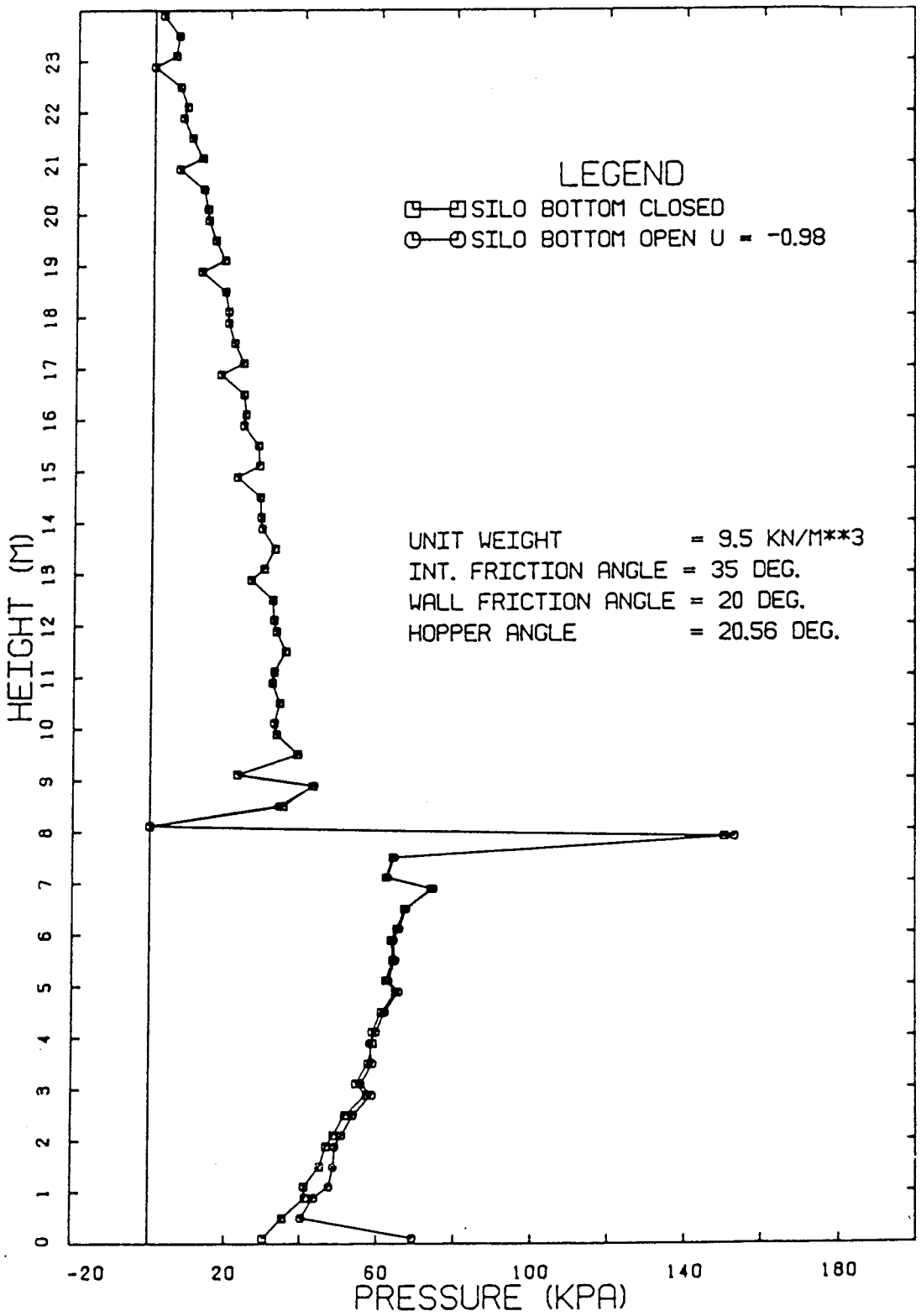

Figure 6.15 Incipient flow wall pressures - Silo #1

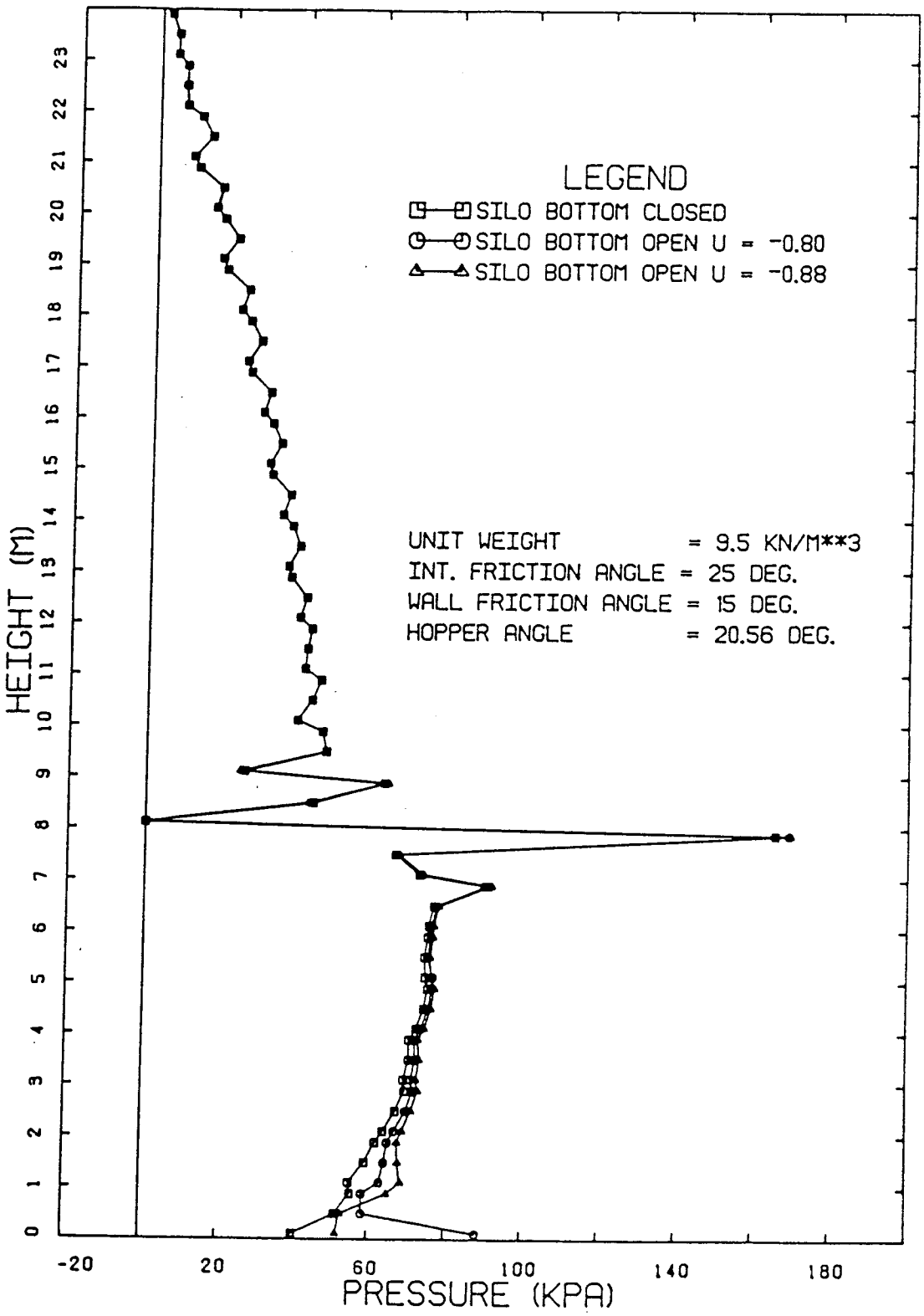

Figure 6.16 Incipient flow wall pressures - Silo #2

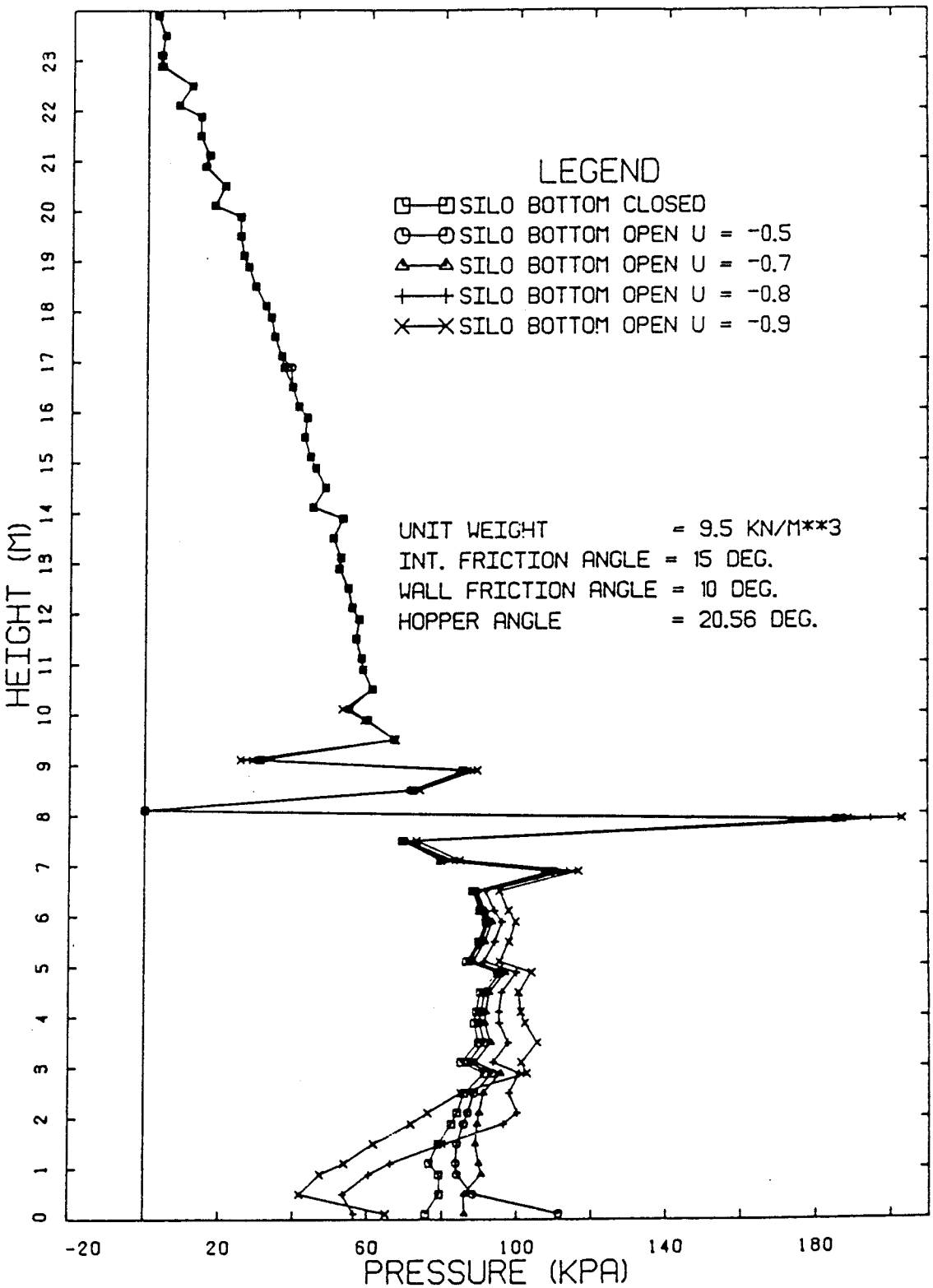

Figure 6.17 Incipient flow wall pressures - Silo #3

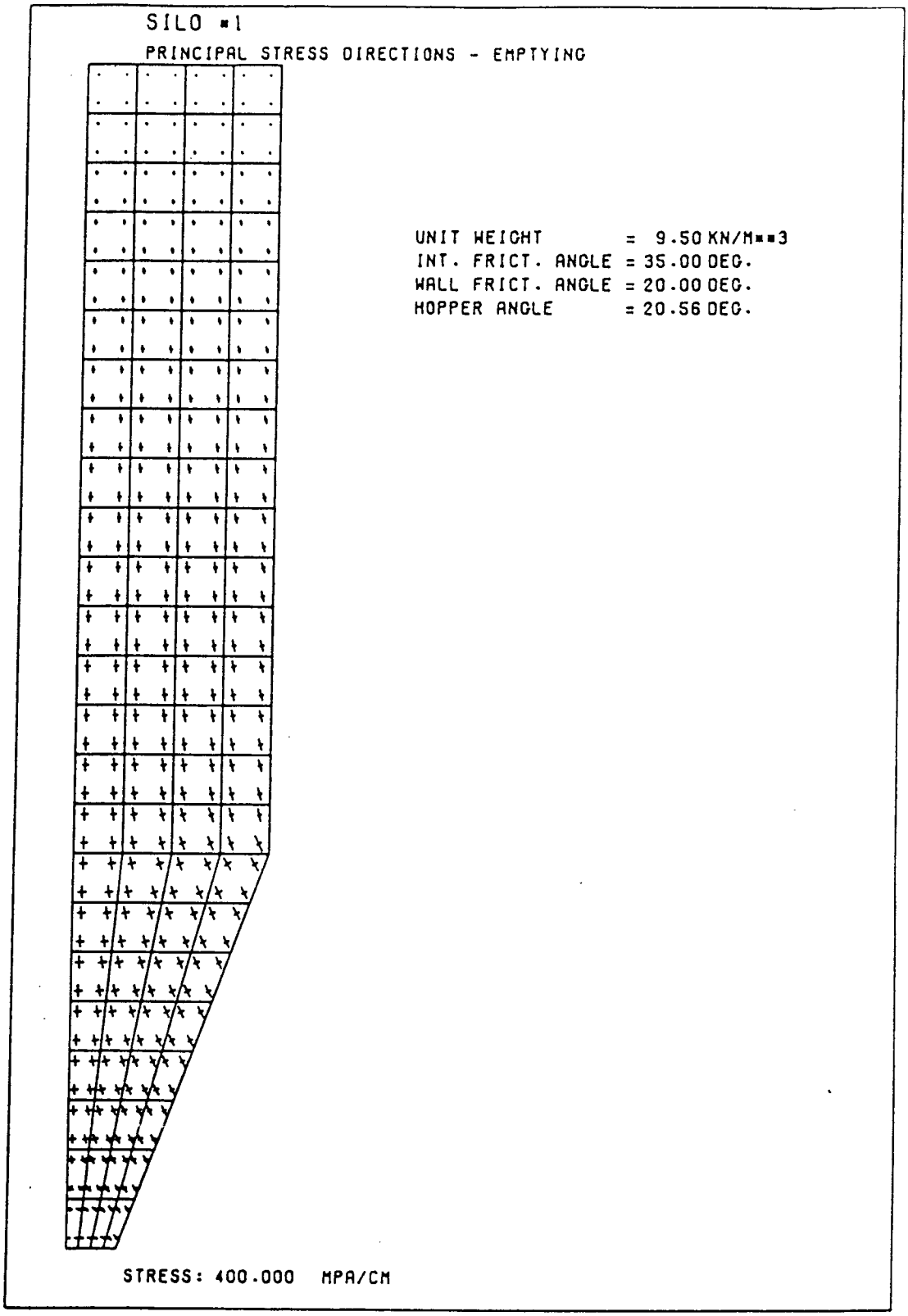

Figure 6.18 Principal stress directions U = -0.98 Silo #1

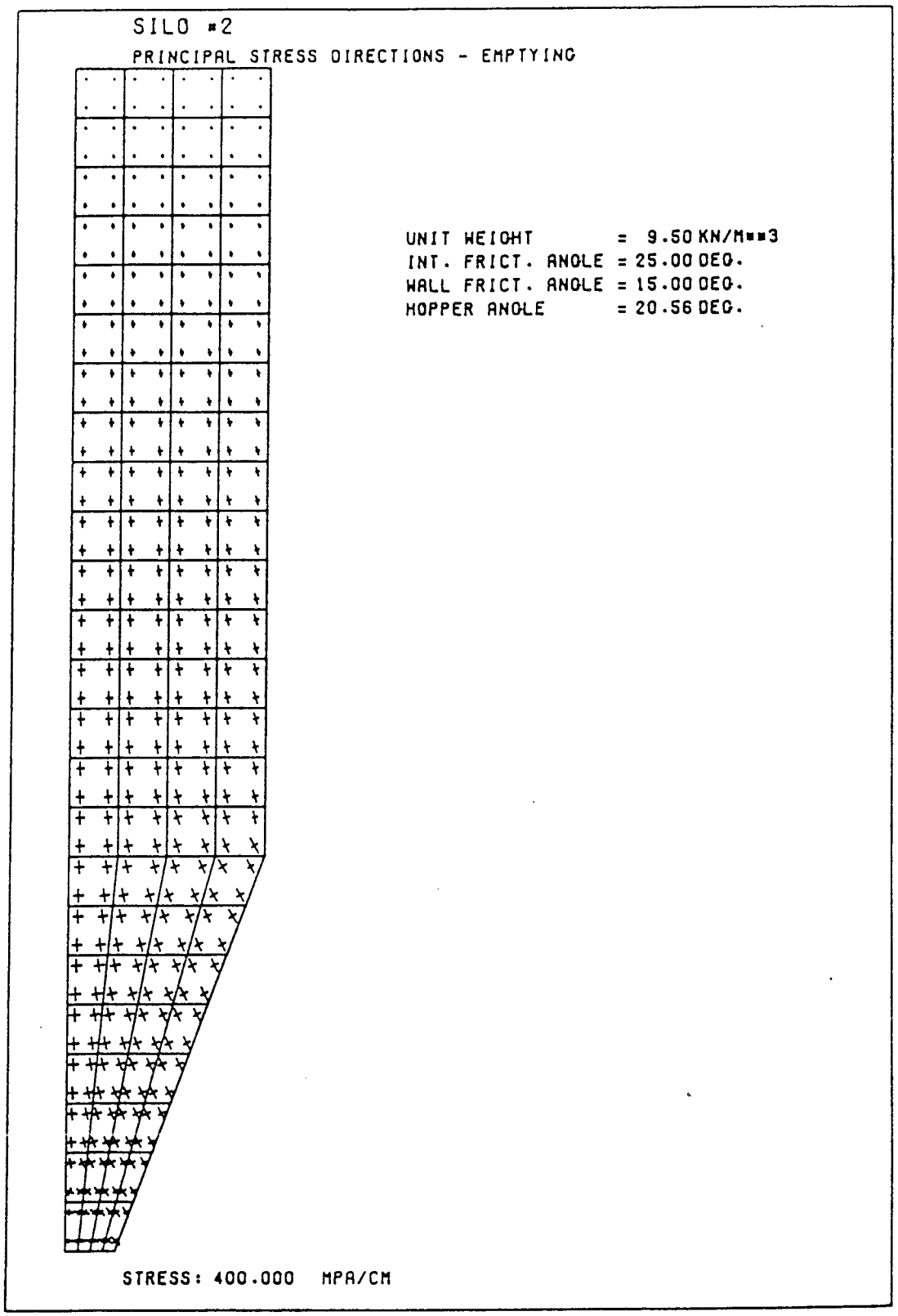

Figure 6.19 Principal stress directions U = -0.88 Silo #2

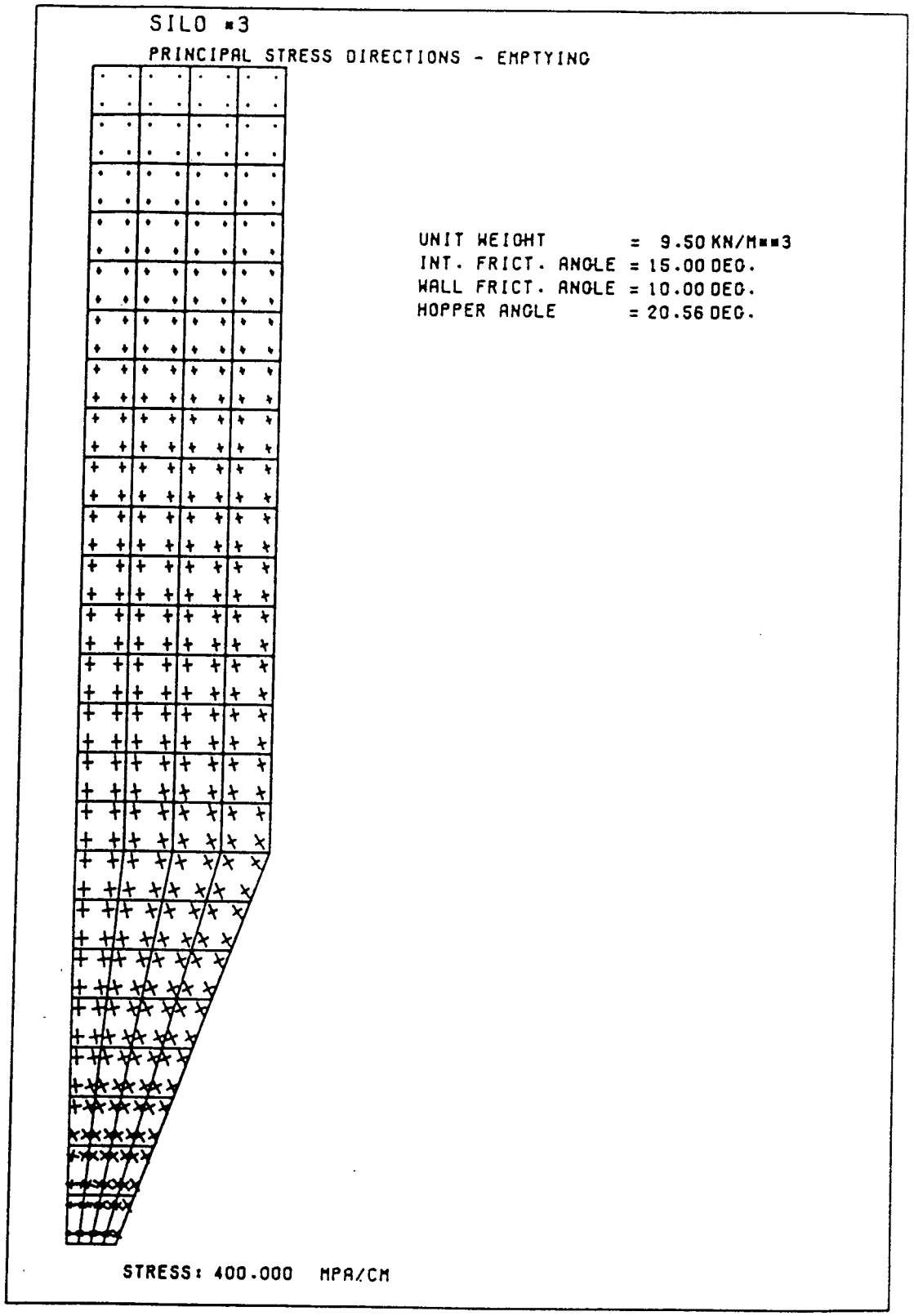

Figure 6.20 Principal stress directions U = -0.70 Silo #3

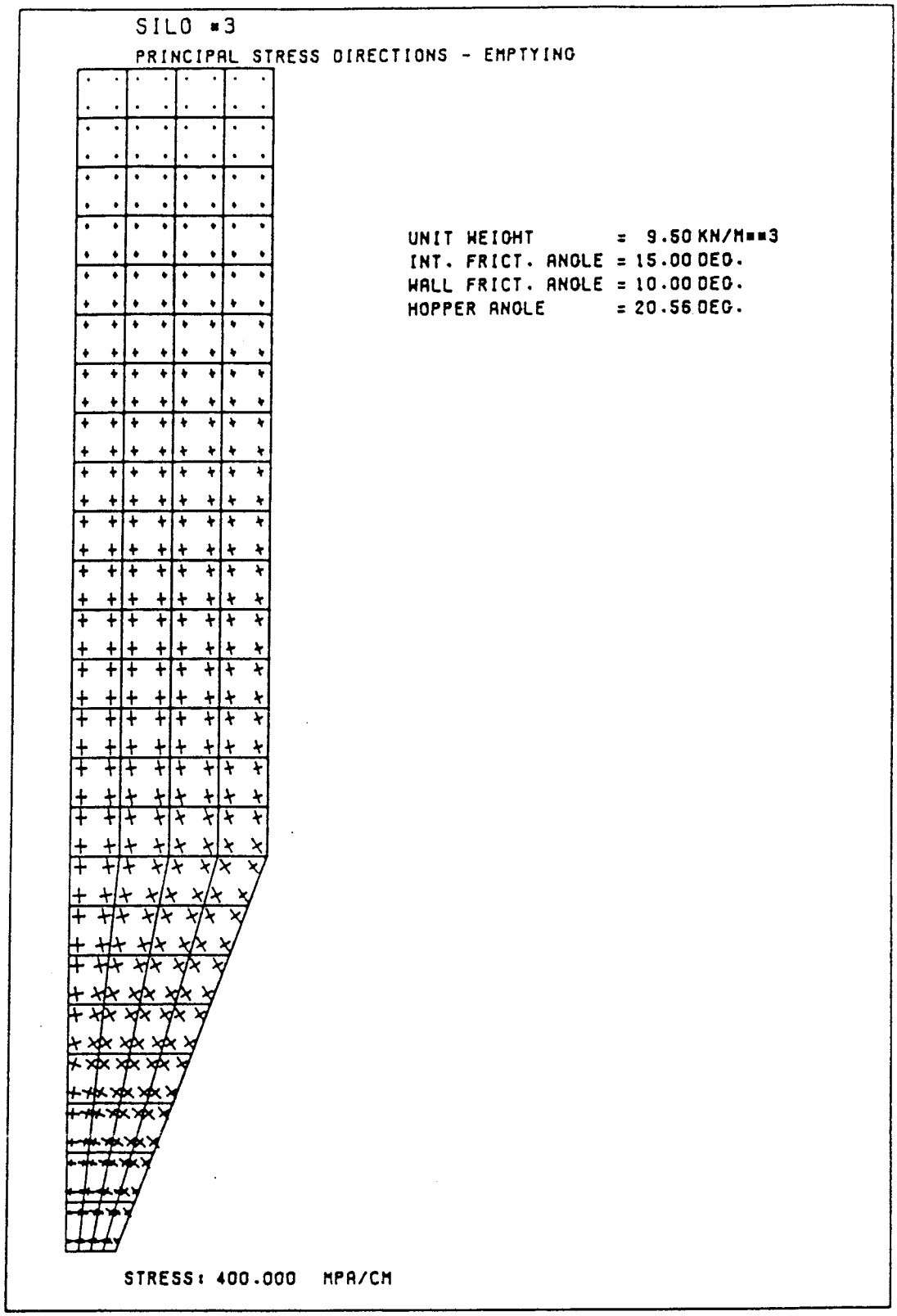

Figure 6.21 Principal stress directions U = -0.80 Silo #3

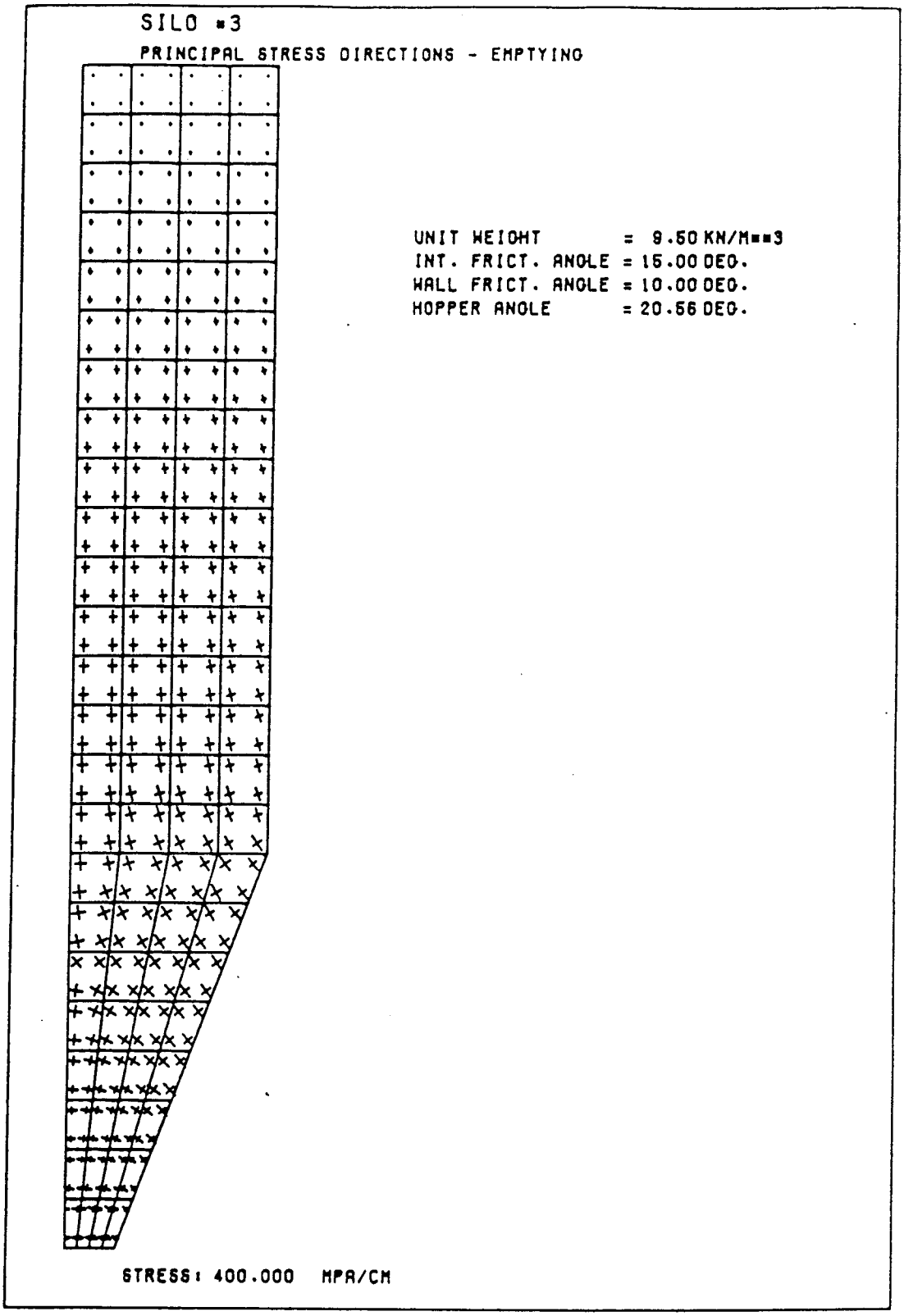

Figure 6.22 Principal stress directions U = -0.90 Silo #3

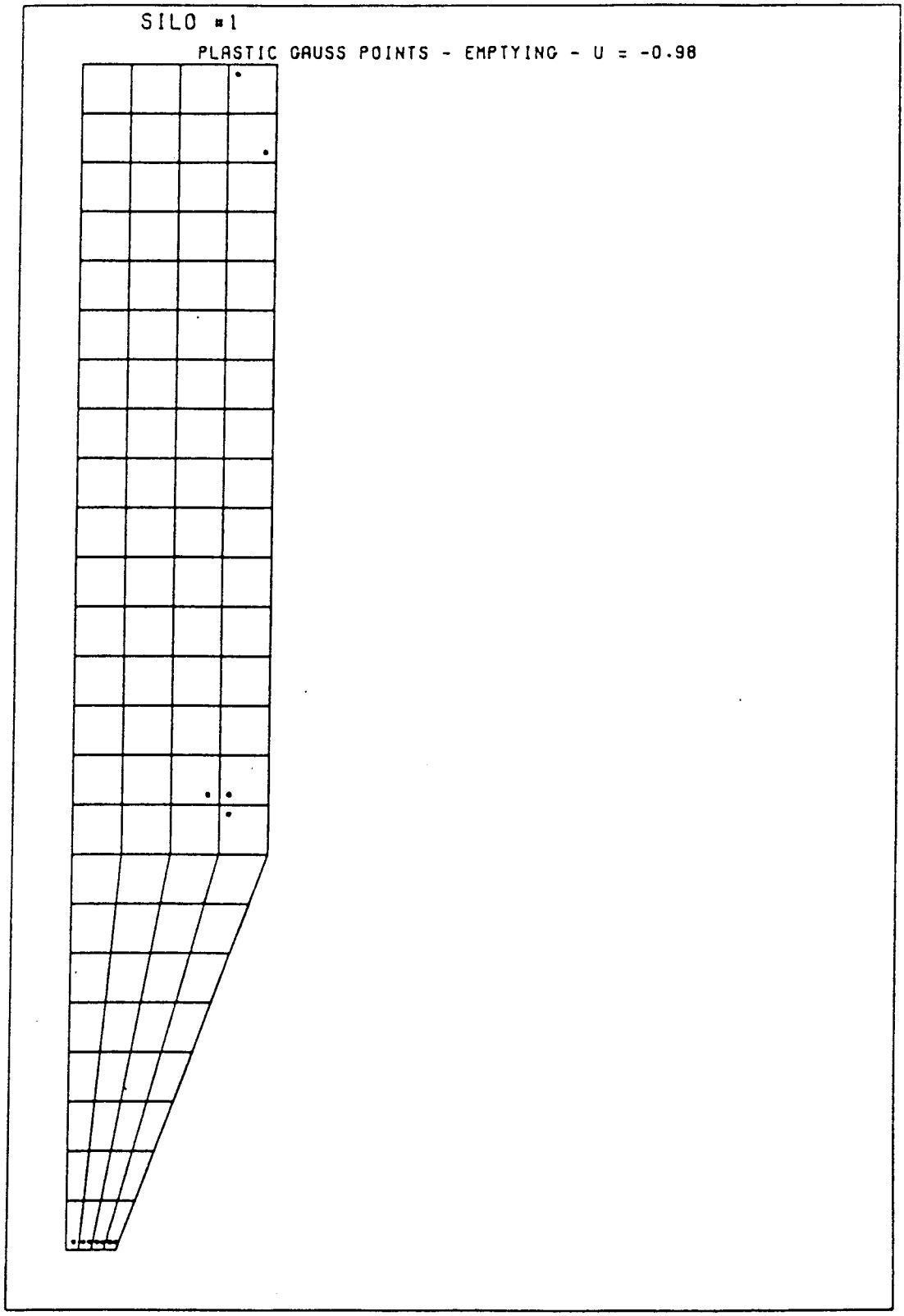

Figure 6.23 Plastic Gauss points U = -0.98 Silo #1

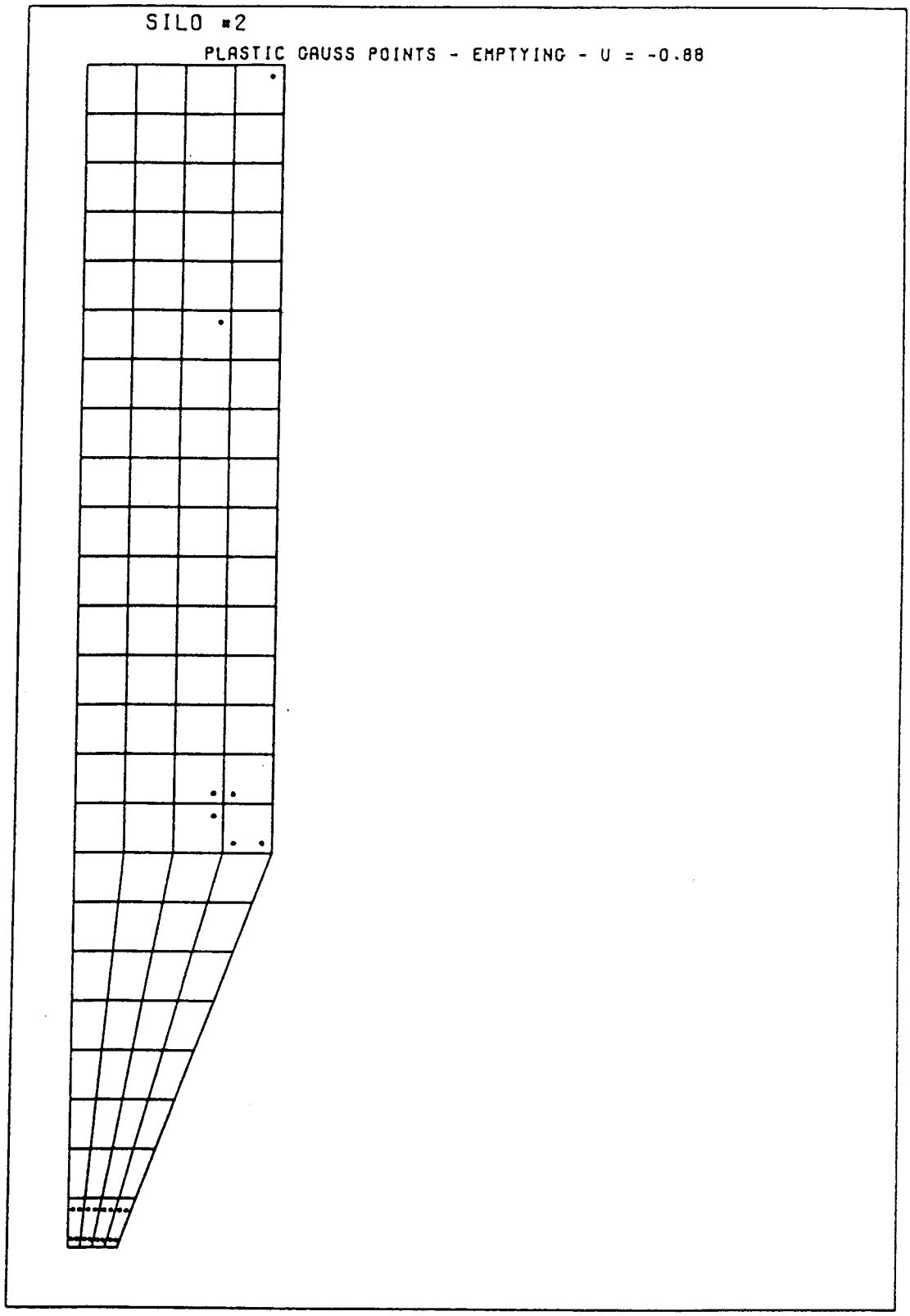

Figure 6.24 Plastic Gauss points U = -0.88 Silo #2

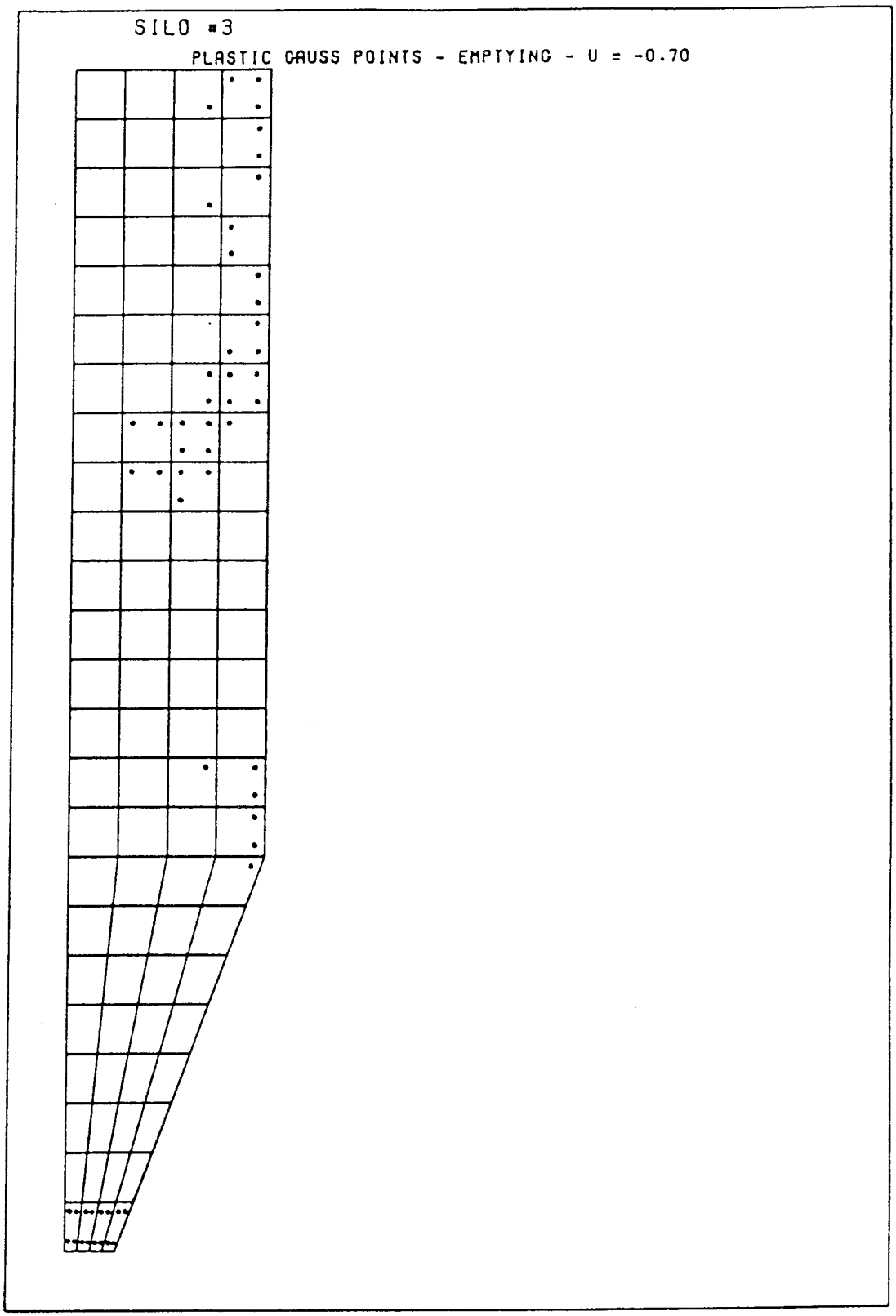

Figure 6.25 Plastic Gauss points U = -0.70 Silo #3

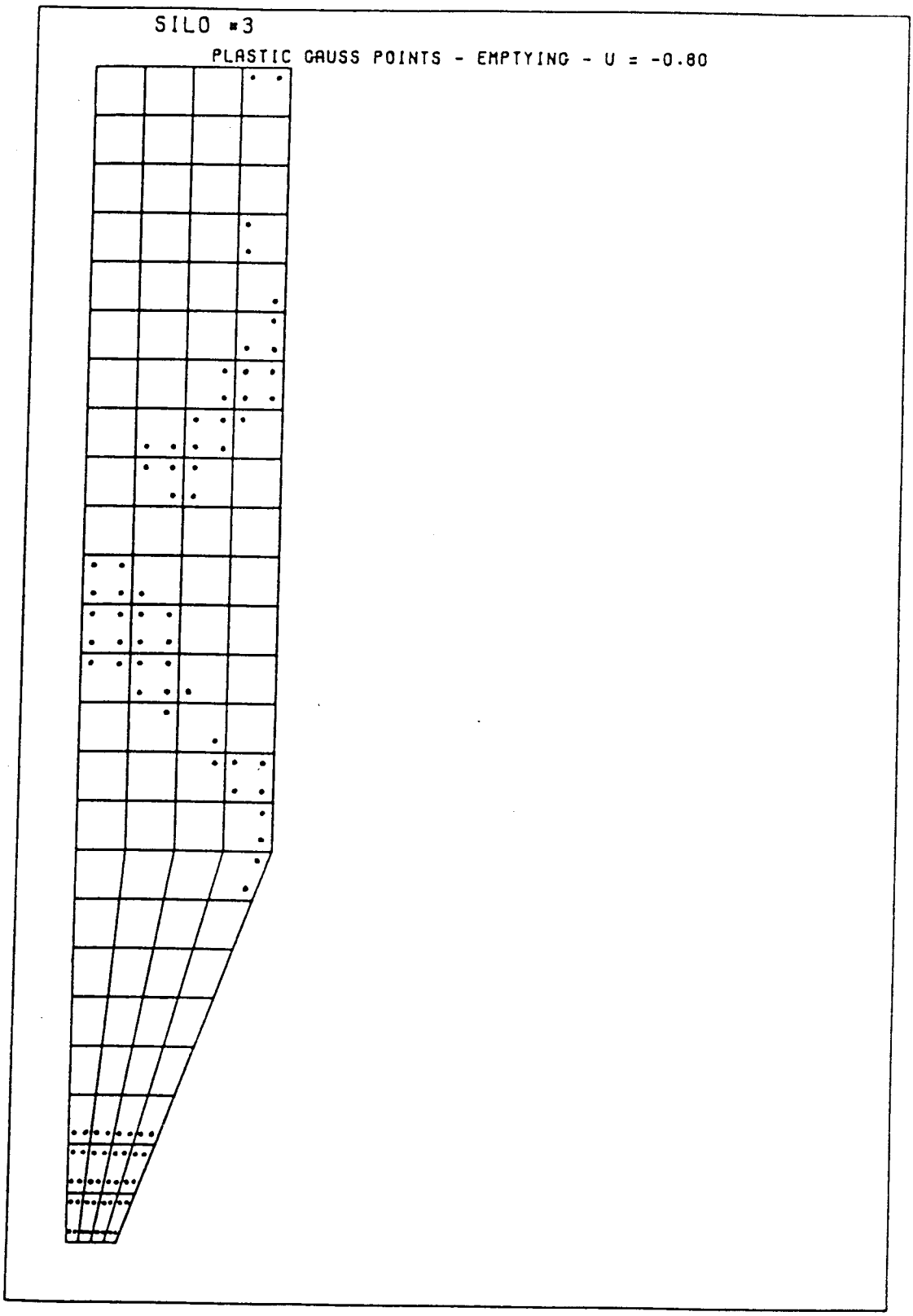

Figure 6.26 Plastic Gauss points U = -0.80 Silo #3

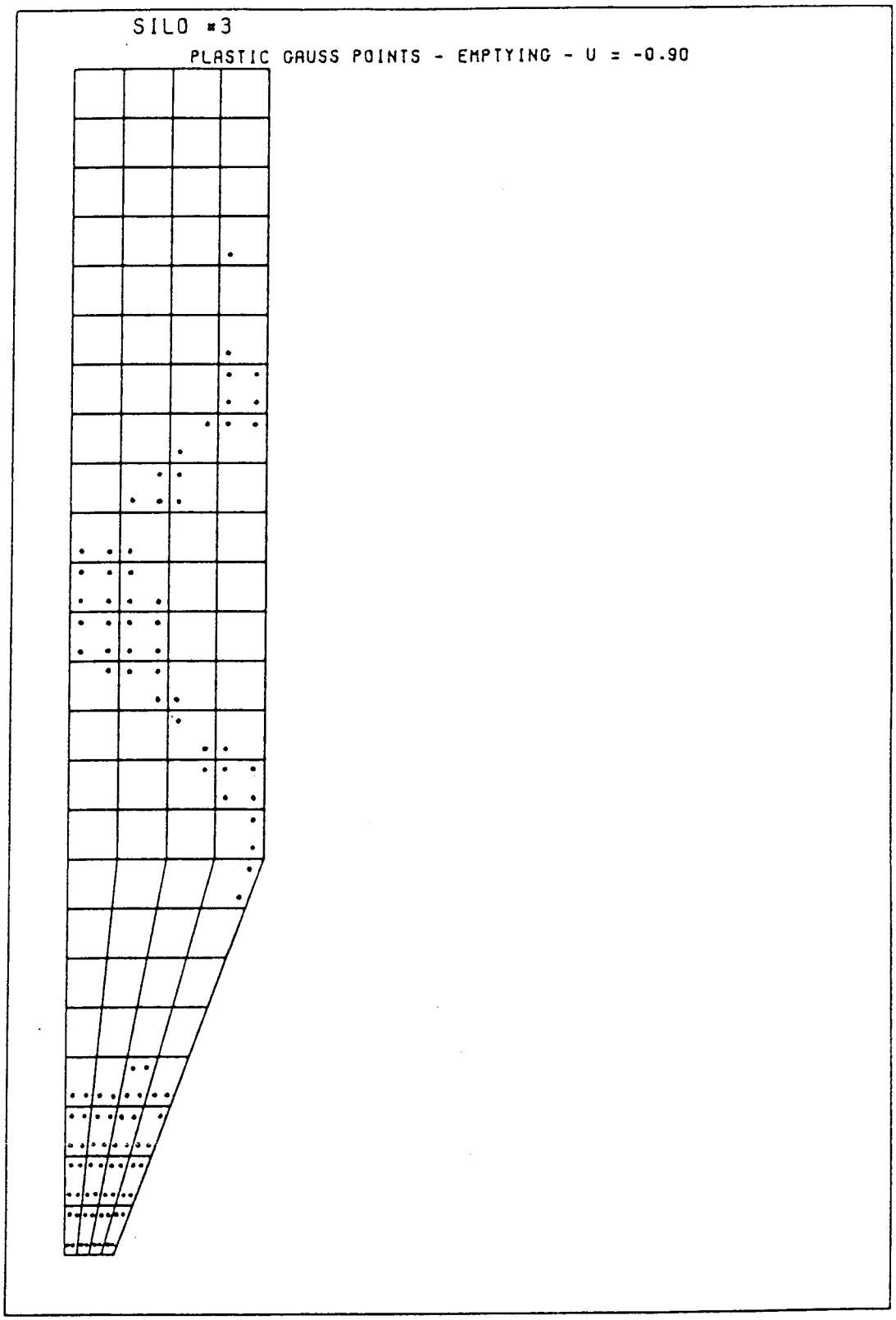

Figure 6.27 Plastic Gauss points U = -0.90 Silo #3

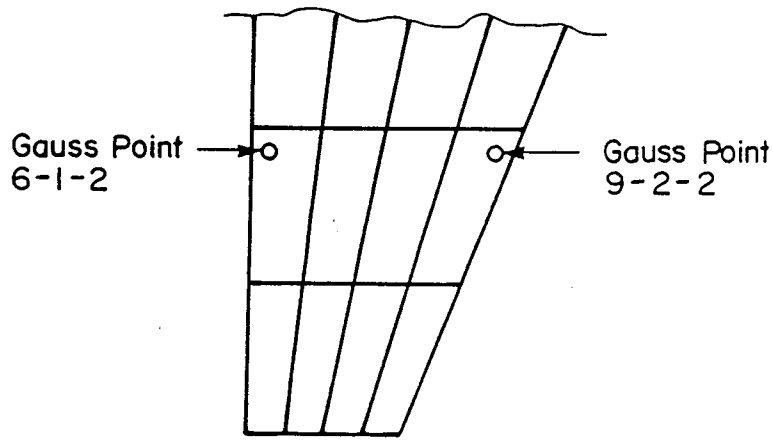

Figure 6.28 Location of selected Gauss points

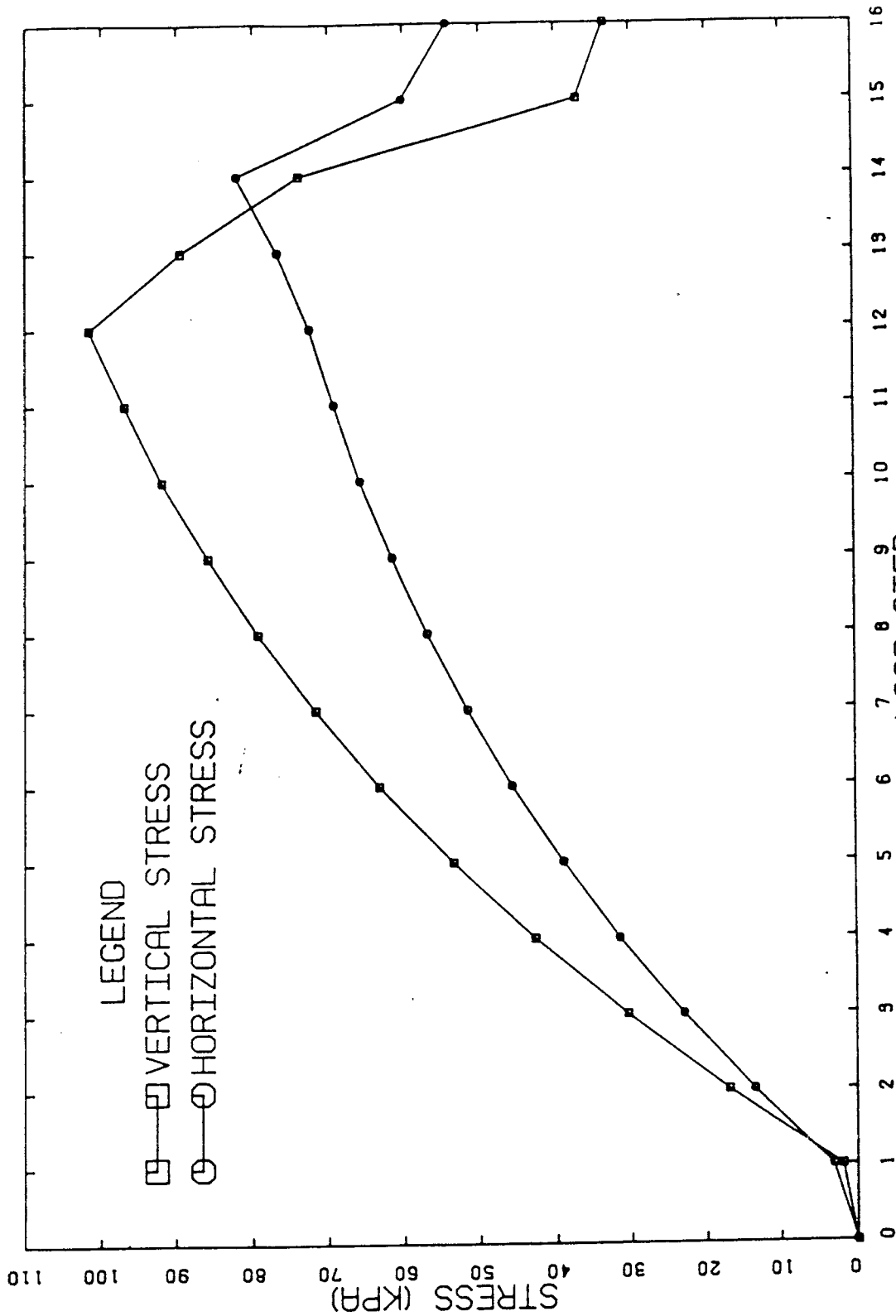

Figure 6.29 Stress history for Gauss point 6-1-2

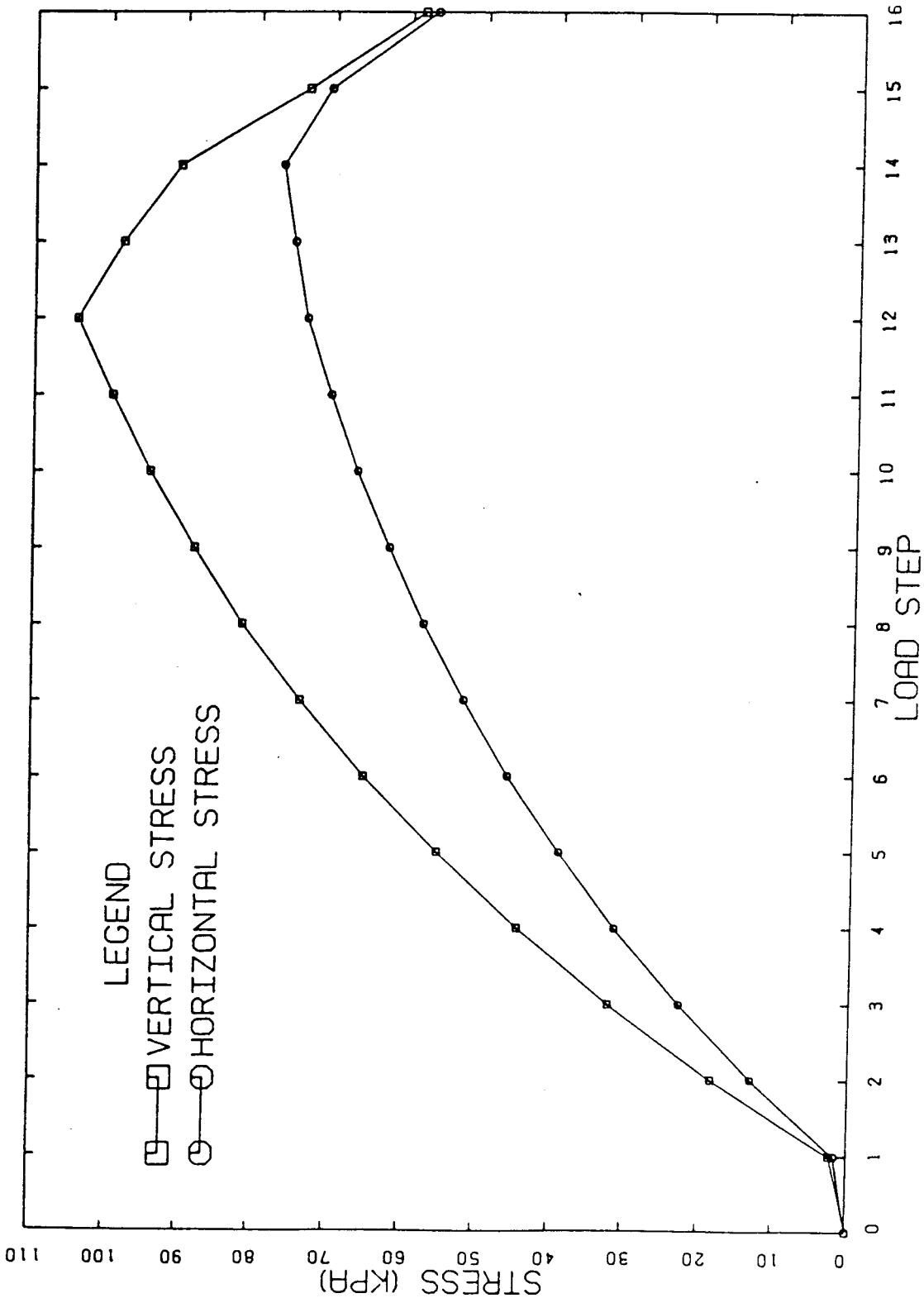

Figure 6.30 Stress history for Gauss point 9-2-2

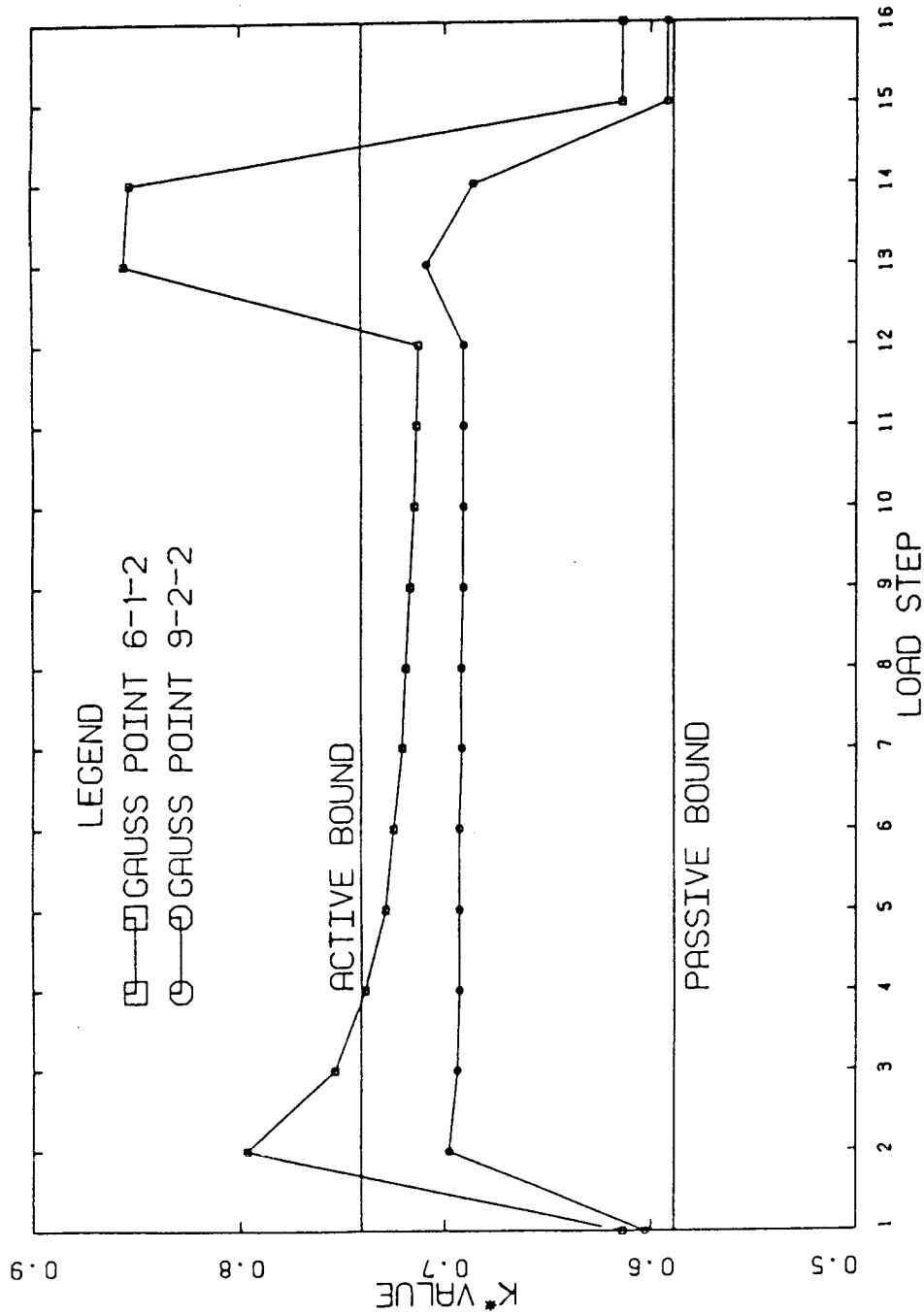

Figure 6.31 Ratio of minor to major principal stresses (K*) vs. stress history for selected Gauss points

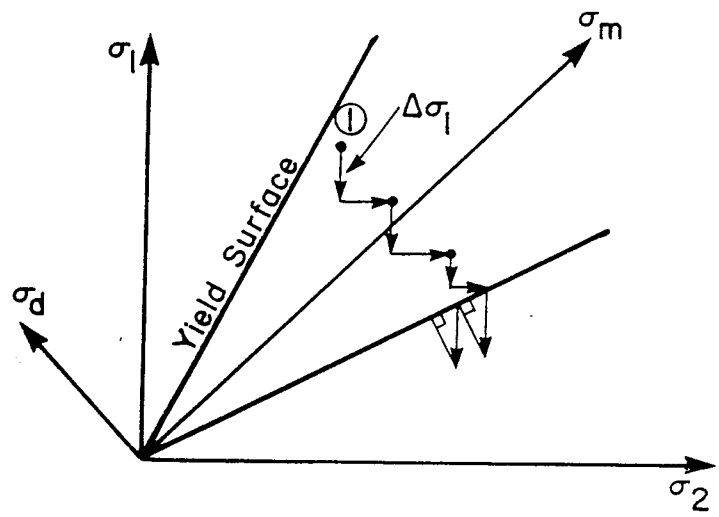

Figure 6.32 Stress path of material during outlet release

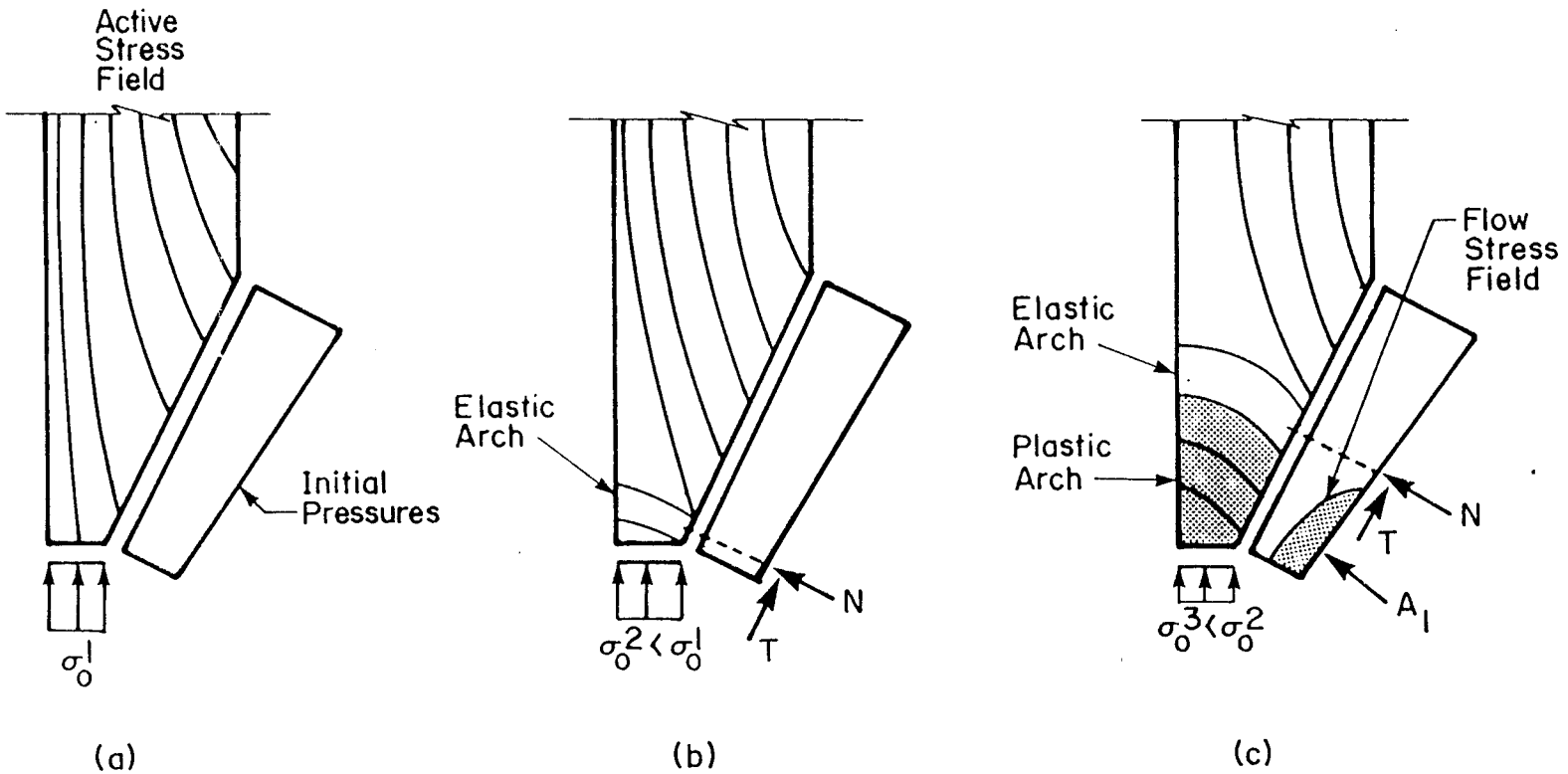

Figure 6.33 Incipient failure model

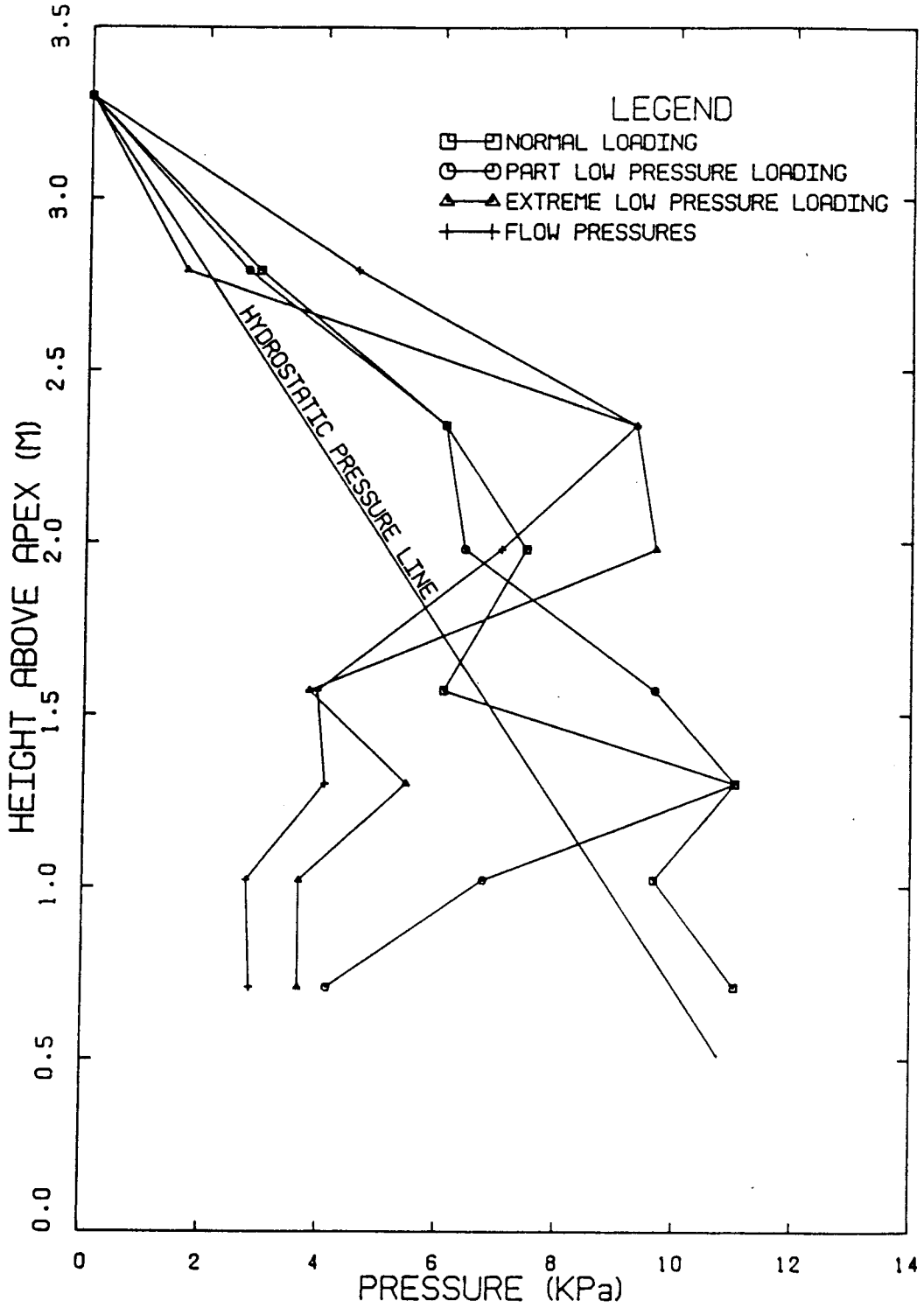

Figure 6.34 Pressure curves for 15° pyramidal hoppers (Adapted from Walker and Blanchard 1967)

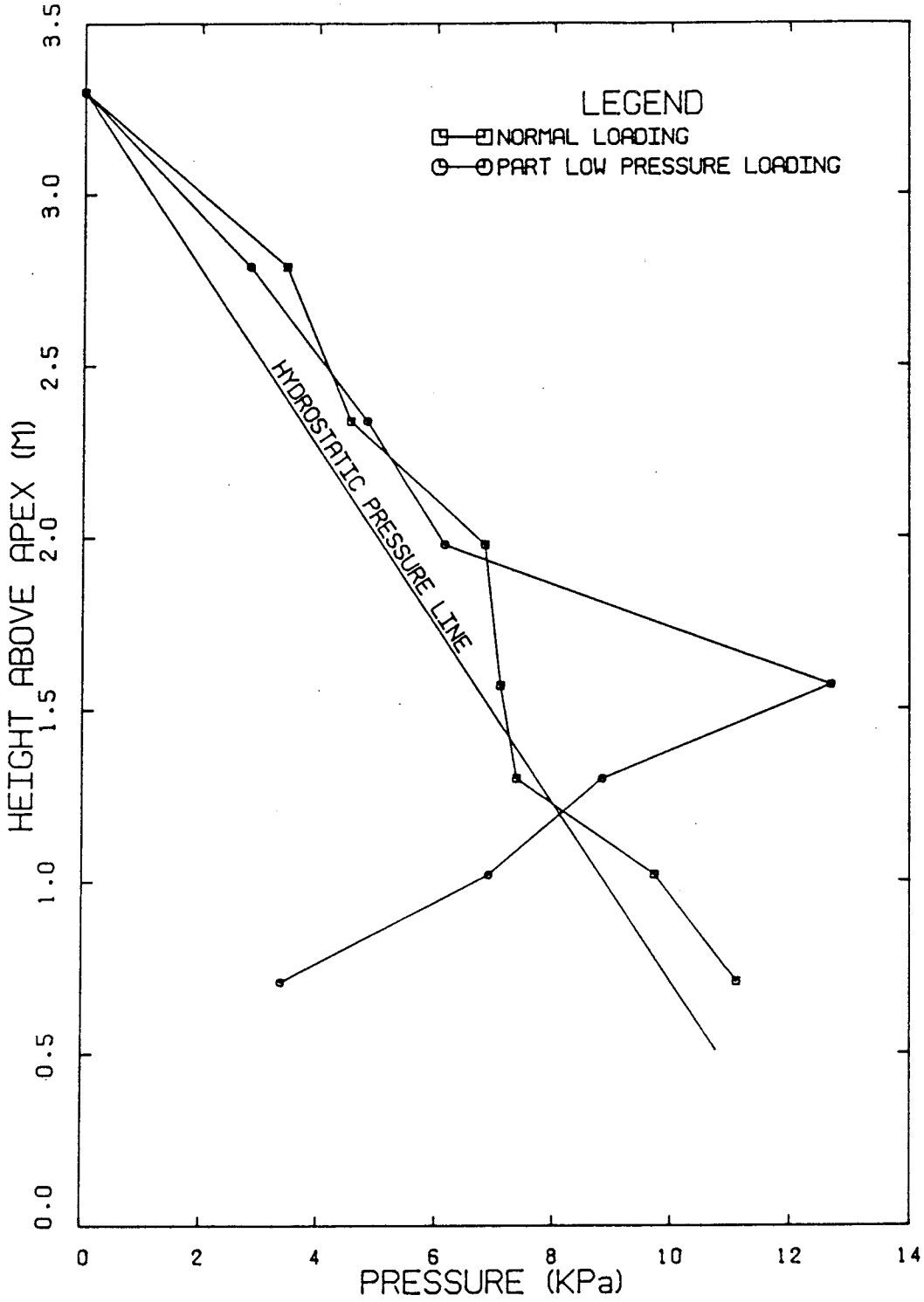

Figure 6.35 Pressure curves for 15° conical hoppers (Adapted from Walker and Blanchard 1967)

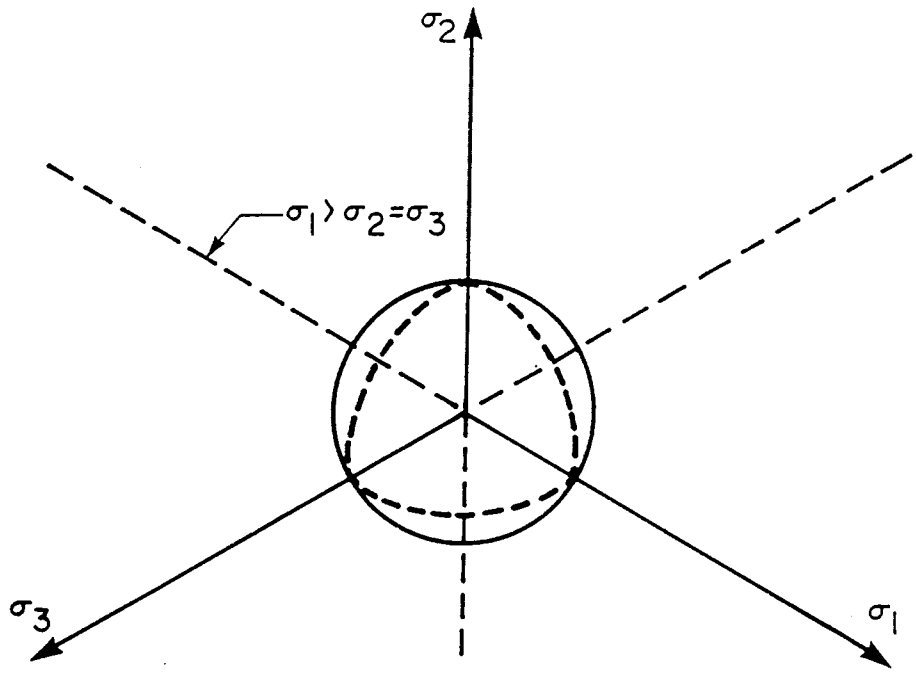

(a) Octahedral Plane Properties

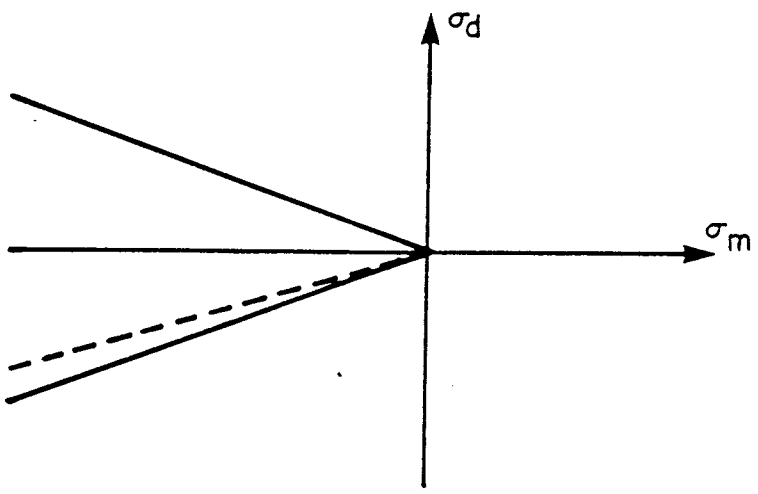

(b) Rendulic Plane Properties

Figure 6.36 Comparison of Drucker-Prager yield surface with actual yield surface

7. SUMMARY AND CONCLUSIONS

A nonlinear incremental static finite element formulation of the silo problem is presented. The analysis includes the effects of nonlinear material behavior, load history, and wall friction on silo wall pressures.

Nonlinear material behavior is idealized by using a Drucker-Prager yield surface. Previous numerical difficulties encountered by Askari (1986) are avoided by using a stepwise stress increment to intersect the yield surface. The effects of load history are modelled using a layering technique in which layers of elements were placed as filling proceeded. Wall friction is modelled with a thin layer interface element. The interface element is capable of simulating the interface state of stick, slip, and debond. In addition, the element has rebonding capabilities.

The finite element results of three analyses carried out on an axisymmetric silo using different material and wall friction properties are presented and compared with the classical theories of Jenike, Walker, and Janssen. The analyses simulate initial filling and opening of the outlet to the initiation of incipient flow. The wall pressures during initial filling gave good agreement with solutions obtained by Jenike and Janssen. The assumption of an active stress field made by Jenike and Janssen was justifed based on inspection of the principal stress directions.

The stress field during incipient flow was similar in orientation to the arched field assumed by Jenike. Results

indicated the initial formation of an elastic arch at the outlet, followed by a stress reduction due to yield and subsequent upward movement of the elastic arch. This is in partial agreement with Jenike's assumption of a moving switch point. Switch pressures obtained at the outlet are greater than static pressures, but smaller than those obtained using Jenike's and Walker's solutions. It is suggested that the switch "point" has a finite thickness, and distribution of the unbalanced load over this thickness has the effect of reducing wall pressures. Thus, design pressures may be between the static pressure and those pressures predicted by Jenike and Walker.

Current design procedures do not recognize the existence of incipient flow overpressures in hoppers, even though there is evidence, both experimental and theoretical, as to their existence. Ignoring these overpressures is unconservative, since these pressures can be "locked in", and act as static loads. The author suggests the use of an influence type analysis, instead of a pressure envelope, to determine load effects on the silo structure. Since switch pressures are found to be in between static pressures and those obtained by classical flow pressure theories, it is suggested that Jenike's and Walker's solutions can be used to obtain a conservative estimate of wall pressures.

It was not possible to develop an extensive plastic hopper stress field (assumed by Jenike during flow conditions) in the stronger materials. Possible reasons

include the conservative strength characteristics and high dilatency ratio of the Drucker-Prager yield surface, and the exclusion of viscous and inertial effects.

It is recommended that a viscoplastic analysis be the next step in research. Determination of flow parameters (analogous to viscosity) may not be important, since there is some evidence (Eibl and Häussler 1984) that a significant viscosity change causes only a small change in material stresses. In addition, a more realistic yield surface similar to Lade's (1977) should be used.

It is believed that the new interface element developed in this work may be of significant value in small displacement problems. However, further work is needed to investigate the numerical stability of its use.

REFERENCES

1. Askari, A.H., and Elwi, A.E. (1986), "Finite Element Prediction of Bin Loads", Structural Engineering Report No. 135, Department of Civil Engineering, The University of Alberta, Edmonton, Alberta, Canada.
2. Chandrangsu, Karoon, and Bishara, A.G. (1978), "Nonlinear Finite Element Analysis of Farm Silos", Proceedings, ASCE, Vol. 104, No. ST7, pp. 1045-1059.
3. Chen, W.F. (1982), "Plasticity In Reinforced Concrete", McGraw-Hill.
4. Clough, G.W., and Duncan, J.M. (1969), "Finite Element Analyses of Port Allen and Old River Locks", U.S. Army Engineers Waterway Experimental Station, Vicksburg, Mississippi, Contract Report S-69-6.
5. Desai, C.S., Zaman, M.M., Lightner, J.G., and Siriwardane, A.J. (1984), "Thin-Layer Element for Interfaces and Joints", International Journal for Numerical and Analytical Methods in Geomechanics, Vol. 8, pp. 19-43.
6. Drucker, D.C., and Prager, W. (1952), "Soil Mechanics and Plastic Analysis or Limit Design", Q. Appl. Math., Vol. 10, No. 2, pp. 157-165.
7. Eibl, J., and Häussler, U. (1984), "Numerical Investigation on Discharging Silos", Journal of the Engineering Mechanics Division, ASCE, Vol. 110, No. EM6, pp. 957-971.
8. Elwi, A.E., and Murray, D.W. (1980), 'Nonlinear Analysis

of Axisymmetric Reinforced Concrete Structures", Structural Engineering Report No. 87, Department of Civil ENgineering, The University of Alberta, Edmonton, Alberta, Canada.

9. Jaky, J. (1948), "Pressure in Silos", Proceedings, 2nd International Conference on Soil Mechanics and Foundation Engineering, Rotterdam, Vol. 1, pp. 103-107.
10. Janssen, H.A. (1895), "Versuche über Getreidedruck in Silozellen (Experiments about Pressure of Grain in Silos)", Zeitshrift Verein Deutscher Ingenieure, Vol. 39, pp.1045-1049.
11. Jenike, A.W., and Shield, R.T. (1959), "On the Plastic Flow of Coulomb Solids Beyond Original Failure", Journal of Applied Mechanics, Transactions, ASME, Vol. 26, No. 4, Series E, pp. 599-602.
12. Jenike, A.W. (1961), "Gravity Flow of Bulk Solids", Bulletin #108, Utah Engineering Experimental Station, University of Utah.
13. Jenike, A.W. (1964), "Storage and Flow of Solids", Bulletin #123, Utah Engineering Experimental Station, University of Utah.
14. Jenike, A.W. (1964), "Steady Gravity Flow of Frictional Cohesive Solids in Converging Channels", Journal of Applied Mechanics, Series E, Vol. 31, No. 1, pp. 5-11.
15. Jenike, A.W., and Johanson, J.R. (1968), "Bin Loads", Journal of the Structural Division, ASCE, Vol. 94, No. ST4, pp. 1011-1041.

16. Jenike, A.W., and Johanson, J.R. (1969), "On the Theory of Bin Loads", Journal of Engineering for Industry, Transactions, ASME, Series B, Vol. 91, No. 2, pp. 339-344.

17. Jenike, A.W., Johanson, J.R., and Carson, J.W. (1973), "Bin Loads - Part 2: Concepts", Journal of Engineering for Industry, Transactions, ASME, Vol. 95, No. 1, pp. 1-5.

18. Jenike, A.W., Johanson, J.R., and Carson, J.W.(1973), "Bin Loads - Part 3: Mass Flow Bins", Journal of Engineering for Industry, Transactions, ASME, Vol. 95, No. 1, pp. 6-12.

19. Jofriet, J.C., Lelievre, B., and Fwa, T.F. (1977), "Frictional Model for Finite Element Analyses of Silos", Transactions, ASAE, Vol. 20, No. 4, pp. 735-740 and 744.

20. Katona, M.G. (1983), "A Simple Contact-Friction Interface Element with Applications to Buried Culverts", International Journal of Numerical and Analytical Methods in Geomechanics, Vol. 7, pp. 371-384.

21. Lade, P.V. (1977), "Elasto-Plastic Stress-Strain Theory for Cohesionless Soil with Curved Yield Surfaces", International Journal of Solids and Structures, Vol. 13, pp. 1019-1035.

22. Moriyama, R., and Jotaki, T. (1980), "An Investigation of Wall Pressures in Flowing and Static Bulk Materials in Model Bins", International Conference on Design of Silos for Strength and Flow, University of Lancaster,

pp. 1-12.

23. Motzkus, U. (1974), "Belastung von Siloböden und Auslauftrichten durch Körnige Schüttgüter", Dissertation, Technical University of Braunschweig, Germany.
24. Smith, A.B.B, and Simmonds, S.H. (1983), "Lateral Coal Pressures in a Mass Flow Silo", Structural Engineering Report No. 113, Department of Civil Engineering, The University of Alberta, Edmonton, Alberta, Canada.
25. Walker, D.M. (1966), "An Approximate Theory for Pressures and Arching in Hoppers", Chemical Engineering Science, Vol. 21, pp. 975-997.
26. Walker, D.M., and Blanchard, M.H. (1967), "Pressures in Experimental Coal Hoppers", Chemical Engineering Science, Vol. 22, pp. 1713-1745.
27. Walli, G., and Schwaighofer, J. (1984), "A Bibliography on Silos (1857-1979): Addendum 1899-1983", Department of Civil Engineering, University of Toronto.
28. Walters, J.K. (1973), "Theoretical Analysis of Stresses in Silos with Vertical Walls", Chemical Engineering Science, Vol. 28, No. 1, pp. 13-21.
29. Walters, J.K. (1973), "Theoretical Analysis of Stresses in Axially Symmetric Hoppers and Bunkers", Chemical Engineering Science, Vol. 28, No. 3, pp. 779-789.
30. Willam, K.J., and Warnke, E.P. (1975), "Constitutive Model for Triaxial Behavior of Concrete", IABSE Seminar on Concrete Structures Subjected to Triaxial Stresses,

ISMES, Bergamo, Italy, IABSE Proceedings, Vol. 19.

31. Zienkiewicz, O.C. (1977), "The Finite Element Method", McGraw-Hill.

APPENDIX A - Numerical Implementation of the Material Constitutive Model

The numerical implementation of the elastic perfectly plastic material model used in this study can be described as follows:

1) An elastic stress increment $\{\Delta\sigma\}_{test}$ is calculated from the strain increment $\{\Delta\epsilon\}$ as a trial stress path. A trial total stress state $\{\sigma\}_{test}$ is obtained as the sum of the stress state from the previous load step $\{\sigma\}_0$ and the trial stress increment.

$$\{\Delta\sigma\}_{test} = [C]\{\Delta\epsilon\}, \qquad [A.1]$$

$$\{\sigma\} = \{\sigma\}_0 + \{\Delta\sigma\}_{test}. \qquad [A.2]$$

2) The total stress state is tested against the yield criteria

a) $f(\sigma_{test}) \leq 0$

b) $f(\sigma_{test}) = 0 \quad <\partial f/\partial\sigma>\{\Delta\sigma\}_{test} < 0$

c) $f(\sigma_{test}) \geq 0 \quad <\partial f/\partial\sigma>\{\Delta\sigma\}_{test} > 0$

3) If conditions a) or b) are satisfied, then the test path is elastic and we can now proceed to the next strain increment. If condition c) is obtained, then the strain increment $\{\Delta\epsilon\}$ includes plastic flow. If the original stress state, $\{\sigma\}_0$ in Eq. A.2, was plastic, then one can proceed directly to Step 4. If it was elastic then it is necessary that the stress increment $\{\Delta\sigma\}_{test}$ be divided

into two parts (See Fig A.1); an elastic part $\{\Delta\sigma\}_e$, and a part after onset of yield $\{\Delta\sigma\}_{oy}$

$$\{\Delta\sigma\}_{test} = \{\Delta\sigma\}_e + \{\Delta\sigma\}_{oy}. \qquad [A.3]$$

Dividing the stress increment in this way requires determination of the intersection point A in Fig. A.1. There is a variety of methods available to do this, and the approach chosen here is an interval halving technique. The total stress state is updated as

$$\{\sigma\} = \{\sigma\}_0 + \{\Delta\sigma\}_e. \qquad [A.4]$$

The total stress is represented by Point "A" in Fig. A.1. Note that $\{\sigma\}$ now lies on the yield surface.

4) The strain increment $\{\Delta\epsilon\}_e$ corresponding to $\{\Delta\sigma\}_e$ is calculated as

$$\{\Delta\epsilon\}_e = (\|\{\Delta\sigma\}_e\|/\|\{\Delta\sigma\}\|)\{\Delta\epsilon\}, \qquad [A.5]$$

and the strain increment after onset of yield is computed as

$$\{\Delta\epsilon\}_{oy} = \{\Delta\epsilon\} - \{\Delta\epsilon\}_e. \qquad [A.6]$$

5) The stress increment after onset of yielding is calculated using $\{\Delta\epsilon\}_{oy}$ and the constitutive relationship in Eq. 5.9

$$\{\Delta\sigma\}_{oy} = \left[[C] - \frac{[C]\ \{\partial f/\partial\sigma\}\ <\partial g/\partial\sigma>\ [C]}{<\partial f/\partial\sigma>\ [C]\ \{\partial g/\partial\sigma\}}\right]\{\Delta\epsilon\}_{oy}. \qquad [A.7]$$

The calculation is illustrated in Fig. A.1. The total

stress state is updated to the state of stress at point "B". The stress increment $\{\Delta\sigma\}_{oy}$ is projected in a direction tangent to the yield surface at the point of intersection.

6) As shown by Fig. A.1, the total stress vector is not on the yield surface, point B. This is because the incremental stress - strain relationship is, in theory, continuous. This means that the surface gradient $\{\partial f/\partial\sigma\}$ should be evaluated on a continuous basis. Equation A.7 implies a piecewise linear approximation of $\{\Delta\sigma\}_{oy}$. Since $\{\Delta\sigma\}_{oy}$ moves linearly in a direction tangent to the yield surface, Point B is not on the curved yield surface.

Point B must be scaled onto the yield surface. An approach used by Chen (1982) is to assume the correction is normal to the yield surface, i.e.

$$\{\delta\sigma\} = a\{\partial f/\partial\sigma\}, \qquad [A.8]$$

where a is a scaling factor The expression for the correction stress can then be derived using the normality condition, Eq. 5.4, as

$$\{\delta\sigma\} = -\frac{\{\partial f/\partial\sigma\}f(\sigma)}{<\partial f/\partial\sigma>\{\partial f/\partial\sigma\}}. \qquad [A.9]$$

The total stress state is then updated from Point B to a point close to the yield surface. The scaling procedure may have to be repeated several times to obtain an acceptable error tolerance in regions of high surface

curvature.

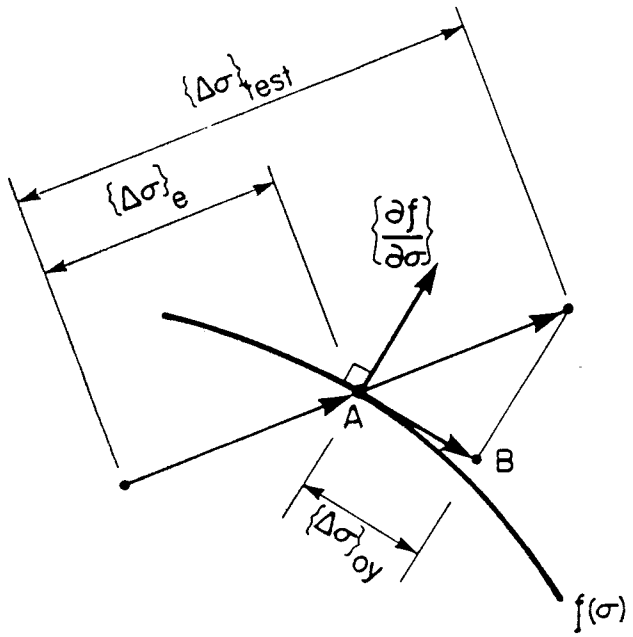

Figure A.1 Illustrative representation of numerical implementation of material model

APPENDIX B - Derivation of the Jenike and Walker Overpressure Envelopes

It is relatively simple to obtain a Jenike envelope of switch stresses. Consider a hopper configuration as shown in Fig. B.1. The position of the switch is at level $\beta_i z_i$, where $\beta_i = z_i/z_0$. Above the switch point, the stress field is active, and a vertical force, Q_i, acts on the cross section at z_i. Below the switch point, the field is passive, and a reduced flow force Q_f reacts. In order to maintain equilibrium at the switch point, the wall must develop an overpressure or concentrated force. To obtain a Jenike envelope, the equation of equilibrium is written from examination of Fig. B.2.

$$N(\sin \theta' + \cos \theta' \tan \phi') = Q_i - Q_f \qquad [B.1]$$

Jenike et. al. (1973) obtained an expression for the overpressure at the transition based on Eq. B.1. This expression, Eq. 1.9, can be extended to obtain the solution for the switch envelope (assuming a distribution depth of $0.3\beta_i B$).

$$\sigma_{si} = \sigma_{ri} + \frac{3.3(\sigma_{vi} - (4/\pi)^m q\gamma(\beta_i B))}{(2 - 0.4 \sin \theta')^m(\sin \theta' + \cos \theta' \tan \phi')}, \qquad [B.2]$$

where σ_{vi} is the vertical initial filling stress at the switch point. The flow radial stress at the switch point, σ_{ri}, is obtained as a modification of Eq. 2.10

$$\sigma_{ri} = (\sigma'/\gamma B)\beta_i \gamma B. \qquad [B.3]$$

Charts for $(\sigma'/\gamma B)$ as a function of θ', δ, and ϕ' have been developed by Jenike (1961). The stress parameter q is obtained by integrating the vertical components of the radial stress field over the cross sectional area, and charts for q have also been developed by Jenike (1961).

Examination of Fig. B.1 yields the expression for the vertical stress σ_{vi} using Jenike's approximation (discussed in Section 2.2.2).

$$\sigma_{vi} = \gamma z_0(1 - \beta_i) + \beta_i \sigma_J, \qquad [B.4]$$

where σ_J is the Janssen pressure at the transition (Eq. 2.9a).

It is also simple to obtain a Walker envelope. The expression of Eq. 2.15 can be modified to calculate vertical stresses below a variable switch point

$$\sigma_v = \frac{\gamma z}{C - 1}\left[1 - \left[\frac{z}{z_i}\right]^{C-1}\right] + \sigma_{vi}\left[\frac{z}{z_i}\right]^{C}, \qquad [B.5]$$

where σ_v is the vertical stress at the switch point z_i. The dimensionless stress parameter C is obtained from Eq. 2.15.

If the switch occurs at $z = z_i$, the above expression reduces to

$$\sigma_v = \sigma_{vi}. \qquad [B.6]$$

To transform the vertical stress into wall pressure, Walker (1966) derived the expression

$$\sigma_{si} = \frac{1 + \sin\delta \cos 2\beta}{1 - \sin\delta \cos 2(\theta' + \beta)} \sigma_{vi}, \qquad [B.7]$$

where

$$\beta = \frac{1}{2}\left[\phi' + \text{Arcsin}\left[\frac{\sin \phi'}{\sin \delta}\right]\right]. \qquad [B.8]$$

Switch stresses may be obtained directly from Eq. B.7.

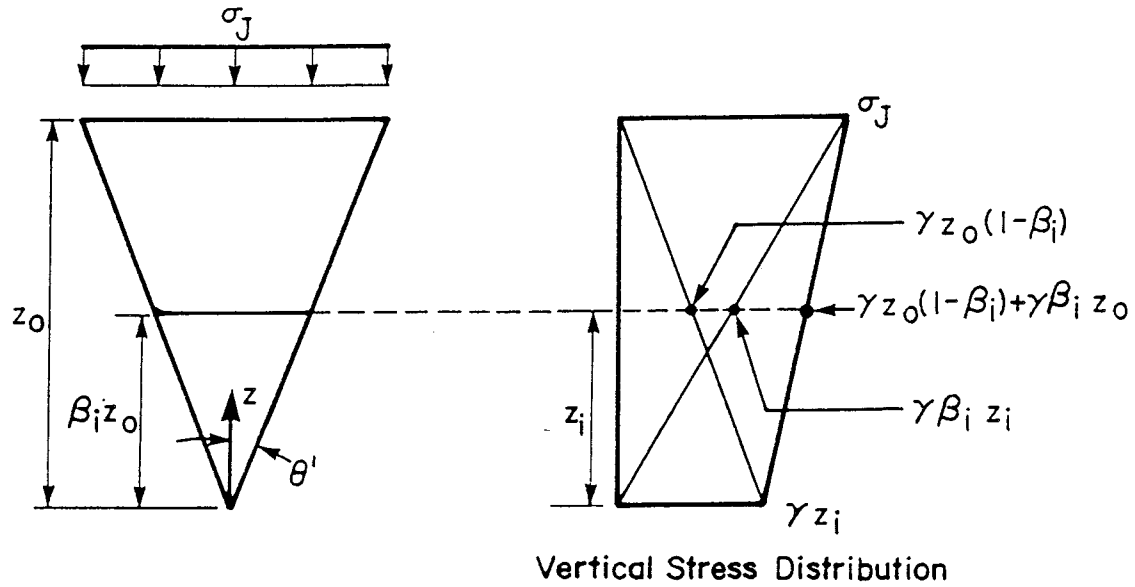

Figure B.1 Determination of σ_{vi}

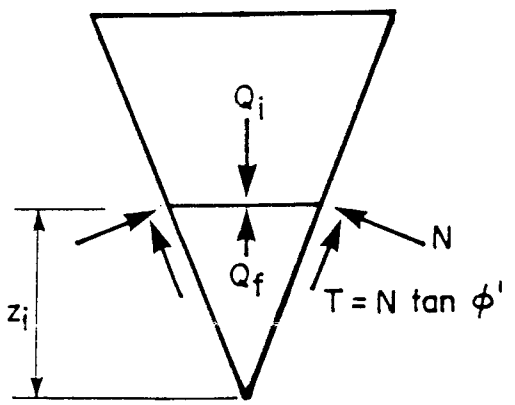

Figure B.2 Equilibrium of switch point